Adhesion and the Lamination/Failure of Stretchable Organic and Composite Organic/Inorganic Electronic Structures

Deying Yu

A Dissertation
Presented to the Faculty
of Princeton University
in Candidacy for the Degree
of Doctor of Philosophy

Recommended for Acceptance
by the Department of
Mechanical and Aerospace Engineering
Adviser: Professor Winston Oluwole Soboyejo

September 2017

Abstract

Stretchable organic electronics have emerged as interesting technologies for several applications where stretchability is considered important. The easy and low-cost deposition procedures for the fabrication of stretchable organic solar cells and organic light emitting devices reduce the overall cost for the fabrication of these devices. However, the interfacial cracks and defects at the interfaces of the devices, during fabrication, are detrimental to the performance of stretchable organic electronic devices. Also, as the devices are deformed under service conditions, it is possible for cracks to grow. Furthermore, the multilayered structures of the devices can fail due to the delamination and buckling of the layered structures. There is, therefore, a need to study the failure mechanism in the layered structures that are relevant to stretchable organic electronic devices.

Hence, in this study, a combined experimental, analytical and computational approach is used to study the effects of adhesion and deformation on the failure mechanisms in structures that are relevant to stretchable electronic devices. First, the failure mechanisms are studied in stretchable inorganic electronic structures. The wrinkles and buckles are formed by the unloading of pre-stretched PDMS/Au structure, after the evaporation of nano-scale Au layers. They are then characterized using atomic force microscopy and scanning electron microscopy. Analytical models are used to determine the critical stresses for wrinkling and buckling. The interfacial cracking and film buckling that can occur are also studied using finite element simulations. The implications of the results are then discussed for the potential

applications of micro-wrinkles and micro-buckles in the stretchable electronic structures and biomedical devices.

Subsequently, the adhesion between bi-material pairs that are relevant to organic light emitting devices, composite organic/inorganic light emitting devices, organic bulk heterojunction solar cells, and composite organic/inorganic solar cells on flexible substrates, is measured using force microscopy (AFM) techniques. The AFM measurements are incorporated into the Derjaguin-Muller-Toporov model to calculate the adhesion energies. The implications of the results are then discussed for the design of robust organic and composite organic/inorganic electronic devices.

Finally, the lamination of organic solar cells and organic light emitting devices is studied using a combination of experimental, computational, and analytical approaches. First, the effects of applied lamination force (on contact between the laminated layers) are studied using experiments and models. The crack driving forces associated with the interfacial cracks that form at the interfaces between layers (at the bi-material interfaces) are estimated along with the critical interfacial crack driving forces associated with the separation of thin films, after layer transfer. The conditions for successful lamination are predicted using a combination of experiments and models. Guidelines are developed for the lamination of low-cost organic electronic structures.

Acknowledgements

First of all, I would like to extend my deepest gratitude to my advisor, Professor Wole Soboyejo, for his guidance, encouragement and support. Professor Soboyejo is more than an advisor, but also a mentor to me. I appreciate all his effort and patience on leading me through each stage of the research and study, as well as providing me with the valuable instructions and suggestions on my thesis. Also, I am grateful to Professor Daniel Steingart and Professor George Scherer for reviewing this thesis, and Professor Daniel Steingart and Dr. Nan Yao for the valuable comments as my dissertation committee members.

I am grateful to Professor Barrie Royce for useful technical discussions. I am also grateful to Dr. Nan Yao and Mr. Gerald R. Poirier for their technical assistance. I would like to thank Professor Jeremy Kasdin for his encouragement and help all the time.

I would like to thank all my colleagues in the Soboyejo research group. I would like to thank Dr. Tiffany Tong for research collaborations and guidance. Professor Jing Du for the help on my study and research; Dr. Yusuf Oni for the encouragement and support. I also want to express my gratitude to the other Soboyejo group members: Dr. Wanliang Shan, Dr. Emily Hampp, Dr. Juan Meng, Dr. Wali Akande, Dr. Jianbo Chen, Dr. Guoguang Fu, Dr. Ismaiel Yakub, Dr. Karen Malatesta, and Dr. Onobu Akogwu.

The research was supported by the National Science Foundation (DMR 0231418), Princeton University, and the Princeton Grand Challenges Program. These finacial supports from these organizations/programs are all greatly appreciated.

Last but not least, I would like to express my gratitude to my parents, for their love, support and encouragement throughout the years. I feel not only thankful but blessed to have them in my life.

This dissertation carries T# 3276T in the records of the Department of Mechanical and Aerospace Engineering.

To my family,

my parents, Mrs. Xiaolan Li and Mr. Shuguang Yu.

Contents

List of Tables

List of Figures

Chapter 1

Background and Introduction

1.1 Introduction

Stretchable electronics have emerged as interesting and important technologies for several applications in which stretchability is important [58, 59, 64, 65, 68, 73, 76, 82]. Stretchable electronics are either organic [76], inorganic [58, 59, 64, 68, 73] or composite organic-inorganic [82] structures that have applications in electrical inter-connects [58, 59, 64, 65, 73], optical sensors [7, 119], diffraction gratings [7, 119], solar cells [68,76], light emitting devices [82], surfaces for cell contact guidance [52,66] and biomedical devices [52]. Stretchable electronics can also be integrated into multipurpose electronic systems that can serve as roofing tiles, energy harvesting systems and lighting of the future.

Stretchable inorganic electronics are often fabricated from inorganic materials that are deposited on stretchable substrates [59, 68, 73]. Figure 1.1 illustrates an

example of a PDMS substrate (Figure 1.1a) that is first pre-stretched (Figure 1.1b). Cr and Au thin layers (Figure 1.1c and d) are then deposited onto the pre-stretched PDMS substrate (Cr is an adhesion promoter while Au is a flexible electronic material). The pre-stretched PDMS substrate is then released to produce wrinkled (Figure 1.1e) or micro-buckled (Figure 1.1f) thin gold films on PDMS substrates. Broad ranges of stretchability are possible for such wrinkled and micro-buckled structures. Stretchable inorganic electronics include: stretchable inorganic light emitting devices, stretchable transistors and stretchable inter-connects. These devices can be fabricated on rigid substrates before they are transferred to stretchable substrates. They are usually bonded [58, 59] to the stretchable substrates, while the connectors between the devices are free to buckle [58, 59]. In some situations, these devices are deposited onto the substrates by applying the chemical and physical processes, such as spin-coating, thermal evaporation, and Chemical Vapour Deposition (CVD) techniques.

Stretchable organic electronics are produced from organic materials on stretchable substrates. However, stretchable composite organic-inorganic electronics are fabricated from mixtures of both organic and inorganic materials on stretchable substrates. Also, the metallic films can be introduced by lamination techniques [1] that transfer the soft or hard layers directly onto adhesive surfaces. The rigidity of the inorganic constituents can also be managed by introducing pre-buckled thin film structures onto stretchable substrates [58, 59, 64, 65, 68, 73].

The release of the substrate pre-stretching can cause wrinkling [59] and buckling [76] that is associated with out-of-plane structures that can accommodate strains.

Therefore, in a number of scenarios [58, 59, 64, 76], the substrates are pre-strained before the deposition of the layered structures of stretchable devices. . As shown in Figure 1.2, for stretchable organic solar cells, the PDMS substrate is pre-stretched before the deposition of the $PEDOT:PSS$, $P3HT:PCBM$ and the EGaIn layers. After the release of the PDMS substrate, wrinkled and buckled films are formed on the PDMS substrate. The pre-strain levels affect the amplitudes of the resulting buckled and wrinkled structures [111]. Hence, it is important to know the level of the applied pre-strain that can result in the formation of buckled and wrinkled structures, without inducing failure in the individual layers and interfaces within the devices.

The structures of stretchable electronics range from, bi-layered inorganic metallic (silicon)-coated substrates, to multilayered organic and organic-inorganic structures coated on pre-strained substrates. In the case of bi-layered stretchable electronic structures, the interfacial adhesion between the two different materials can enhance the formation of wavy structures that further improve their stretchability. Furthermore, cyclic loading may cause interfacial cracking in layered electronic structures. This dissertation studies the interfacial adhesion and failure of stretchable electronic structures to provide insights and models for the design and fabrication of stretchable/flexible electronic structures.

1.2 Unresolved Issues

There have been relatively few studies of the effects of adhesion and processing on the reliability of stretchable electronic structures. Since the reliability of stretchable electronic structures could depend strongly on the interfacial adhesion and the fabrication techniques, there is a need for a more detailed understanding of the effects of adhesion and stretching on the behavior of stretchable electronic structures.

1.3 Scope and Organization of Thesis

In this dissertation, a combined analytical, experimental and computational approach is used to study the effects of adhesion and stretching on the failure mechanisms of layered structures that are relevant to stretchable/flexible organic and composite organic-inorganic solar cells and light emitting devices. First, the failure mechanisms in the model are investigated by using both experiments and analytical/computational models. The role of adhesion is then studied in experiments on stretchable/flexible organic and composite organic-inorganic solar cells and light emitting devices. A combined experimental, computational and analytical approach is then used to study the lamination process of organic solar cells and light emitting devices.

Chapter 1 provides the background and introduction, the objectives and the scope of this dissertation.

Chapter 2 reviews prior work on stretchable/flexible electronic structures and the literature on thin film fracture mechanics and the failure mechanics. The literature

review includes: stretchable inorganic electronic structures; stretchable organic electronic structures; stretchable organic solar cells; adhesion theory; fracture mechanics theory; wrinkling and micro-buckling of thin films; thin film fracture mechanics and lamination mechanics.

Chapter 3 presents the failure mechanisms in stretchable inorganic electronic structures. The results of experimental and theoretical/computational studies of micro-wrinkles and buckling are presented. The wrinkles and buckles are formed by the unloading of pre-strained PDMS substrate, after the evaporation of nano-scale Au layers. They are then characterized using atomic force microscopy and scanning electron microscopy. The critical stresses required for wrinkling and buckling are determined from analytical models. Finite element simulations of interfacial crack growth are then used to investigate the possible interfacial cracking that can occur with the film buckling. The implications of the results are discussed for potential applications of micro-wrinkles and micro-buckles in stretchable electronic structures and biomedical devices

Chapter 4 presents the results of an experimental study of the adhesion between bi-material pairs that are relevant to organic light emitting devices, composite organic/inorganic light emitting devices, organic bulk heterojunction solar cells, and composite organic/inorganic solar cells on flexible substrates. The adhesion between the possible bi-material pairs is measured using force microscopy techniques. The results of the force microscopy measurements are used in the Derjaguin-Muller-Toporov model to determine the adhesion energies. The

implications of the results are then discussed for the design of robust organic and composite organic/inorganic electronic devices.

Chapter 5 presents the lamination of organic solar cells and organic light emitting devices at the macro- and micro-scales. These are studied using a combination of experimental techniques and computational/analytical models. First, the effects of applied lamination force (on contact between the laminated layers) are investigated. The crack driving forces associated with the interfacial cracks (at the bi-material interfaces) are then estimated, along with the critical interfacial crack driving forces associated with the separation of the thin films, following the layer transfer. The experiments and computational models are used to predict the conditions for the successful lamination. Processing guidelines are then developed for the lamination of low-cost organic electronic devices.

Finally, conclusions arising from this work are presented in Chapter 6, along with suggestions for future work.

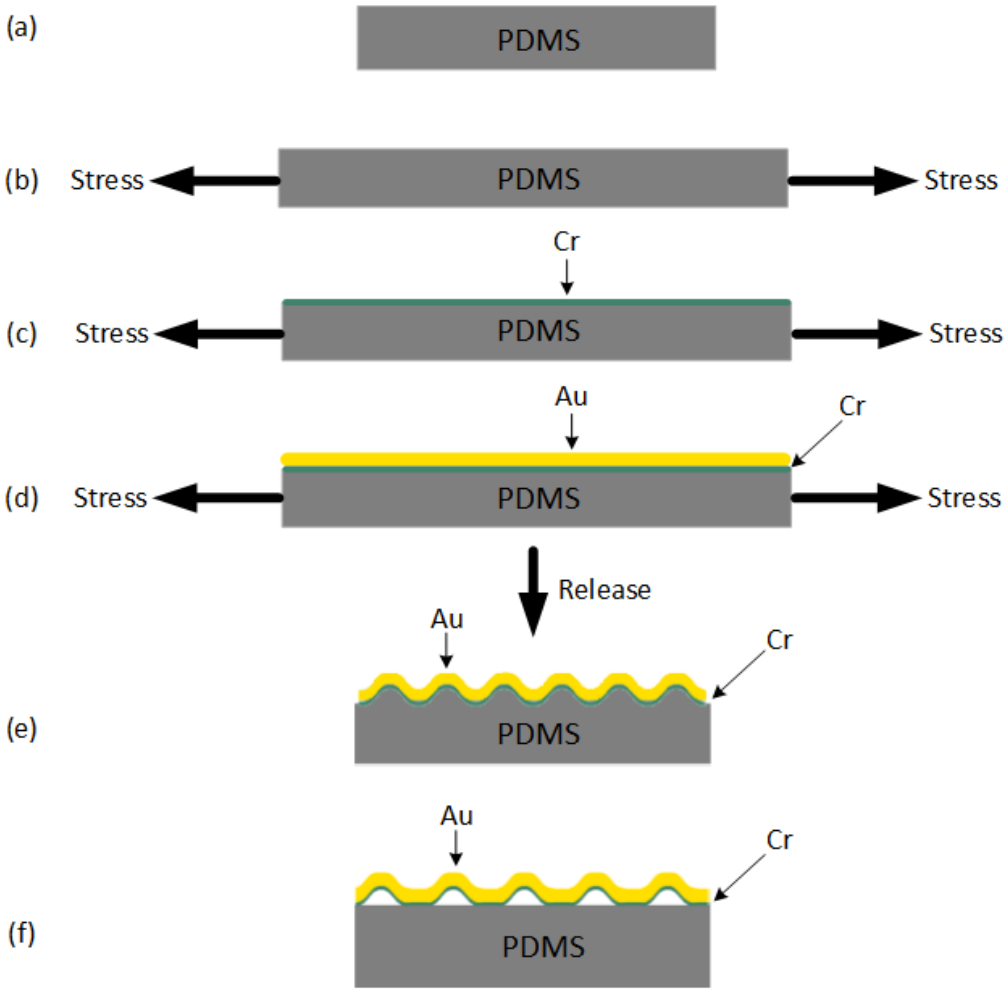

Figure 1.1: Schematic illustration of structural approach to stretchable inorganic materials. (a) Unstretched PDMS substrate. (b) Pre-stretching of PDMS substrate. (c) Deposition of $\sim$ 5 nm thick Cr interlayer. (d) Deposition of $\sim$ 50-200 nm thick Au layer. (e) Wrinkling after the release of PDMS substrate. (f) Micro-buckling after the release of PDMS substrate.

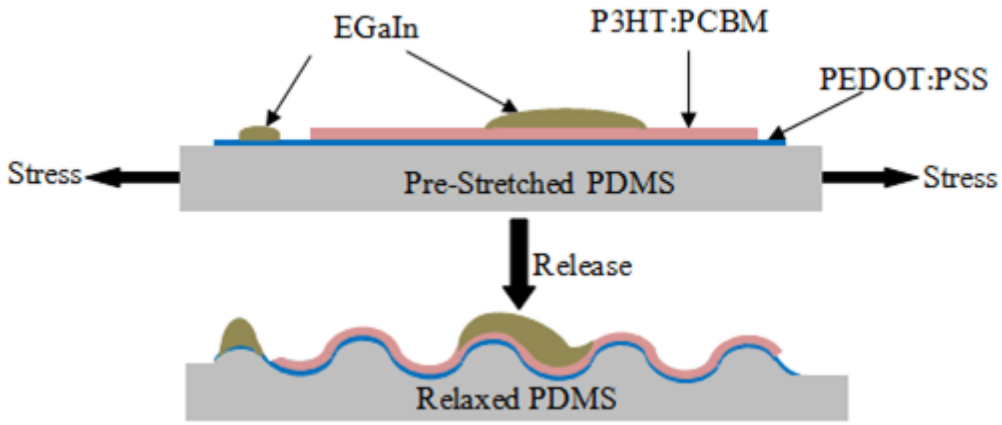

Figure 1.2: Wrinkled and buckled films formed from the release of the pre-stretched PDMS substrate.

Chapter 2

Literature Review

2.1 Stretchable/Flexible Electronic Structures

In most cases, stretchable electronics are either inorganic, organic or composite organic-inorganic structures. For inorganic electronic structures, applications have been found in stretchable electrical inter-connects [58, 59, 64, 65, 73], optical sensors and diffraction gratings [7, 119], metrology for the measurement of elastic moduli [101, 102], templates for device fabrication [118], stretchable electronics [65, 73, 76, 114], micro-contact printing stamps [87, 110], cell culture substrates [66] and surfaces for cell contact guidance [52] in implantable biomedical devices. Prior work by Rogers and co-workers [58, 64, 68, 103] has identified the importance of buckling as a strategy for achieving stretchable inorganic electronic devices, stretchable optoelectronic devices, stretchable integrated systems,

stretchable metallic inter-connect and emerging stretchable curvilinear systems for biomedical applications.

Stretchable organic electronic structures become very important for its easy fabrication, large surface area coverage and cost reduction. For stretchable organic light emitting devices, the active materials, which are capable of emitting light in response to electric current are sandwiched between two electrodes (an anode and a cathode) (Figure 2.1). When the layered structures are deposited on stretchable substrates, they become stretchable. Sekitani et al. [96] have showed the stretchable active-matrix organic light emitting diode display using printable elastic conductors. Yu et al. [122] have also showed intrinsically stretchable polymer light emitting devices by applying carbon nanotube polymer composite electrodes. The metal-free devices they presented can be linearly stretched up to 45%. Song et al. [100] have presented an emerging anodic transparent conducting electrode for organic light emitting devices that can accommodate deformations.

For stretchable organic solar cells, as shown in Figure 1.2, when the layered structures are deposited on stretchable substrates they become stretchable. A schematic of a typical structure of stretchable organic solar cell is presented in Figure 2.2. The layered structures of the bulk heterojunction solar cells include an active materials that are capable of absorbing light and photogenerate hole-electron pairs, which are separated and collected at the electrodes before recombination. The bulk heterojunction system, a blend of poly(3-hexylthiophene) (P3HT) as the donor and fullerene derivative (6,6)-phenyl C61-butyric acid methyl ester (PCMB) as the acceptor (P3HT:PCMB), is an effective electron donor/acceptor

combination in terms of efficiency and long term stability [95]. This P3HT:PCMB bulk heterojunction system has dominated organic solar cells between 2007 and 2017 [18].

The first organic solar cells consisted of an active layer that is made of a single material sandwiched between two electrodes of different work functions [4]. Tang (in 1986) introduced the organic bilayer solar cells, which consisted of a double-layer structure of two organic semiconductor materials with different electron affinity. This is regarded as a breakthrough in the history of organic solar cells [109]. The second layer was a quantum leap (atomic electron transition) in terms of power conversion efficiency. These organic bilayer solar cells made of conjugated small molecules achieved a low power conversion efficiency of about 1% [109]. The major limiting factor is that the thickness of the absorbing materials is much more than the diffusion length of the excitons (bound electron-hole pairs) [84]. The layer thickness of the absorbing materials has to be of the same order of the absorbing length in order to achieve high power conversion efficiency.

Yu et al. [84] introduced bulk heterojunction solar photovoltaic cells, which have improved the manufacturing of organic solar cells. The interface between donor and acceptor materials is spatially distributed, as both components inter-penetrate each other. By spin coating a polymer fullerene blend, the concept of bulk heterojunction solar cells is implemented. Solution processed bulk heterojunction solar cells can achieve better power conversion efficiency by using engineered materials and additives that optimize the phase separation.

Although some of the thin film stretchable organic solar cells are intrinsically brittle, they can be made somewhat compliant by pre-stretching the substrate before the deposition of the layers. Bao and co-workers [84,121] deposited organic solar cells on pre-stretched substrates, which buckled upon release, to form structures shown schematically in Figure 2.3. The stretchable organic solar cells can be strained to 27%. The structures can be stretched within the limit of the pre-strain. However, the failure caused by delamination and buckling of the films can be very significant when the devices experience several cyclic deformations, especially above the pre-strain.

2.2 Adhesion Theory

2.2.1 Adhesion Force

There is a need to measure the adhesion between layers that are relevant to stretchable inorganic, organic, and composite organic-inorganic electronic structures, since the contacts between layers can affect the degradation and electronic performance of the devices. The adhesion force between two materials can be measured using contact mode atomic force microscopy (AFM).

In order to measure the adhesion force between two dissimilar materials, the AFM tip is coated with one material, while the substrate is coated with the second material Figure 2.4. The steps involved in the measurement of the adhesion force are illustrated in Figure 2.5. The cantilever tip begins at point A, at a distance from the substrate. In this case, there is minimal long-range attractive force, so there is no deflection of the tip on the force-displacement between A and B. As the tip is

lowered towards the surface, it jumps into contact. This is due to increasing adhesive attractive forces, as the tip approaches point B. Subsequently, the tip bends under elastic deformation, as the deflection increases past point C. The process is then reversed after loading the tip to a maximum force. However, as the tip is reversed, it does not detach at zero force. This is due to the effects of adhesion at point D. Instead, the reversed loading must be continued to point E, at which the force is sufficient to overcome the adhesive interactions. The adhesion force, F, is determined from Hooke's law to be:

$$F = -kx, \tag{2.1}$$

where x is the tip displacement (A-E) and k is the spring constant of the AFM tip. The spring constant, k, of each AFM tip was measured using the thermal tune method [97].

2.2.2 Adhesion Energy

The adhesion energy can be considered as the energy required to adhesively break the interfacial secondary bonds between the two dissimilar materials. In order to determine the adhesion energy from the measured adhesion force, several models have been developed for different materials and geometry properties of the interacting layers.

The Derjaguin-Muller-Toporov (DMT) model [19] applies to weak long-range interactions between stiff materials with small radii. The adhesion energy, γ, is

related to the adhesion forces, $F_{adhesive}$, by the following expression:

$$\gamma_{DMT} = \frac{F_{adhesive}}{2\pi R}, \tag{2.2}$$

where R is the effective radius, which is calculated through [19]:

$$R = (\frac{1}{R_{rms}} + \frac{1}{R_{tip}})^{-1}, \tag{2.3}$$

where R_{rms} and R_{tip} are the radii of the average roughness of the substrate and the coated AFM tip, respectively.

The Johnson-Kendall-Robert (JKR) model [53] is used to characterize strong near-range adhesive forces between compliant materials with large radii. The adhesion force and energy are related by the following formula:

$$\gamma_{JKR} = \frac{2F_{adhesive}}{3\pi R}. \tag{2.4}$$

Analytical methods are used to calculate the exact relationship between the adhesion force and energy for the Maugis-Dugdale (MD) model [78] that is between the above two limiting cases. Carpick et al. [13] introduced an iterative process to simplify this work, and Pietrement and Troyon [86] reached a generalized approximation of the MD adhesion energy to within 1% accuracy. The calculation of a non-dimensionalized parameter, λ, is used to characterize the entire range of adhesion models:

$$\lambda = 2\sigma_0(\frac{R}{\pi\kappa^2\gamma})^{\frac{1}{3}}. \tag{2.5}$$

If $\lambda < 0.1$, the DMT model applies and if $\lambda > 5$, the JKR model applies. Values between 0.1 and 5 correspond to the transition field between DMT and JKR models. σ_0 is a constant adhesive force between two bodies, and is non-zero at small distances h. Separation between the bodies will happen at a separation height, defined as h_0, after which $\sigma_0 = 0$. The two terms have the following relationship with the adhesion energy:

$$\sigma_0 h_0 = \gamma. \tag{2.6}$$

The constant, κ, is obtained from:

$$\kappa = \frac{4}{3}[\frac{1-\nu_1^2}{E_1} + \frac{1-\nu_2^2}{E_2}]^{-1}, \tag{2.7}$$

where ν_1 is the Poisson's ratio for layer 1 and ν_2 is the Poisson's ratio for layer 2, E_1 is the elastic modulus for layer 1 and E_2 is the elastic modulus for layer 2.

According to the Carpick model, the adhesion force is related to the adhesion energy through:

$$\gamma = \frac{F_{adhesive}}{\pi R \bar{F}_{adhesive}}, \tag{2.8}$$

where:

$$\bar{F}_{adhesive} = 0.267\alpha^2 - 0.767\alpha + 2. \tag{2.9}$$

Values of $\lambda < 0.1$ correspond to the DMT model, and $\lambda > 5$ correspond to the JKR model. Intermediate values correspond to the MD range. An iterative approximation is necessary due to the inter-dependence of terms in Equations 2.5, 2.6, 2.7, 2.8, 2.9.

The above formulae can be used to convert the adhesion forces measured from the AFM adhesion experiments to adhesion energy over a wide range of scenarios.

2.3 Fracture Mechanics Theory

2.3.1 Linear Elastic Fracture Mechanics

The three modes of crack growth are presented in Figure 2.6 [99]. Mode I (Figure 2.6(a)) corresponds to the crack opening mode, which is the most damaging mode of all the crack growth modes. Mode II (Figure 2.6 (b)) refers to the in-plane shear mode, while Mode III (Figure 2.6(c)) is the out-of-plane shear mode. Each of the three modes can occur separately, or in combination with the others.

Under linear elastic conditions, the crack-tip stress fields are given by [99]:

$$\sigma_{ij} = \frac{K}{\sqrt{2\pi r}}\tilde{\sigma_{ij}}(\theta), \tag{2.10}$$

where σ is the stress, and r and θ are the coordinates in the polar coordinate system, with the origin at the crack tip. K represents the amplitude of the crack-tip fields. It is the driving force for crack growth. The stress intensity factor, K, is given by [99]:

$$K = f(a/w)\sigma\sqrt{\pi a}, \tag{2.11}$$

where σ is the applied remote stress, $f(a/w)$ is a function of the crack length, a, and the specimen width, w.

Equation (2.10) shows that there is a singularity of stress at the crack-tip, i.e., the stress at crack tip approaches infinity, as the distance r approaches zero. However, in reality, infinite stresses can not be reached, since the region near the crack-tip yields when the yield stress is exceeded near the crack tip. This results in the formation of a plastic zone around the crack tip. Generally, the concept of K applies when the size of plastic zone at the crack tip is small compared to the crack length.

The strain energy is stored in the area ahead of the crack tip. This strain energy is released when crack growth occurs. The energy release rate for Modes I, II, and III can be summed up since energy is a scalar quantity. For a three-dimensional solid with mode I, II and III, the energy release rate, G, is given as:

$$G = G_I + G_{II} + G_{III}, \tag{2.12}$$

$$G_I = K_I^2/E',\ G_{II} = K_{II}^2/E',\ G_{III} = K_{III}^2/2\mu = (1+\nu)K_{III}^2/E, \tag{2.13}$$

where E is the Young's modulus, μ is the shear modulus and ν is the Poisson's ratio. For plane stress conditions: $E' = E$, for plane strain conditions: $E' = E/(1-\nu^2)$. Therefore, we have [104]:

$$G = \frac{1}{E}(K_I^2 + K_{II}^2) \quad \text{(for plane stress)} \tag{2.14}$$

$$\text{and} \quad G = \frac{(1-\nu^2)}{E}(K_I^2 + K_{II}^2) + \frac{1+\nu}{E}K_{III}^2 \quad \text{(for plane strain).} \tag{2.15}$$

2.3.2 Elastic-Plastic Fracture Mechanics

In many cases, the plastic zone sizes are large compared to the crack size. Hence, linear elastic fracture mechanics is not applicable. In such cases, elastic-plastic fracture mechanics approaches are adopted.

Rice and Rosengren [93] proposed the J integral approach for a non-linear elastic solid. It is expressed as:

$$J = \int_{\Gamma} (W dy - T \frac{du}{dx} ds), \tag{2.16}$$

where Γ is an arbitrary counterclockwise closed contour in a stressed solid (Figure 2.7), ds is an element of Γ, T is the traction force perpendicular to Γ in an outward facing direction, u is the displacement in the x direction and W is the strain energy density. Begley and Landes [9, 16] have shown that J provides a measure of the driving force for crack growth under elastic-plastic fracture mechanics conditions.

Rice [92] defined the J integral as the change in potential energy for a virtual crack extension, for a nonlinear elastic solid. It is a path-independent integral that depends on the determination of an energy term, which shows the change in potential energy, when a crack is virtually extended by a distance. It is analogous to the strain energy release rate, G, which is applied under the linear elastic condition. For a linear elastic material, $J = G$.

Hutchinson [48] proposed the following two conditions for J dominance for the J integral to be applicable:

1. The J_2 deformation theory of plasticity must give an adequate model for the small-strain behavior of real elasticplastic materials under the monotonic loading.

2. The regions in which finite strain effects are significant and the region in which microscopic processes happen must be contained within the region of the small-strain solution dominated by the singularity fields.

2.3.3 Interfacial Fracture Mechanics

Crack growth and fracture at the interfaces of dissimilar materials is complicated. This is due to the oscillation singularity of the crack-tip fields for cracks at the interfaces in the presence of mode mixity.

The most basic relations for interface crack growth are as follows. The amplitudes of the normal and shear stresses on an interface, distance x ahead of a plane strain interfacial crack, are characterized by two stress intensity factors, K_I and K_{II}.

$$\sigma_{22} = K_I/\sqrt{2\pi x} \tag{2.17}$$

$$\sigma_{12} = K_{II}/\sqrt{2\pi x} \tag{2.18}$$

The two stress intensity factors can be combined to formulate two alternative parameters, the energy release rate, G, and the mode mixity angle, ψ. They are found to form a more convenient practical measure of interface crack growth. The

energy release rate, G, is given by:

$$G = \frac{1}{2}(\frac{1-\nu_1^2}{E_1} + \frac{1-\nu_2^2}{E_2})(K_I^2 + K_{II}^2), \tag{2.19}$$

where the subscripts 1 and 2 denote the two dissimilar materials and the subscripts I and II denote Modes I and II. The other is the mode mixity angle, ψ, defined as:

$$\psi = tan^{-1}(\frac{K_{II}}{K_I}) \tag{2.20}$$

Hutchinson and Suo [92] defined the criterion for crack growth, when G reaches a critical value, the interfacial toughness G_i. The investigation by Cao and Evans [11] and the study by Soboyejo et al. [98], both presented that the toughness changed appreciably with mode mixity. The above phenomena could be caused by crack-tip shielding by ductile ligaments; plastic dissipation in the substrate; and friction at asperities at the crack surfaces. Evans and Dalgleish [25] presented that the crack could either grow along the interface or inside the substrate materials. The crack-path selection criteria for cracks between dissimilar solids depend on the ratio of interfacial toughness, G_i, to the substrate toughness, G_s, of the adjoining material and the mode mixity angle, ψ.

2.4 Thin Film Fracture Mechanics

When the applied stress is bigger than the critical stress, fracture occurs in the layered materials. Residual stress can cause crack to grow in the film and along the

interface between the films and the substrates in the layered thin films on stretchable substrates. If the substrate is not compliance enough, crack can also grow in the substrate.

The stress on the stretchable thin films is due to two reasons: one is the thermal mismatch between the film and the substrate, the other is the pre-stretch of the substrate. Stretchable thin films are generally wrinkled or buckled. Buckling can also cause delamination of thin films from elastomeric substrates.

Hutchinson and Suo [47] have shown that when compressive stresses in the films exceed the critical buckling stress, the film can buckle away from the substrate, for a given interfacial crack length. Angstrom-scale periodic buckling patterns have been observed in the free-standing grapheme bi-layered thin films produced by liquid-phase processing [77], while non-sinusoidal surface profiles of buckled gold thin films have been observed on the elastomeric substrates [28]. A combination of experiments and models have been used to explain the finite width effects [51], while the deformation of a stretchable single crystal silicon has been investigated on the elastomeric substrates [55].

Domokos et al. [20] have used analytical and computational methods to study the elastic buckling of an inextensible beam with fixed end displacements, restricted to the plane, and in the presence of rigid, frictionless side-walls. Holmes [85] has also studied the buckling of an inextensible rod with free ends, restricted to the plane, and in the presence of distributed body forces derived from a potential. The effects of plasticity on buckling patterns in thin films on the elastomeric substrates have

also been investigated using finite element simulations that reveal different patterns of buckling [116].

The strain-to-wrinkling has been modeled in the literature on thin films on stretchable electronics. Analytical solutions [51, 103] have also been used to predict critical strains for the onset of wrinkling of thin films during the pre-straining of polymeric substrates with small and large pre-strains [51, 59, 103, 113]. Furthermore, a nonlinear buckling model has been used by Jiang et al. [51] to obtain the analytical solution for buckled geometries and maximum strain in the buckled thin film. Sun et al. [103] have also studied the incompressible substrate deformation of a folding wrinkled structures using neo-Hookean non-linear elasticity, while Huang [44] has shown the wrinkle formation in the films bonded to compliant substrates using nonlinear analyses. The wrinkling was caused by the compressive stresses [15] that buckled the films on polymeric substrates after deposition.

Significant work has been reported on the deformation of nanotube thin films on the stretchable substrates. Harris et al. [61] have presented the electronic and optical properties of thin films of single-walled carbon nanotubes on the polymeric substrates. Their studies of failure mechanisms revealed big differences in wrinkling of thin films. Hobbie et al. [38] have shown that the dominant wavelength of the wrinkled structures of single-wall carbon nanotubes deposited on pre-strained poly (dimethylsiloxane) (PDMS) decreases with pre-strain, while Wang et al. [111] have reported that the amplitude and periodicity of buckled graphene films on flexible substrates reduce with the increase of the pre-strain.

In the case of self-assembled materials, Ramanathan et al. [85] have studied the effects of confinement on the wrinkling of structures produced under compressive strains. Wang et al. [112] have also conducted the experimental studies of fracture in the self-assembled gold nanoparticle layers on polymeric substrates. They showed that the fracture strength of the gold nanoparticles increases when the size of the particles increases, but decreases when the layer thickness increases.

In the case of gold thin films deposited on the pre-strained PDMS substrates, Fei et al. [28] have studied the profile of gold-PDMS structure by using experiments and finite element models. They showed that the profiles depend on the film thickness, the level of pre-strain and the rate at which the strain is released. Hence, the different profiles of thin-film coated PDMS substrates can be attributed to the effects of strain localization, when the pre-strain exceeds the critical strain. Ebata et al. [24] have also shown that the amplitude of the folded, wrinkled, and delaminated profiles of such structures depend on the applied strain.

2.5 Lamination of Electronic Structures

Several deposition techniques have been used for the fabrication of low-cost organic solar cells and organic light emitting devices [33, 43, 67, 69, 124]. These include: cold welding [1]; transfer printing [108] and lamination [33, 43, 69, 124] techniques. In the case of lamination processes, deposition parameters, such as applied force for pre-lamination, pull-off force and surface roughness must be controlled for successful lamination [12, 108].

In most cases, the presence of particles in the clean room environment (e.g. silicon, dust and organic materials) can not be ignored. Such particles are trapped at the interfaces between the layers during the fabrication of organic light emitting devices and organic solar cells [12]. This leads to the formation of microvoids and partial contacts at the interfaces between the layered electronic structures [1, 12].

Furthermore, during lift-off (separation of stamp from the transferred layer) in the lamination process, stress concentrations occur at the edges of the entrapped voids/cracks. Since these can result in the interfacial plasticity or cracking, it is important to understand the stresses and crack driving forces associated with the prelamination and pull-off stages. It is also important to identify the processing windows for the contact and pull-off, without damage to organic electronic devices.

Since organic solar cells and organic light emitting devices require charge transport across their layered interfaces (Figure 2.8), the entrapped voids/cracks that are formed during contact and lamination processes can limit charge transport across the interfaces [50]. Conversely, the improved contact between the adjacent layers can be improved by increased pressure and interfacial adhesion. This can result in improved charge transport across the layered structures that are relevant to organic solar cells and organic light emitting devices. However, excessive pressure can also result in the sink-in of the interfacial impurities, as well as damage to the devices [21]. There is, therefore, a need for process models to guide the design of lamination processes.

Prior work [33, 43, 69] has been conducted on the lamination of solar cells, light emitting devices and flexible batteries. Lee et al. [69] have shown the lamination of

top electrode on the semitransparent organic photovoltaic cells. They demonstrated that the top electrode can be laminated for improved electrode performance without necessarily causing damage on the underlying device. Guo et al. [33] have also shown that a low temperature lamination process to fabricate the high performance Polymer Light Emitting Diodes (PLEDs). The interfacial properties of the laminated layered devices were enhanced by using the template activated surface. Huang et al. [43] have also presented a one-step process for the fabrication of semi-transparent polymer solar cells. These were fabricated by applying a glue-based lamination process combined with interfacial modification. Furthermore, Hu et al. [41] have used a lamination process to integrate Li-ion battery materials into a single sheet of paper. Hence, lamination technique can be used for the fabrication of high performance and low-cost electronics.

In order to improve the interfacial adhesion and contact in the laminated bi- and multi-layered structures of organic and inorganic electronic devices, Cao et al. [12] and Akande et al. [1] have developed cold welding techniques for the joining of gold-gold and gold-silver thin films. Enhanced interfacial adhesion (of gold-silver films) can be engineered in the presence of dust particles along the cold-welded interface. Tucker et al. [108] have also used a computational approach to improve the quality of film transferred during the lamination of electronic devices.

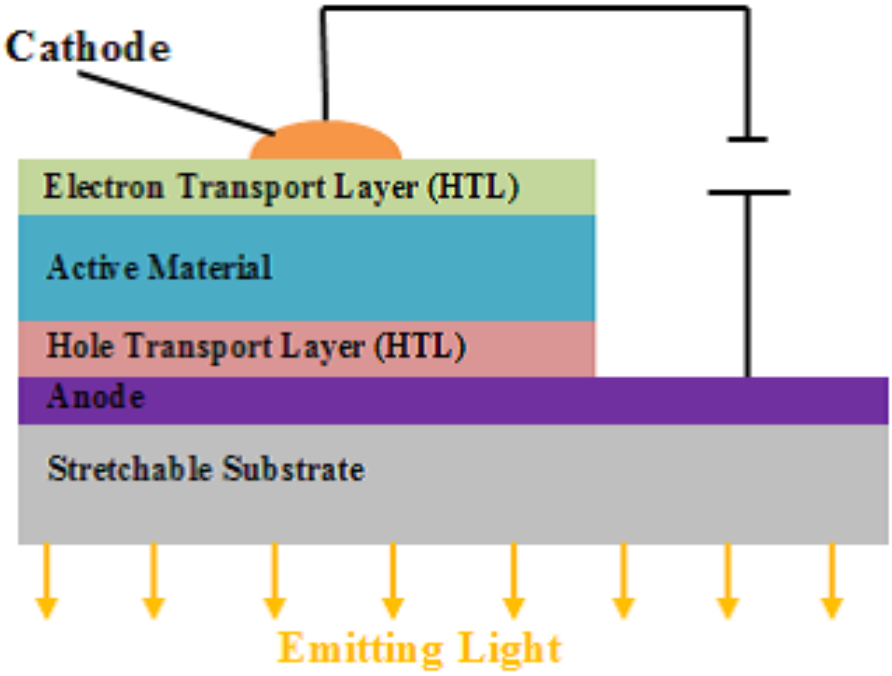

Figure 2.1: Schematic of a typical structure of stretchable light emitting devices.

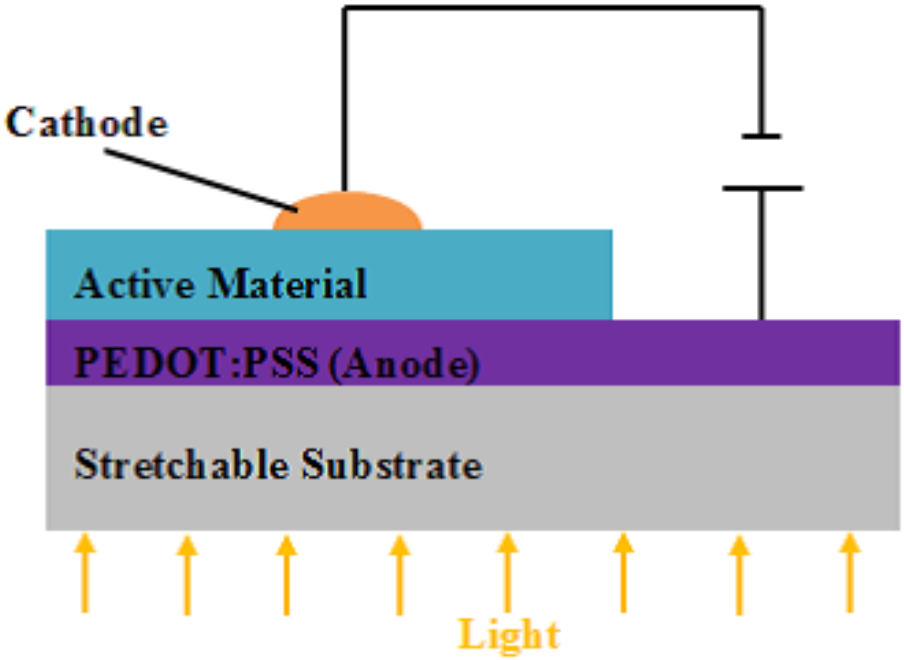

Figure 2.2: Schematic of a typical structure of stretchable organic solar cell.

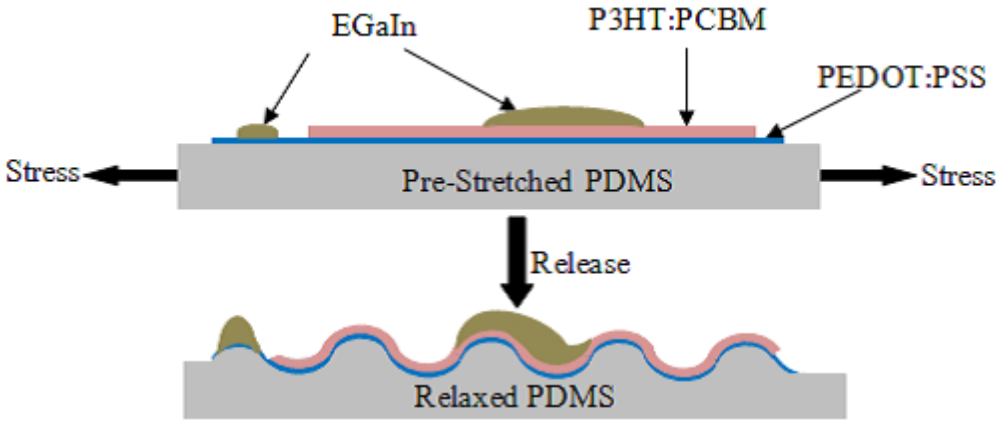

Figure 2.3: Stretchable organic solar cells

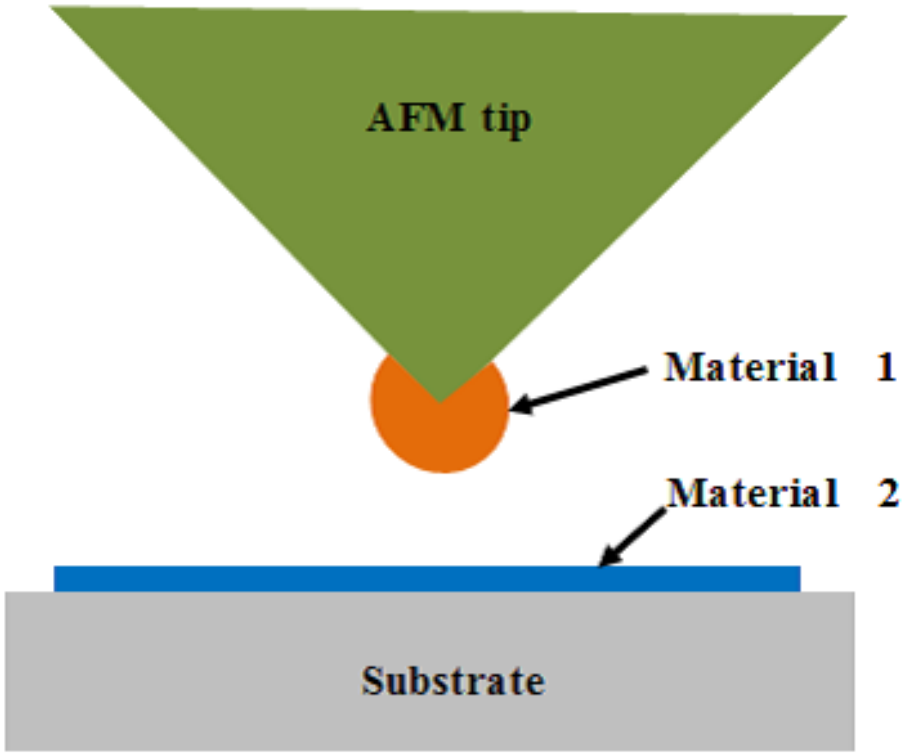

Figure 2.4: AFM adhesion measurement configuration.

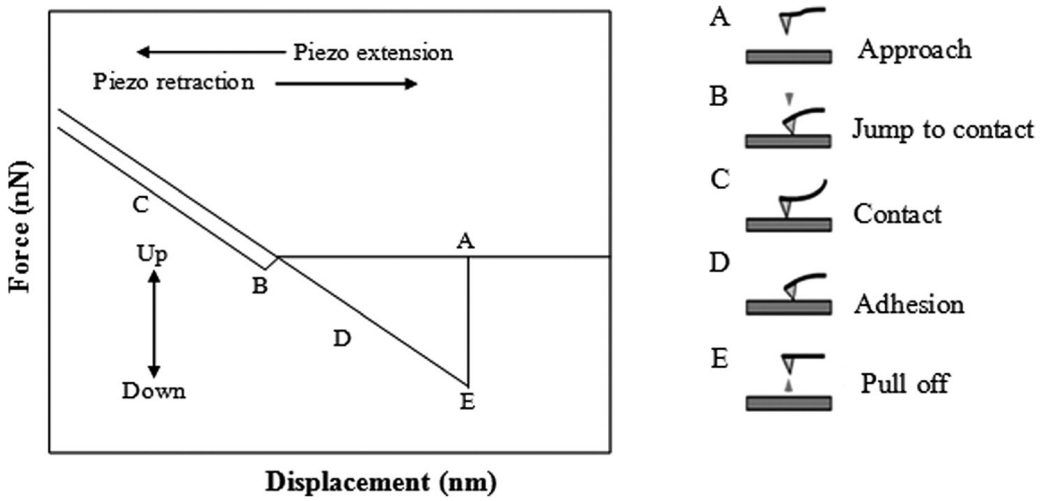

Figure 2.5: Schematic of force-displacement curve for various stages from A to E [94].

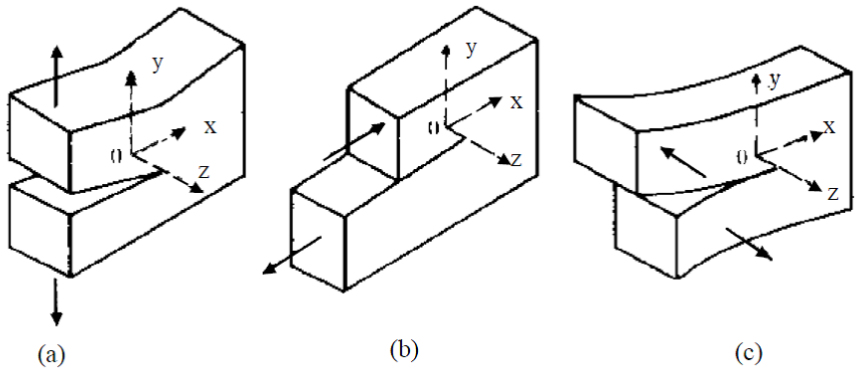

Figure 2.6: Modes of crack growth: (a) Mode I; (b) Mode II; (c) Mode III [99].

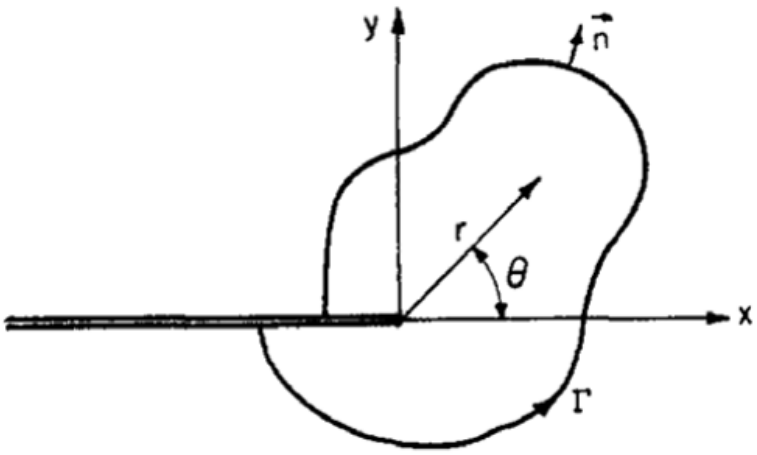

Figure 2.7: Schematic of the components of the path independent J integral [93].

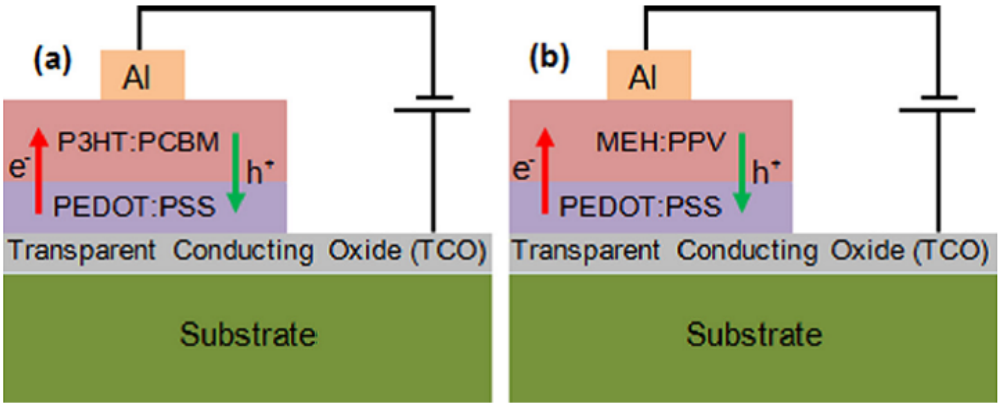

Figure 2.8: Schematics of (a) OPV structure and (b) OLED structure.

Chapter 3

Micro-wrinkling and Delamination-induced Buckling of Stretchable Electronic Structures

This chapter presents the results of experimental and theoretical/computational micro-wrinkles and buckling on the surfaces of stretchable poly-dimethylsiloxane (PDMS) coated with nano-scale Gold (Au) layers. The wrinkles and buckles are formed by the unloading of pre-stretched PDMS/Au structure after the evaporation of nano-scale Au layers. They are then characterized using atomic force microscopy and scanning electron microscopy. The critical stresses required for wrinkling and buckling are analyzed using analytical models. The possible interfacial cracking that can occur along with film buckling is also studied using finite element simulations of the interfacial crack growth.

To sum up, in this work, we conducted experiments and developed models to study the micro-wrinkling and delamination-induced buckling in the thin film structures consisting of nano-scale Au films coated onto the surfaces of stretchable PDMS substrates. Our experiments and theoretical/computational analysis lead to the three important results below:

- The wavelengths of the micro-wrinkled and buckled profiles decrease with increasing pre-strain.
- The critical buckling stress decreases with increasing wavelength of the profile.
- The measurements of interfacial fracture toughness obtained for Au films on PDMS substrates are comparable to AFM measurements of adhesion energy.

Based on these results, we also discussed the implications of micro-wrinkle and buckle formation on design and fabrication of micro-scale features in the stretchable electronic and biomedical structures.

3.1 Introduction

Stretchable electronics have emerged as interesting technologies for several applications in which stretchability is considered important [58–60, 64–66, 73, 87, 101, 102, 110, 118, 119]. These applications include stretchable electrical inter-connects [58, 59, 64, 65, 73], optical sensors and diffraction gratings [60, 119], metrology for the measurement of elastic moduli [101, 102], templates for device fabrication [118], stretchable electronics [58, 65, 76, 114], micro-contact printing

stamps [87,110], cell culture substrates [66], and surfaces for cell contact guidance [52] in implantable biomedical devices.

However, mechanical flexibility is a pre-requisite to achieve organic and inorganic [58, 59, 64, 68, 73] stretchable electronics, where wrinkling and buckling deformations are used to create wavy, out of plane structures, which can accommodate strain. This is done by pre-stretching the substrates [58, 59, 102] before the deposition of the devices. The wrinkled and delamination induced buckled structures of the devices are formed due to thermal compressive residual [46, 80, 113, 114] and pre-stretch stresses [58, 59, 102]. The formation and deformation of wrinkling of thin films can initiate failure, which can lead to delamination [24] in layered structures of stretchable electronics. Prior work by Rogers et al. [58, 64, 68, 103] has identified the importance of buckling as a strategy for achieving stretchable electronics, stretchable optoelectronic devices, stretchable integrated systems, stretchable metallic interconnect, and emerging stretchable curvilinear systems for biomedical applications. The formation of wrinkles of thin film-coated polymeric structures has also been observed by Watanabe [113] for checkerboard patterning.

In the case of wrinkling, layered devices adhere to substrate, upon release of pre-strain. During service conditions, by stretching the wrinkled structure below the critical prestrain levels, the wavy structures will become plane, while the interfacial contact remains intact. However, the nucleation and growth of cracks along the interfaces can cause interfacial failure to occur under static or cyclic loading conditions above threshold conditions. This can lead ultimately to adhesive or cohesive failure. Mei and Huang [80] and Ebata et al. [24] have shown that

the wrinkled surfaces are formed due to compression-induced buckling instability of thin films, which can lead to interfacial cohesive failure and delamination. On the other hand, a buckled morphology of the layered structure can occur in the presence of interfacial voids, before and after the release of the pre-stretch. This failure mode can also occur due to merging of the possible micro voids that can lead to delamination [24, 80]. Interfacial cracks are also formed from sandwiched dust particles [1] and bubbles [83] between the deposited films and substrates. Residual stress can also drive the delamination of the layered structures from substrate. The interfacial cracks then grow under static or cyclic loading conditions until critical conditions are reached. It is, therefore, important to study the possible interfacial adhesion and contact of micro-wrinkled and buckled structures.

In an effort to further understand the mechanics of thin films on elastomeric substrates, Hutchinson and Suo [47] have shown that when compressive stresses in the films exceed the critical buckling stress, the film can buckle away from the substrate, for a given interfacial crack length. Angstrom-scale periodic buckling patterns have been observed in freestanding graphene bilayers generated by liquid-phase processing [77], while non-sinusoidal surface profiles of buckled gold thin films have been observed on elastomeric substrates [28]. Furthermore, finite width effects have been elucidated using experiments and models [51], while the deformation of a stretchable single crystal silicon has been studied on elastomeric substrates [55]. Theoretical and numerical schemes have been used by Domokos et al. [20] to study the elastic buckling of an inextensible beam with fixed end displacements, restricted to the plane, and in the presence of rigid, frictionless side-walls. Holmes et al. [39]

have also studied the buckling of an inextensible rod, restricted to the plane, with free ends, and in the presence of distributed body forces derived from a potential. The effects of plasticity on buckling patterns in thin films on elastomeric substrates have also been studied using finite element simulation to reveal different patterns of buckling [116]. The delamination-induced buckling of semiconductor nano-ribbons (on the surfaces of elastomers) can be precisely controlled [103] with periodic, inactivated, and activated regions. Ordered buckled structures can also occur on thin metal films, due to the thermal contraction of elastomeric polymer substrates [6]. Furthermore, the controlled formation of ordered, sinusoidal wrinkles has also been associated with the effects of plasma oxidation of a compliant polymer [7]. Periodic sinusoidal structures have also been developed for buckled ribbons of piezoelectric ceramic (PZT) [88] and tunable diffraction gratings [118]. In an effort to develop robust systems for stretchable electronics, the level of strain-to-wrinkling had been modeled in literature. A well-known analytical solution [51, 103] has been used to predict critical strain for the onset of wrinkling of thin films on pre-strained polymeric substrates with small and large pre-strains [51, 59, 80, 103, 113]. Jiang et al. [51] have obtained the analytical solution for the buckling geometry and maximum strain in buckled thin film using nonlinear buckling model. Sun et al. [103] have also analyzed the incompressible substrate deformation of a folding wrinkled structures using neo-Hookean non-linear elasticity, while Huang et al. [44] have presented nonlinear analyses of wrinkle formation in films bonded to compliant substrates. The wrinkling was due to compressive stresses [15], which buckled the films on the polymeric substrates after deposition. Significant efforts have been

reported on nanotubes on stretchable substrates. Harris et al. [34] have reported the electronic and optical properties of thin films of single-walled carbon nanotubes on polymeric substrates. They had studied the underlying failure mechanisms, for significant differences in the electronic manifestations of the thin films using wrinkling. Hobbie et al. [38] have also reported that the dominant wavelength of the wrinkled structures of single-wall carbon nanotubes deposited on pre-strain poly(dimethylsiloxane) (PDMS) decreases with pre-strain, while Wang et al. [111] have shown that the amplitude and periodicity of buckled graphene films on flexible substrates reduce with the increasing in prestrain. In the case of self-assembled materials, Ramanathan et al. [91] have described the role of confinements on wrinkling structures using compressive strains. Wang et al. [112] have presented the experimental investigation of fracture in self assembled gold nanoparticle layers on polymeric substrates. They showed that the fracture strength of the gold nanoparticles increases as the size of the particles increases, but decreases as the layer thickness increases. In case of thin films of gold deposited on pre-strained PDMS substrates, Fei et al. [28] have analyzed the profile of gold-PDMS structure using experiments and finite element models. They showed that the profile of the structure depends on film thickness, the level of pre-strain and the rate at which the strain is being released. Therefore, the different profiles of thin-film coated PDMS substrates can be attributed to the effects of strain localization, when the pre-strain exceeds the critical strain. Ebata et al. [24] have also shown that the amplitude of the wrinkled, folded, and delaminated profile of such structures depends on the applied strain. However, there are no prior studies that use the occurrence

of wrinkling and delamination-induced buckling in the combined measurement of film elastic properties and interfacial fracture toughness between thin metal films and elastomeric substrates. This is done in this chapter using the results of a combined analytical, computational, and experimental study of micro-wrinkling and interfacial fracture of the delamination-induced buckling of nano-scale Au films on elastomeric poly-dimethylsiloxane (PDMS) substrates that are relevant to stretchable electronics and implantable stretchable biomedical devices. Analytical models are used to determine the critical stresses required for wrinkling and delamination-induced buckling in the structures. Interfacial fracture mechanics concepts are also used to determine the interfacial fracture toughness between the Au films and the PDMS substrates. The implications of the results are then discussed for the design of stretchable electronics and biomedical devices.

The rest of this chapter is divided into five sections. Following the introduction in Section 3.1, the models are presented in Section 3.2 before describing the experimental and computational methods in Section 3.3. The results and discussion are then presented in Section 3.4, before summarizing the salient conclusions from this work in Section 3.5.

3.2 Theory

There are three models that need to be presented to form the theoretical base for the work of this chapter: (i) the theory of interfacial adhesion between two dissimilar materials; (ii) analytical models of the wrinkling and buckling of thin films on

stretchable substrates; and (iii) interfacial fracture mechanics models of crack growth between layers.

3.2.1 Atomic Force Microscopy (AFM) Force Measurement

The adhesion force between two materials can be measured by contact mode AFM [3, 106]. First, the AFM tip is coated with one material. The substrate is then coated with the second material in the bi-material pair. The steps for measuring the adhesion force are illustrated in Figure 3.1, along with a force-displacement curve associated with the tip deflection (A-E). The displacement of the AFM cantilever tip begins (at point A) above the substrate. As the tip is lowered towards the substrate, it will jump to contact (point B). Subsequent deflection of the tip is associated with elastic bending, as the tip is deflected (point C) to a maximum force/displacement. The tip deflection is then reversed until the tip is separated from the substrate (point E). The adhesion force, F, is determined from Hooke's law to be

$$F = -kx, \tag{3.1}$$

where x is the tip displacement (AE) and k is the spring constant of the AFM tip, which was measured using the thermal tune method [49].

3.2.2 Adhesion Energy

There are several possible theories that can be used to estimate the adhesion energy. These include: the Derjaguin-Muller-Toporov (DMT) model [19]; the

Johnson-Kendall-Robert (JKR) model [53]; and the Maugis-Dugdale (MD) model [78]. A non-dimensional parameter is determined to distinguish the use of these adhesion energy models [19, 49, 53, 78]. If the parameter is smaller than 0.1, the DMT model applies. If it is greater than 5, the JKR model applies. The intermediate values correspond to the MD model. The DMT model applies to cases in which there are weak interactions between stiff materials with small radii. The application of the DMT model to similar scenarios was reported initially by Rahbar *et al.* [89]. This was extended by Meng *et al.* [81]. to the study of adhesion in multilayered drug-eluting stents. The adhesion energy, γ, is related to the adhesion force, F, by the following expression:

$$\gamma_{DMT} = \frac{F_{adhesion}}{2\pi R}, \tag{3.2}$$

where R is the effective radius which is given by

$$R = (\frac{1}{R_{rms}} + \frac{1}{R_{tip}})^{-1}, \tag{3.3}$$

where R_{rms} and R_{tip} are the radii of the average roughness of the substrate and the coated AFM tip, respectively.

3.2.3 Residual and Applied Stresses

The controlled formation of wrinkles and buckles for applications in stretchable electronics involves the deposition of thin films onto pre-stretched substrates [58, 59, 64, 65, 73, 76]. The film is subject to stresses due to two factors. One is from

the thermal expansion mismatch between the film and the substrate, while the other is from the pre-stretch of the substrate. These stresses are responsible for the induced wrinkling and buckling. The residual stress, σ_{th}, due to the thermal expansion coefficient mismatch is given in [3]:

$$\sigma_{th} = [E_f(\alpha_f - \alpha_s)(T_d - T)]/(1 - \upsilon_f), \tag{3.4}$$

where E_f and υ_f are Young's modulus and Poisson's ratio of the film; α_f and α_s are the thermal expansion coefficients of the film and the substrate respectively; T_d is the deposition temperature, and T corresponds to the room temperature. The stress, σ_{app}, due to the release of the applied prestretched substrate can be approximated as

$$\sigma_{app} = E_f \varepsilon_{pre}, \tag{3.5}$$

where ε_{pre} corresponds to the pre-strain. By applying the principle of linear superposition, the total stress in the film can be obtained from the summation of Equations. (3.4) and (3.5). This is given by

$$\sigma_R = \sigma_{th} + \sigma_{app} = [E_f(\alpha_f - \alpha_s)(T_d - T)]/(1 - \upsilon_f) + E_f \varepsilon_{pre}. \tag{3.6}$$

Equation (3.6) is the total stress that is responsible for wrinkling and delamination-induced buckling in the thin film deposited on a pre-stretched polymeric substrate.

3.2.4 Wrinkling and Buckling Models for Stretchable Electronics

As described above in Section 3.2.3, wrinkled and buckled structures are formed as a result of the total stress on the film. The film starts wrinkling or buckling when the induced stress reaches a critical value. The solutions of the critical stress, σ_c, for the onset of wrinkling or buckling of thin films are given in [59, 102, 113]:

$$\sigma_c = (\frac{E_f}{1-\upsilon_f^2})^{1/3}(\frac{3E_s}{8(1-\upsilon_s^2)})^{2/3}, \tag{3.7}$$

where E_f and E_s are the Young's moduli of the film and the substrate, υ_f and υ_s are the Poisson's ratios of the film and the substrate. Also, the buckling of thin metallic films on stretchable elastic substrates has been modeled by Hutchinson and Suo [47]. The critical stress can be expressed as a function of wavelength of the buckling [3,47]. This is given by

$$\sigma_c = \frac{\pi^2 h^2 E_f}{3\lambda^2(1-\upsilon_f^2)}, \tag{3.8}$$

where λ is the wavelength of the buckle, E_f is the film Young's modulus, υ_f is the film Poisson's ratio, and h is the film thickness.

3.2.5 Interfacial Fracture Mechanics

In this section, interfacial failure is modeled at the onset of buckling of thin films on PDMS substrates. The theoretical expressions are presented for the energy release rates and the adhesion energies. It is assumed that films that are deposited on

pre-stretched substrates can delaminate due to buckling [47], sandwiched particles and voids [83].

3.2.5.1 Analytical Modeling

The buckling of thin metallic films is often accompanied by the delamination of the films from the substrates. The buckled profiles can be analyzed using interfacial fracture mechanics. The energy release rate, G, of the interfacial crack is given in [47]

$$G = \frac{(1 - v_f^2)h}{2E_f}(\sigma_R - \sigma_c)(\sigma_R + 3\sigma_c), \tag{3.9}$$

where E_f and σ_f are the Young's modulus and the Poisson's ratio of the Au film, h is the thickness of Au film, σ_R is the residual stress in the film, and λ_c is the critical buckling stress. Ebata et al. [24] have shown that the residual stress increases with increasing amplitude of the buckling, as delamination proceeds. The thin film starts to delaminate from the substrate when the total stress (σ_R) is more than the critical stress (σ_c) for buckling. Hence, the interfacial energy release rate, G, increases with increasing σ_R and approaches its critical value, G_c, which is given by

$$G_c = \frac{(1 - v_f^2)h\sigma_R^2}{2E_f}. \tag{3.10}$$

However, the interfacial adhesion between two dissimilar materials involves interactions between atoms on the two surfaces to form secondary bonds. The true

work of adhesion between the film and the substrate materials is given by [3, 31, 106]

$$G_{adhesion} = G_{elastic} = \gamma_f + \gamma_s - \gamma_{f-s}, \tag{3.11}$$

where γ_f and γ_s are the surface energies of the film and substrate separately, while γ_{f-s} is the surface energy between the film and the substrate in contact. If the bonds were broken mechanically, high interfacial fracture energies can be obtained due to the contributions from plastic deformation. However, if the contributions from plasticity are small, then the adhesion energy can be approximated as the interfacial fracture energy [31] between the two different materials.

From a fracture mechanics perspective, the measured adhesion energy, γ, corresponds to the critical mode I energy release rate [106]. This is possible because the fracture mechanics approach uses the applied strain energy release rate to measure the practical work of adhesion [31]. Hence, $G_c \approx \gamma$. The critical interfacial energy release rates can also be computed using commercial software packages, such as ABAQUS^{TM}, which was used in this study (ABAQUS 6.12, Dassault Systèmes Incorporation, Rhoda Island). This involves introducing the geometry, materials properties, and the boundary conditions of the bi-layered system into the software. In this case, the rate of the energy released at the tip of the onset interfacial crack is denoted by G_{comp}.

3.3 Materials and Methods

3.3.1 Experimental Methods

3.3.1.1 Formation of Wrinkled and Micro-buckled Au on PDMS Substrates

First, the PDMS substrate was prepared by mixing a Slygard 184 silicone elastomer curing agent with a Slygard 184 silicone elastomer base (Dow Corning Corporation, Midland MI) in a 1 : 10 weight ratio. Then, the mixture was processed under a vacuum pressure of 6 kPa for 30 minutes to remove all visible bubbles. The processed PDMS was poured into an aluminum mold with a dog-bone shape. This was followed by annealing in an oven at 80 ℃ for 2 hours to form a 1 mm thick substrate. The PDMS was fixed with clamps at both ends and prestrained to different levels (18%, 36% and 70%) on a hard steel substrate. A 5 nm thick of chromium (Cr) adhesive layer was then deposited onto the PDMS substrate using Denton evaporator (Denton DV 502 A, Denton Vacuum Moorestown, NJ). Chromium layer was used to improve the interfacial adhesion between the Au-film and the substrate. A gold thin film layer with a thickness of 100 nm was then deposited on top of the chromium layer. After deposition, the two ends of the PDMS substrate were released, and the wrinkle/buckle patterns were formed spontaneously in the gold thin films.

3.3.1.2 AFM adhesion Measurements

The interfacial adhesion in the layered Au-Cr-PDMS structure was measured using AFM. First, etched silicon contact mode AFM tips were purchased from Veeco

Instruments Woodbury, NY. The AFM tips were then coated with Au and Cr separately, while Au was deposited on glass substrates using Denton evaporator (Denton DV 502A, Denton Vacuum, Moorestown, NJ). With these coated tips and substrates, the adhesion forces between Cr/PDMS (Cr-coated tip versus PDMS), Cr/Au (Cr-coated tip versus Au-coated glass), and Au/PDMS (Au-coated tip versus PDMS) interfaces were measured. AFM measurements were performed in air over a temperature range of $22 \sim 25$ ℃ and a relative humidity range of $31 \sim 46\%$.

The tests were carried out in a Bruker Instruments Dimension 3000 AFM (Bruker Instruments, Plainview, NY). About ten force-displacement curves were obtained for each interaction. The tip deflections were obtained from the curves. The spring constants of each of the tips were measured using the thermal tune method [97]. This was done using a Bruker Instruments Nanoscope IIIa AFM (Bruker Instruments, Plainview, NY). With the measurements of the tip deflections and the spring constants, the adhesion forces were finally obtained from Hooke's law (Eq. (3.1)). Due to the high sensitivity of AFM measurements to surface roughness, the substrate roughnesses and the tip radii were measured for each interaction pair. The surface roughnesses were obtained by AFM in the tapping mode. About 10 height and phase images of each substrate were obtained. These were used to measure the root mean squared roughnesses. The tip radii were calculated (before and after measurement) from images obtained using a scanning electron microscope (SEM,Philips FEI XL30 FEG-SEM, Hillsboro, OR). The measurements of the surface roughness and the tip radii were used to calculate the adhesion energies from Eqs. (3.2) and (3.3).

3.3.2 Computational Methods

Computational methods were used to study the failure mechanisms in the thin films of Au on PDMS substrates due to wrinkling and buckling. These were used to provide insights into the experimental results. First, the stress distributions in the wrinkled Au-films were simulated using the ABAQUS^{TM} software package (ABAQUS 6.12, Dassault Systèmes Incorporation, Rhoda Island). The two ends of the Au-PDMS model were displaced (pre-strained) by 18%, 36% and 70% of the length of the structure. The modulus and Poisson's ratio of the Au films were maintained at 61 GPa and 0.35 [2], respectively. However, the Young's modulus of the PDMS substrate depends on the fabrication curing conditions and the mixing ratio of base and curing agent of the Slygard silicone elastomer [54]. Hence, in the finite element simulation, the modulus of the substrate was varied from 1MPa to 100MPa, with Poisson's ratio of 0.3 [2]. This was done to provide insights into the effects of substrate Young's modulus on the wrinkling profile.

In the case of delamination-induced buckling, it was assumed that there were pre-existing interfacial cracks between the Au-film and PDMS substrates. These cracks can be attributed to imperfections, such as voids, bubbles, or impurities that are present at the interfaces. The energy release rates at the tips of the cracks were computed in form of the path independent J-integral. These were determined as functions of crack length using the ABAQUS^{TM} software package for the three levels of pre-strains. Furthermore, for different interfacial crack lengths, the interfacial energy release rates were calculated as functions of the pre-strain.

Since the film thickness is very small compared to the thickness of the substrate, and the fact that the Young's modulus of the film is far greater than that of the substrate, fine mesh was used to model the Au/PDMS interface (as shown in Figure 3.2). Four-node plane strain quadrilateral elements were used. All the materials properties that were used were assumed to exhibit isotropic behavior, while the active contact Au/PDM S interface was maintained at zero rotation.

3.4 Result and Discussion

3.4.1 Wrinkling Profile As A Function of Pre-strain and Substrate Elastic Modulus

SEM images of the wrinkled profiles induced after the release of the pre-strained Au/PDMS samples are presented in Figures 3.3(a) and 3.3(c). The images show that the wavelengths of the wrinkled structure reduced from 9.7 μm, for a pre-strain of 18%, to 6.6 μm, for a pre-strain of 36%, and 3.0μm, for a pre-strain of 70%. This is presented clearly in Figure 3.4. The wavelengths are, therefore, inversely related to the pre-strain values. Furthermore, some transverse cracking was observed in the Au films, especially after pre-straining to a level of 70% (Figure 3.3(c)). The reduction in the wavelengths is attributed to the effects of the propagating transverse cracks, due to increasing pre-strain.

The von Mises stress distributions in the Au/PDMS structure are presented in Figures 3.5(a) and 3.5(d). These show the dependence of substrate elastic modulus on stress distributions and profile amplitude. The increase in the elastic modulus of

the substrate increases the concentration of stress in the wrinkled structure. Hence, the processing of stiffer PDMS substrates will increase the overall Mises stresses, as shown in Figures 3.5(a) and 3.5(d). Furthermore, the wrinkling profile became more well defined with increasing substrate Young's modulus (Figures 3.5(a) and 3.5(d)). However, there is a high possibility that failure would be induced by the higher Von Mises stresses in the Au/PDMS structures that have higher moduli. A balanced approach is, therefore, needed to obtain well defined wrinkled profiles without inducing failure.

3.4.2 Stress Analysis

3.4.2.1 Residual Stress

For the Au film deposited on a pre-stretched PDMS substrate, residual stresses were induced in the Au films due to the thermal expansion coefficient mismatch between the Au films and the PDMS substrate. The total stress in the Au films was also assumed to be the sum of the thermal mismatch stress and the stress due to pre-strained PDMS cohesive failure in the adhesion force measurement. Therefore, we conclude that the measured AFM pull-off forces correspond to adhesive failure. The average textured Young's modulus for the Au film has been obtained to be $\sim$ 61 GPa (Ref. [2]). The measured Young's modulus of the Au film was then incorporated into Eq. (3.4), along with the temperature difference ($\delta_T = T_d - T = 292K$), the Poisson's ratio ($\upsilon_f = 0.35$), and thermal expansion coefficients of the Au-film ($\alpha_f = 1.4\times10^{-5}/K$) and substrate ($\alpha_s = 3.14\times10^{-4}/K$). These were used to estimate the residual stress due to thermal expansion mismatch to be $\sim 0.583\ GPa$.

Table 3.1: Residual stresses due to effects of thermal expansion coefficient mismatch and pre-strained PDMS substrate.

pre-strain (%)	Applied stress σ_{app}(GPs)	Residual stress σ_R (GPa)
18	10.98	11.56
36	21.96	22.54
70	42.70	43.28

The stress due to the pre-strained PDMS substrate (Table 3.1) was calculated using Eq. (3.5). Hence, the sum of the two residual stresses (σ_R) was obtained using Eq. (3.6) for different thicknesses of the Au film. These results are presented in Table 3.1. These show that the calculated total stress increase with increasing pre-strain of the PDMS substrate.

3.4.2.2 Critical Stresses

The calculated critical stresses obtained for different wavelengths are presented in Figure 3.6(a). The critical stresses for the onset of wrinkling/buckling were estimated from the measured profiles (Figure 3.3 and Eq. (3.8)). The critical stress decreases with increasing wavelength and vice versa. Therefore, the critical stress is inversely related to the wavelength of the buckling/wrinkling profile. It is important to note that the transverse cracks can be attributed to the possible formation of a brittle silica-like layer in the near-surface region of the PDMS with the deposited Cr. However, in Figure 3.6(b), the critical stress increases with increasing substrate Young's modulus. Figure 3.6(b) was obtained from Eq. (3.7), for possible ranges ($1 \sim 100$ MPa) of PDMS Young's moduli. The limiting critical stress for the Au thin film on a specific stretchable substrate (of known modulus) can be predicted from

Table 3.2: Average surface roughness values

Surface (%)	Roughness (mm)
PDMS on glass	0.7 ± 0.1
Cr	9.9 ± 2.2
Au	3.4 ± 0.5

Figure 3.6(b). For example, in Figure 3.6(b) inset, the critical stresses of Au film on PDMS substrates with Young's moduli of 1 MPa and 4 MPa are approximately 0.024 GPa and 0.06 GPa, respectively.

3.4.3 Surface Roughness/Profile

The root-mean-squared (rms) roughnesses of the different layers in the Au-coated PDMS structures are presented in Table 3.2. The PDMS had an rms roughness of 0.7 ± 0.1 nm, while the Cr-coated surface had an rms roughness of 9.9 ± 2.2 nm. The Au film has an intermediate rms roughness of 3.4 ± 0.5 nm. The AFM tip radii measured from the SEM tip images averaged ~ 250 nm (Figure 3.7). Both the surface roughnesses and the AFM tips radii were used for computation of adhesion energies. In the SEM images, there were no significant changes observed in the AFM tips. The highest magnification SEM images did not reveal any evidence of cohesive failure in the adhesion force measurement. Therefore, we conclude that the measu red AFM pull-off forces correspond to adhesive failure.

3.4.4 Interfacial Adhesion and Fracture Energies

3.4.4.1 Measured Adhesion Forces and Energies

Adhesion forces between different layers in the Au-coated PDMS structure (Figure 3.8(a)) are presented in Figure 3.8(b). The highest adhesion force was obtained between the Cr (adhesion promoter layer) and PDMS. This had an average pull-off/adhesion force of 77 ± 29.3 nN. The high adhesion in Cr/PDMS interface could be due to highly electropositive nature of Cr. It is easy for electrons to be donated from Cr to methyl groups in the side chains of PDMS and form the surface dipoles that increase the attraction. An intermediate adhesion force of 30 ± 5.7 nN was obtained for the Cr-Au interaction, while the lowest adhesion was obtained for the PDMS-Au interaction.

In an effort to use the models described in Section 3.2.2, a non-dimensional parameter for the calculation of the adhesion energy was first found to be $\sim 10^{-6}$ (which is $\ll 0.1$) [28, 51, 77]. The DMT model was then used to determine the adhesion energies. The measured rms roughness value of surface 1 and the radius value of the AFM tip (surface 2) were incorporated into Eq. (3.3) to calculate the effective radius. The measured adhesion forces and the corresponding effective radii were then incorporated into Eq. (3.2) to calculate the adhesion energies. The results of these calculations are presented in Figure 3.8(c). Once again, the Cr interlayer exhibits the highest adhesion energy with the PDMS substrate. However, due to the roughness of the Cr layer, the adhesion energies of the Cr-Au couples are now comparable to those between PDMS and Au.

3.4.4.2 Interfacial Fracture Energies

The calculated interfacial energies obtained for different pre-strain values are summarized in Table 3.3. The ratios of the energy release rates, G, and the critical energy release rates, Gc, obtained from Eqs. (3.9) and (3.10), are plotted along with the analytical solutions in Figure 3.9. The ratios increase to a peak before decreasing to a steady-state value of about 1.0. This is comparable to results from earlier work by Hutchinson and Suo [47].

Table 3.3: Interfacial energy release rates obtained from analytical expressions for different pre-strains for cracks between Au films and PDMS substrates

pre-strain (ε)	$G_c(\mathrm{J}/m^2)$	$G(\mathrm{J}/m^2)$	$\sigma_R/\sigma_c)$	G/G_c
18.00	2.64	2.71	75.70	1.02
36.00	2.64	2.79	34.60	1.06
70.00	1.92	2.20	12.20	1.14

The energy release rates were also computed using ABAQUS^{TM}. Figures 3.10(a)-3.10(d) show plots of energy release rate as a function of interfacial crack length. These are presented for buckled Au films of different thicknesses. The interfacial energy release rates decrease continuously with increasing crack length in the case of the 100 nm Au films (Figure 3.10(a)). However, turning points were observed for thinner 50 and 75 nm Au films (Figures 3.10(b)-3.10(d)). In any case, steady state fracture toughness values were approached with increasing interfacial crack length. Also, the turning points corresponded to the onset of buckling, while the differences between the steady state energy release rate and the turning point energy release rate correspond to the interfacial energy for delamination due to buckling. For example, the computed interfacial energy for delamination of a Au/P

DMS structure with a typical thickness (50 nm) of the Au film is $\sim 3J/m^2$ under pre-strain value of 36% (Figure 3.10(d)). The von Mises stress distributions in the buckled Au films on PDMS substrates are presented in Figures 3.11(a)-3.10(e). The amplitude of the buckled film increases with increasing interfacial crack length. It also suggests that interfacial crack growth can be used to control the waviness of the buckled films prior to applications in stretchable electronics structures.

3.4.4.3 Comparison of Adhesion Energies and Energy Release Rates

The measured adhesion energies are comparable to the interfacial energy release rates obtained for PDMS-Au interfaces using both computational and analytical techniques. A comparison of the data is presented in Figure 3.12. Note that the measured adhesion energy of the PDMS-Cr interface was significantly greater than the corresponding calculated interfacial energies. This suggests that the interfaces with the lower interfacial fracture toughnesses dominated the delamination processes that occurred during the buckling of the films on the PDMS substrates.

3.4.4.4 Dependence of Interfacial Energy on Pre-strain and Film Thickness

For different ratios of interfacial crack lengths to film thicknesses ($2a/h$), the computed interfacial energy release rates are plotted as a function of pre-strain in Figure 3.13. In obtaining the ratios, the crack length was maintained constant, while the thickness of the film was varied. The energy release rates increase with increasing pre-strain. However, increasing pre-strain could also result in multiple

interfacial cracks, which can cause reduction in the wavelength of the Au-PDMS surface profile. This explains the reduction in the wavelength of the wrinkled Au film observed in Figure 3 for increasing the pre-strain of the PDMS substrate. According to Figure 3.13, for a thick film ($2a/h = 5$), a small pre-strain ($\sim 20\%$) will cause delamination due to buckling for a critical adhesion energy, $\gamma = 2.42 J/m^2$. However, the interfacial energy release rate between a relatively thin film ($2a/h = 90$) and the PDMS substrate is maintained below the critical value at a pre-strain of $\sim 70\%$.

3.4.5 Implications

First, this study suggests that a basic understanding of micro-wrinkle and buckle formation is useful in the design and fabrication of micro-scale features in opto-electronic and biomedical structures. In the case of opto-electronic structures, these may include diffraction gratings and electronic textiles, while potential biomedical applications may include implantable biomedical devices for sensing and drug delivery.

The ability to control the surface textures by micro-wrinkling and buckling may also provide biomedical electronic systems with the ability to integrate well with biological tissue. For example, prior work [14] has shown that microgrooves with depths and spacings of $\sim 10-20\ \mu m$ can promote the contact guidance/alignment of biological cells in ways that can lead to reduced scar tissue formation and increased cell/surface integration [32]. There is, therefore, the potential to tailor future wrinkled and buckled structures that can facilitate cell/surface interactions and integration with biological tissue.

The potential stretchable electronics which include solar cells and light emitting devices require the design of robust systems that are stretchable without significant interfacial failure [59]. There is, therefore, a need to extend the strain-induced micro-wrinkling and buckling testing technique to a more general framework for the measurement of thin film interfacial fracture toughness. These are clearly some of the challenges and opportunities for future work.

3.5 Summary and Concluding Remarks

This chapter presents evidence of micro-wrinkle and delamination-induced buckle formation in thin film structures consisting of nano-scale Au films coated onto the surfaces of stretchable PDMS substrates. The wavelengths of the micro-wrinkled and buckled profiles decrease with increasing pre-strain. The critical buckling stress also decreases with increasing wavelength of the profile. The pre-strain technique was used for the measurement of the interfacial fracture toughness between hard and soft materials. The measurements of interfacial fracture toughness obtained for Au films on PDMS substrates are comparable to AFM measurements of adhesion energy. The results suggest that pre-strain-controlled profiles can be considered for potential biomedical and optoelectronic applications.

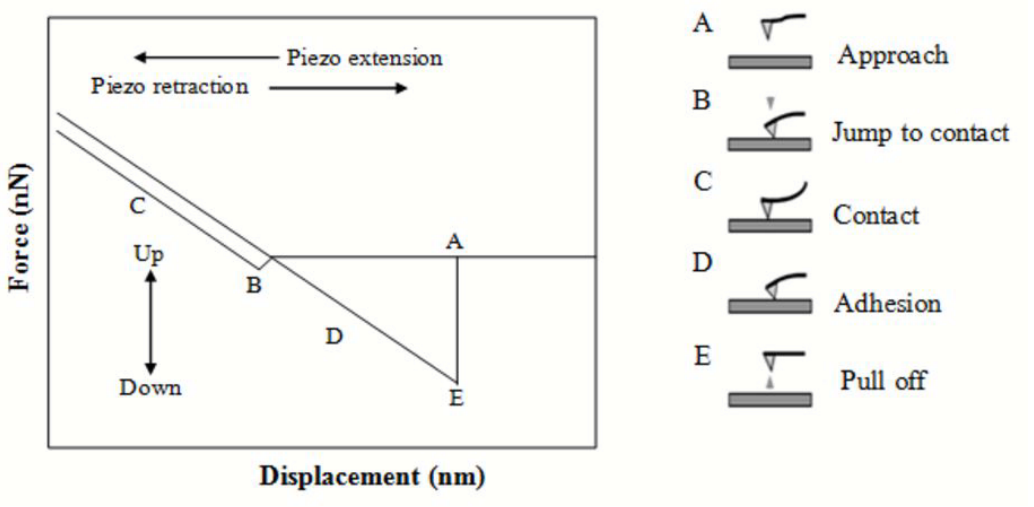

Figure 3.1: Schematic force-displacement curve for various stages of AFM measurement from A to E.

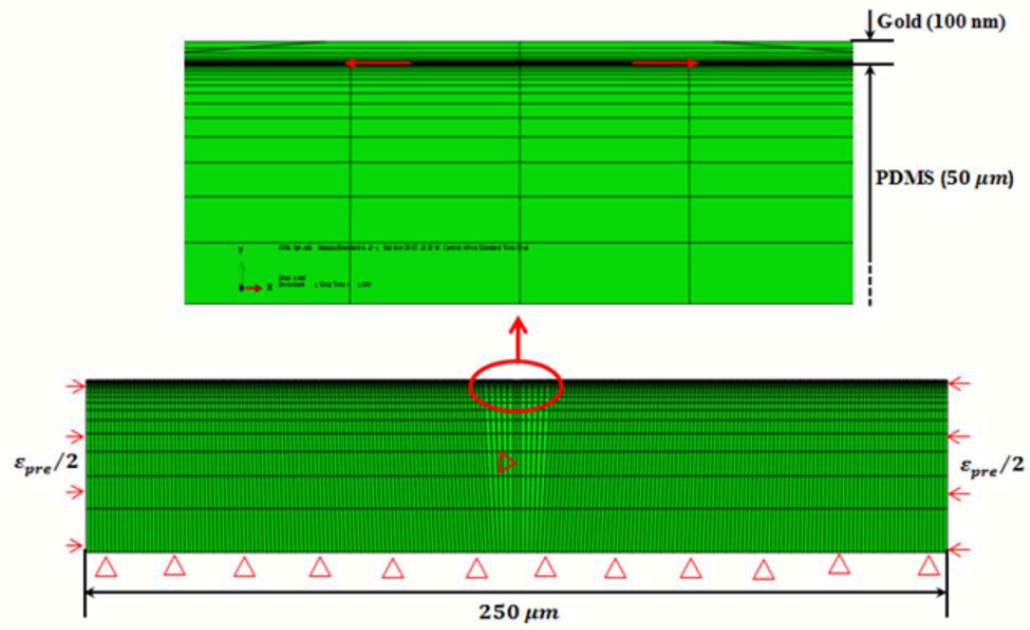

Figure 3.2: Finite element model of buckling of thin gold film on PDMS substrate.

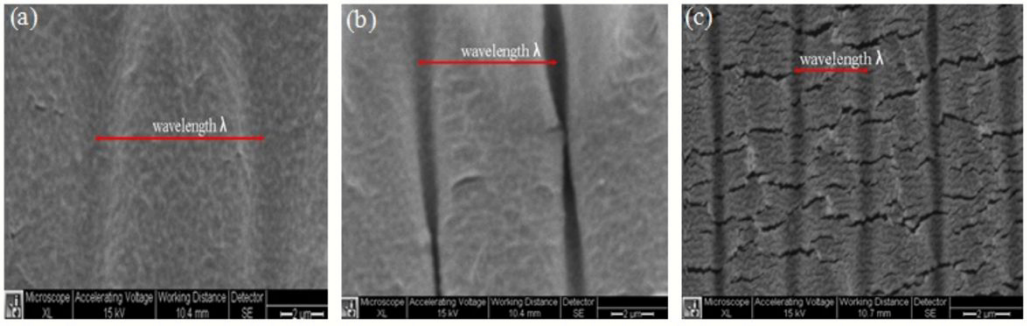

Figure 3.3: Micro-wrinkle profiles for different pre-strain values of (a) 18%, (b)36%, and (c)70%.

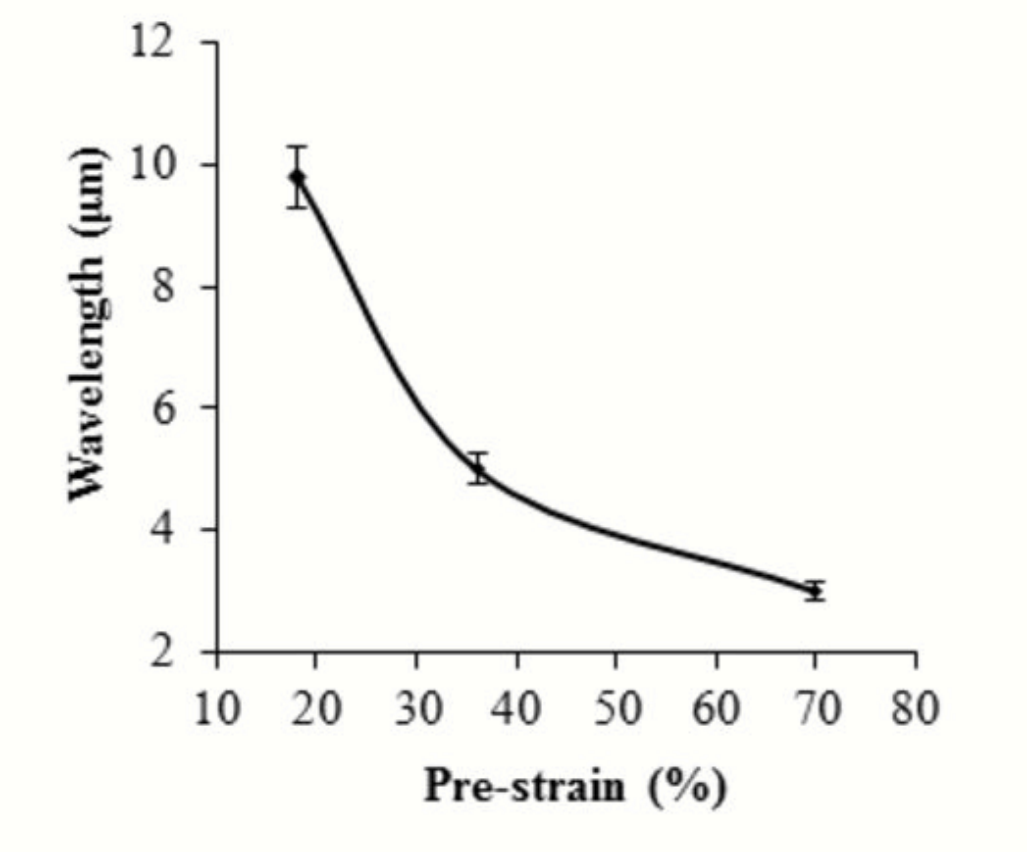

Figure 3.4: The wavelength of the profile versus pre-strain value of the PDMS substrate.

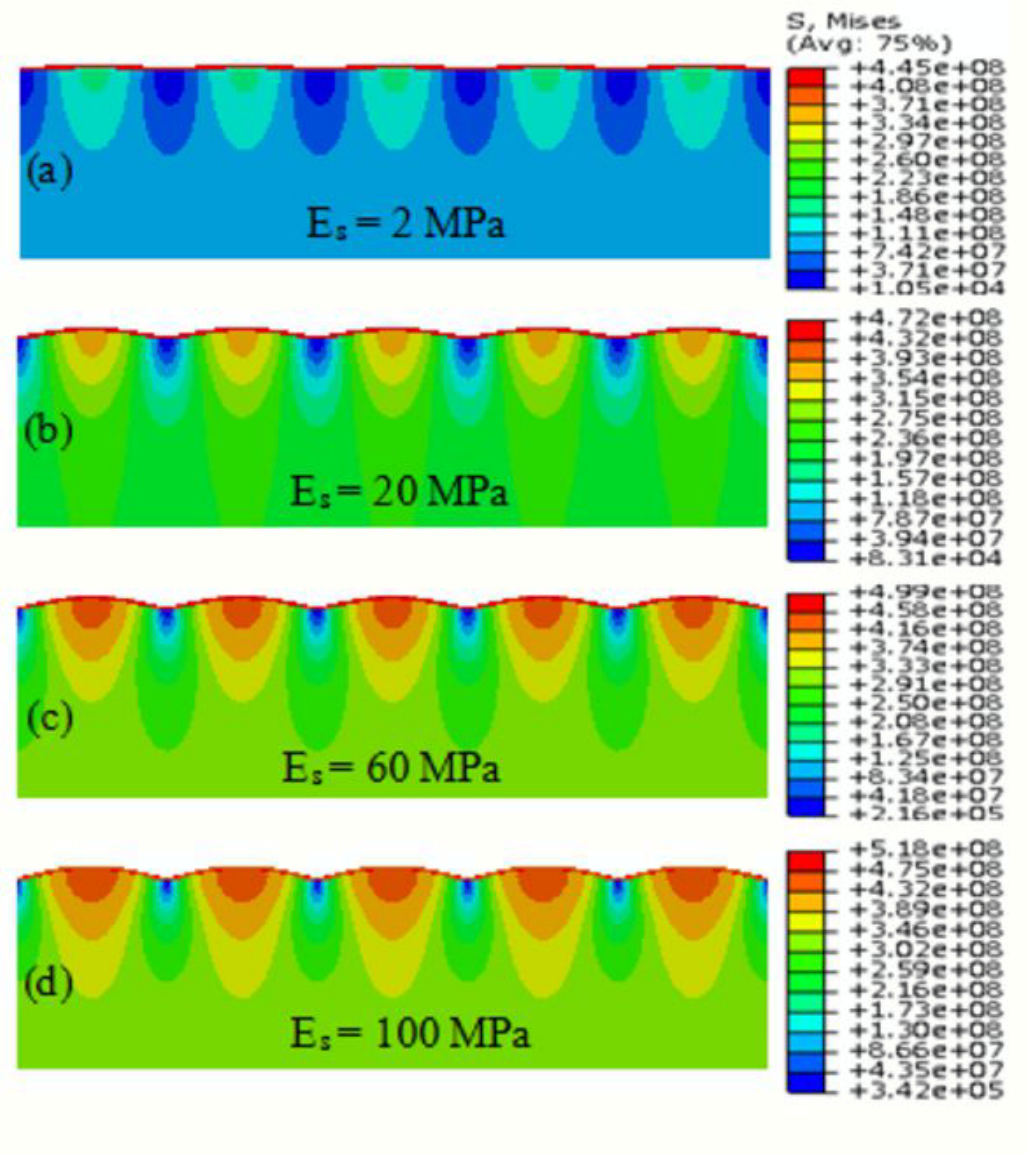

Figure 3.5: Von Mises showing the dependence of elastic modulus of the substrate on wrinkle profile of Au film on PDMS substrate at 36% pre-strain.

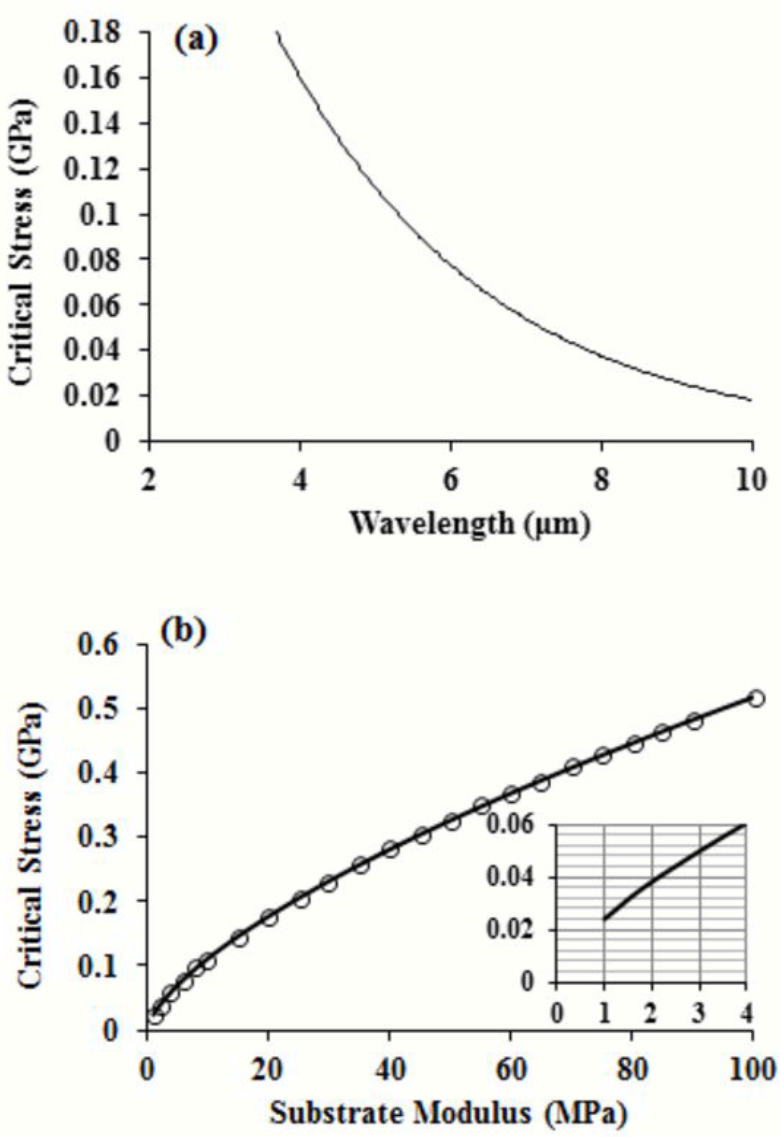

Figure 3.6: Dependence of (a) profile wavelength on critical stress and (b) substrate modulus on critical stress.

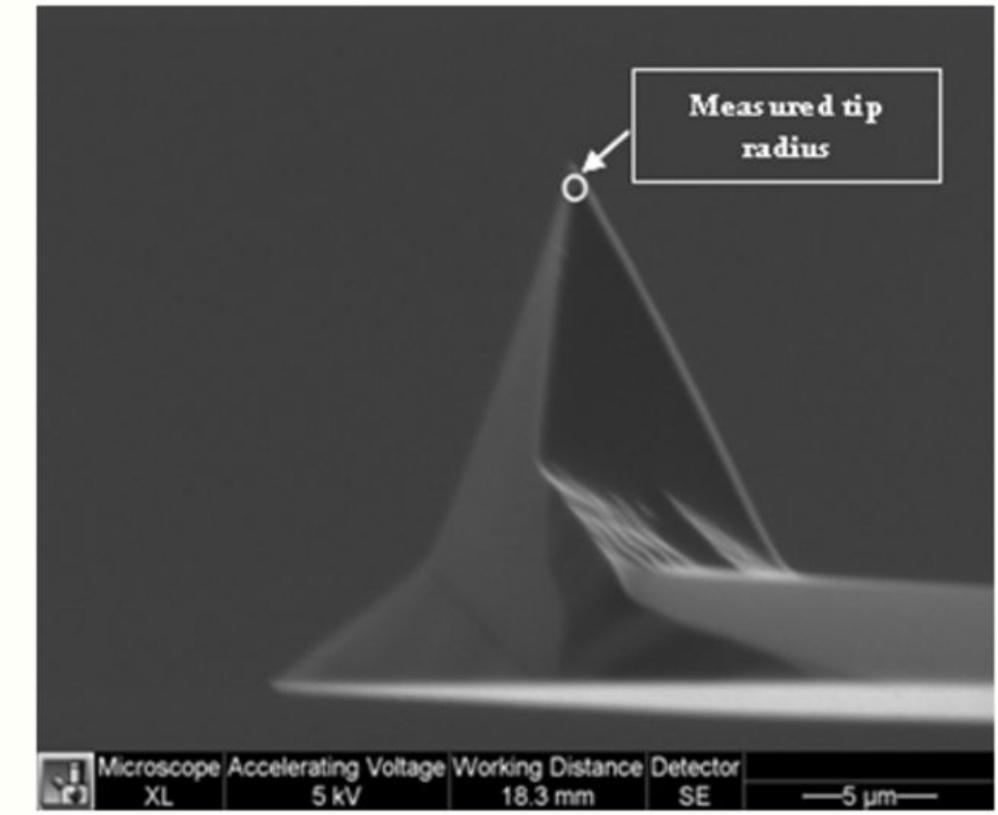

Figure 3.7: SEM image of AFM tip profile.

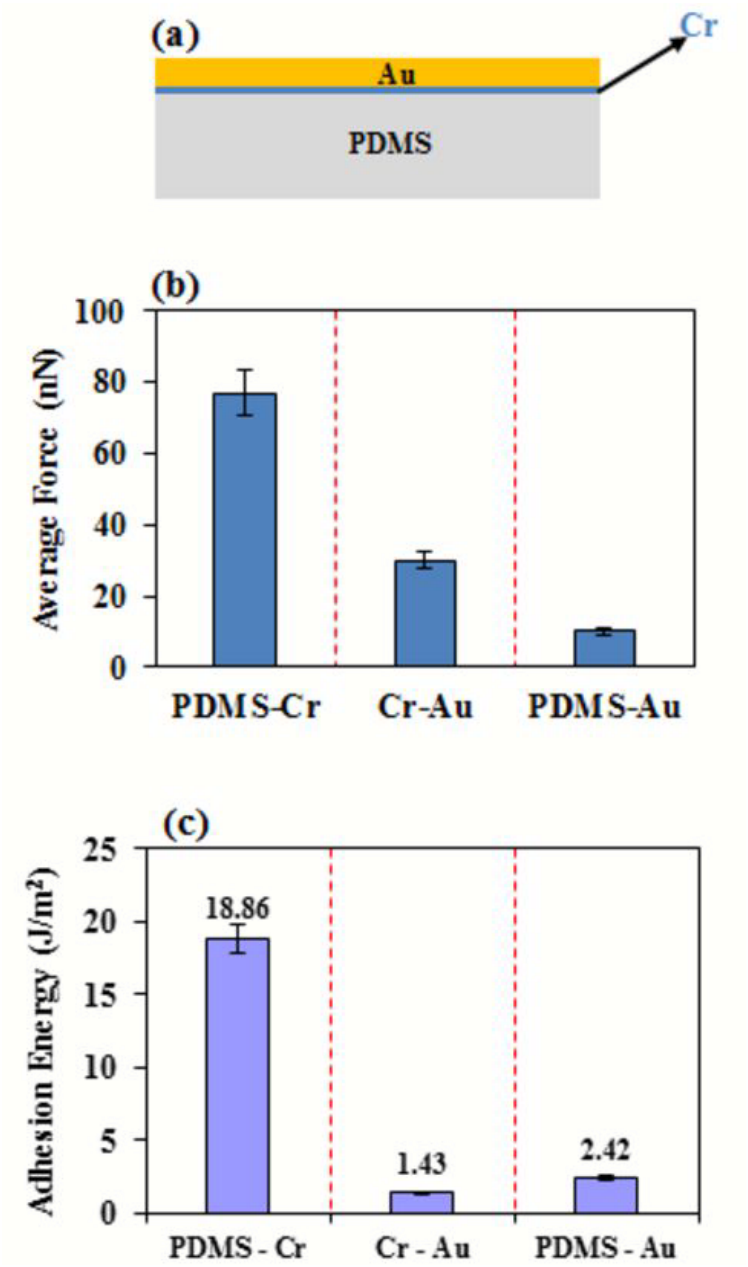

Figure 3.8: Interfacial adhesion in Au-coated PDMS structure: (a) schematic of Au-coated PDMS structure with Cr interlayer, (b) average of the measured AFM adhesion forces, and (c) measured AFM adhesion energies.

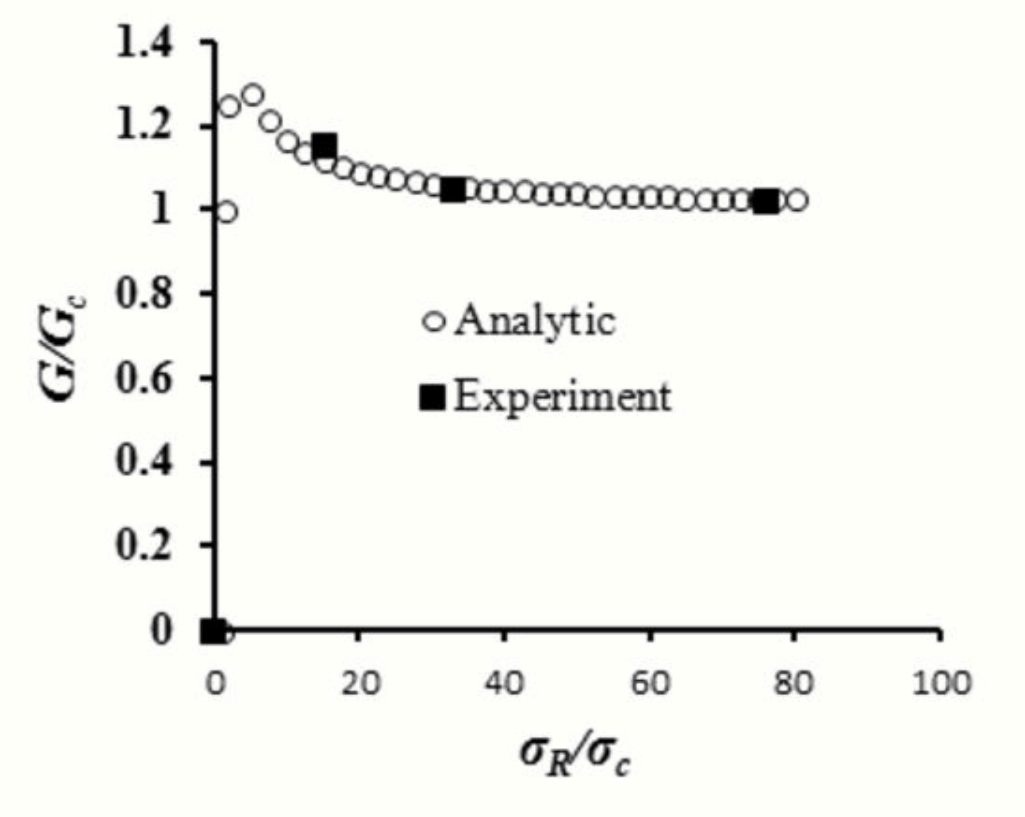

Figure 3.9: Plot of $G = G_c$ versus σ_R/σ_c.

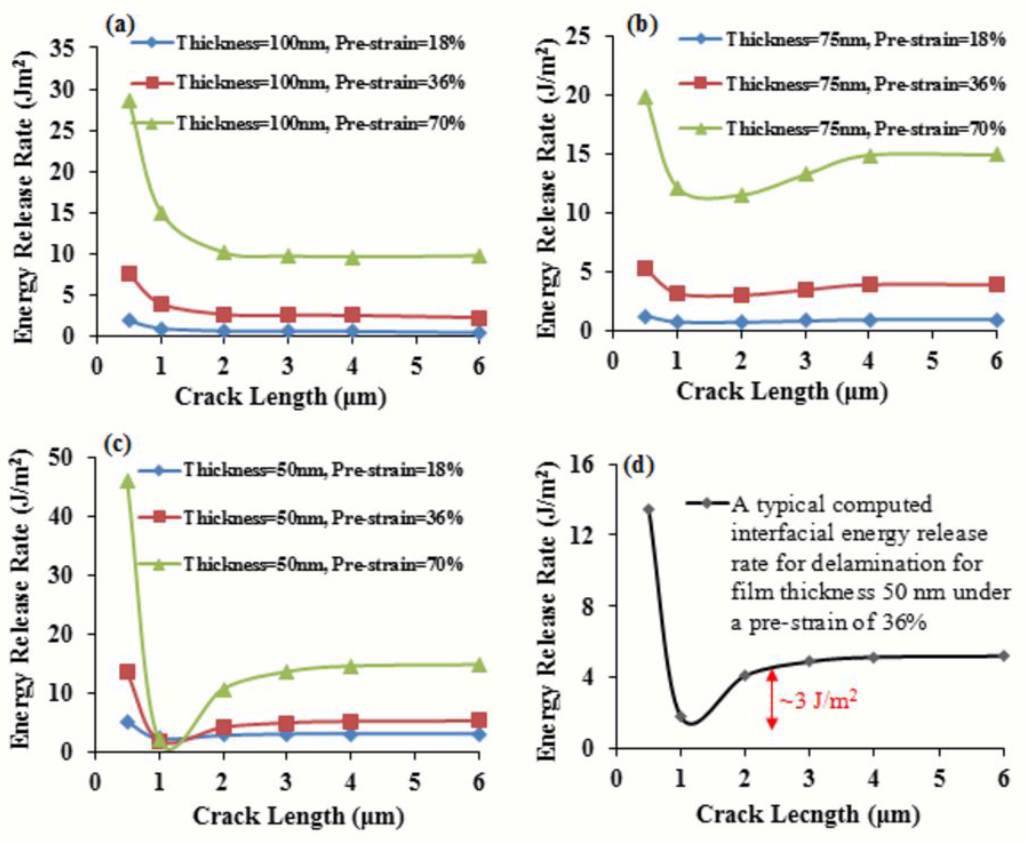

Figure 3.10: Interfacial energy release rate (G_{comp}) versus interfacial crack length. (a) 100 nm thick Au films on PDMS substrates; (b) 75 nm thick Au films on PDMS substrates; (c) 50 nm thick films on PDMS substrates; and (d) 50 nm thick film with 36% pre-strain and delamination.

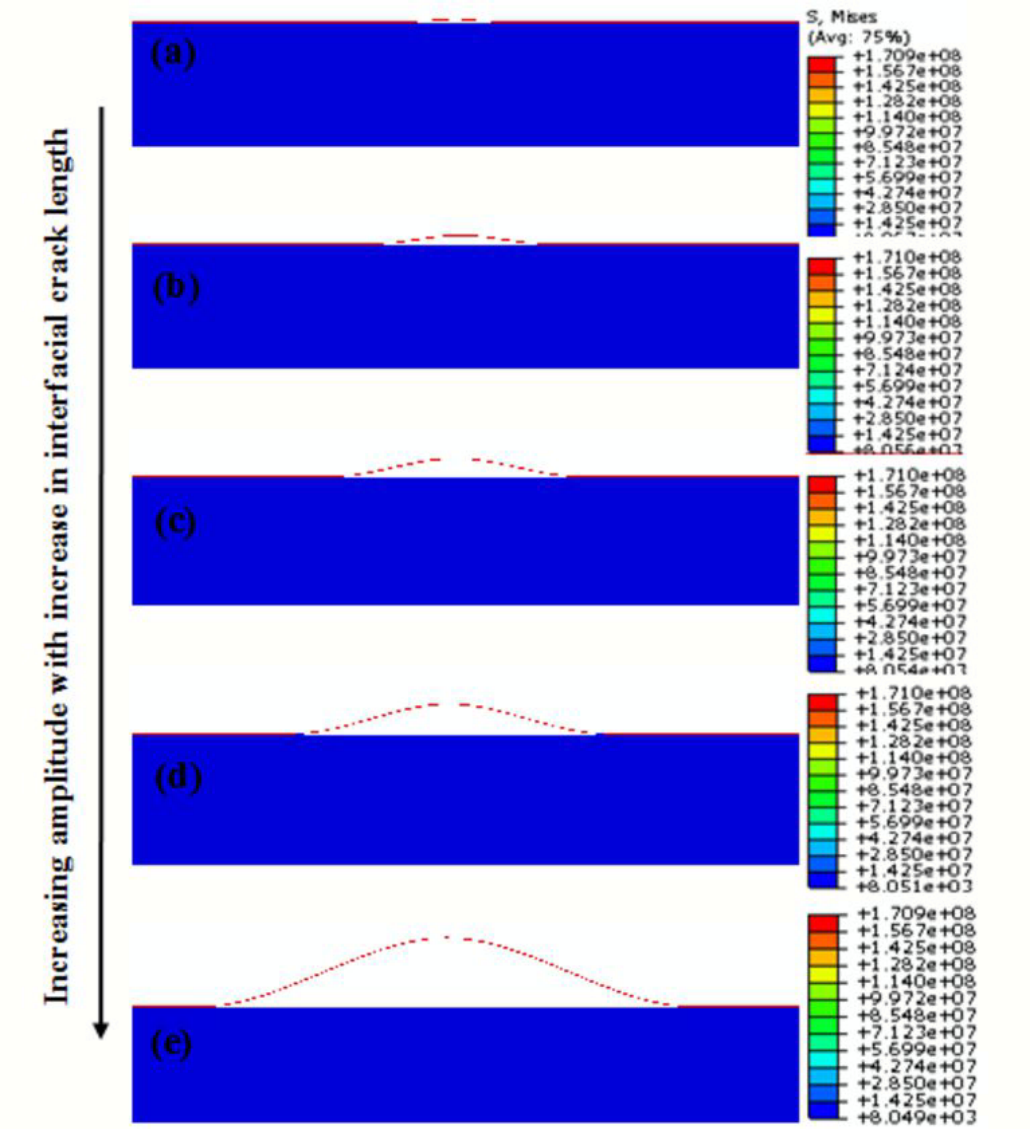

Figure 3.11: Von Mises of delamination-induced buckled Au film. (a)−(e) The amplitude increases with increasing interfacial crack length.

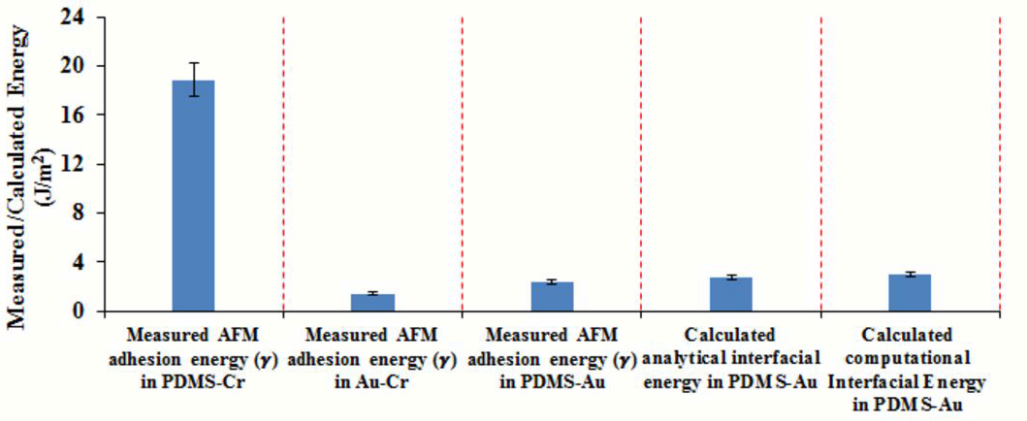

Figure 3.12: Comparison of measured AFM adhesion energies and calculated interfacial energy release rates.

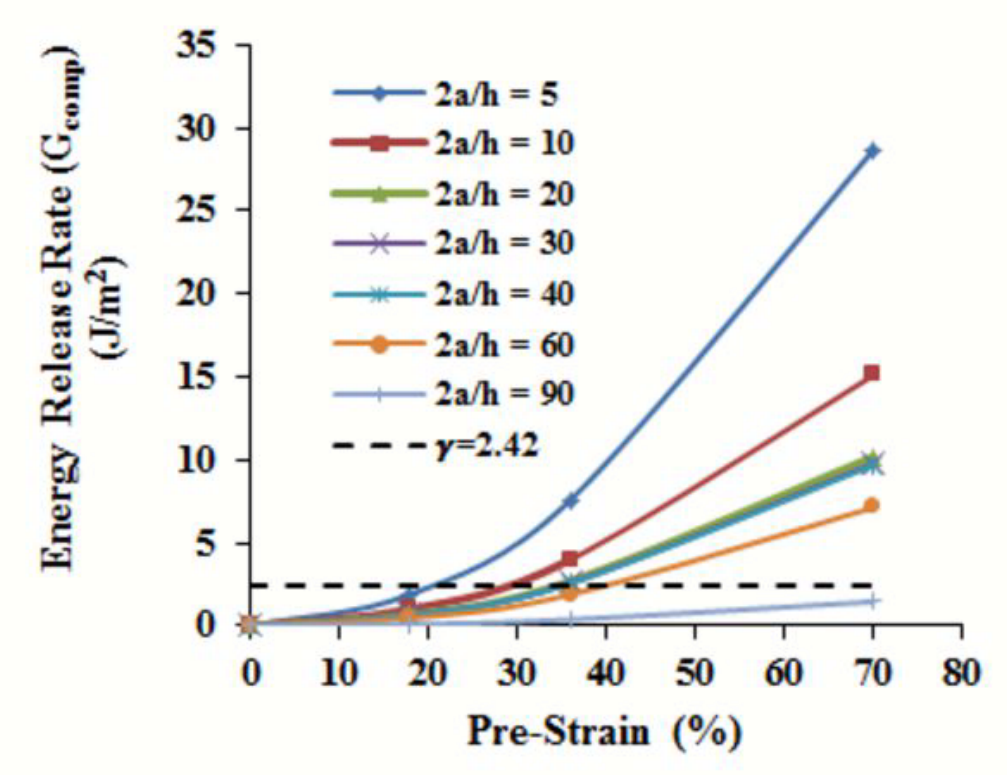

Figure 3.13: Interfacial energy release rate (G_{comp}) versus pre−strain.

Chapter 4

Adhesion in Flexible Organic and Composite Organic/Inorganic SCs and LEDs

This chapter presents the results of an experimental study of the adhesion between bi-material pairs that are relevant to organic light emitting devices, composite organic/inorganic light emitting devices, organic bulk heterojunction solar cells and composite organic/inorganic solar cells on flexible substrates. Adhesion between the possible bi-material pairs is measured using force microscopy techniques. These include: interfaces that are relevant to organic light emitting devices, composite organic/inorganic light emitting devices, bulk heterojunction solar cells and composite combinations of titanium dioxide (TiO_2) and poly(3-hexylthiophene) (P3HT).

Two important contributions were made in this work. Firstly, we studied adhesion between bi-material pairs in the flexible organic and composite organic/inorganic solar cells and light emitting devices. We measured and ranked the adhesion forces and energies between different layers in the flexible organic and composite organic/inorganic light emitting devices and solar cells via the AFM technique. Secondly, our experimental results lead to the following important conclusions:

- The blended active layer of MEH:PPV:TiO_2 in the composite organic/inorganic light emitting device adheres better to the adjacent Al and PEDOT:PSS layers than the active layer consisting of MEH:PPV.

- The incorporation of TiO_2 nanoparticles into the active layers of bulk heterojunction (P3HT:PCBM) organic solar cells reduces the adhesion to the adjacent hole transport and cathode layers.

- The improvements in charge transport facilitated by TiO_2 must, therefore, be balanced against potential reductions in the adhesion that might occur as a result of the incorporation of TiO2 nanoparticles into the active layers of bulk heterojunction solar cells.

These experimental results also facilitate the design of robust flexible organic and composite organic/ inorganic light emitting devices and solar cells.

4.1 Introduction

In the recent years, there has been increasing interest in the development of organic light emitting devices with lower power consumption and higher resolution than traditional displays [29]. Bulk heterojunction solar cells with active layers consisting of poly(3-hexylthiophene) (P3HT) and phenyl-C61-butyric acid methylester (PCBM) have also been engineered to have efficiencies of $\sim 10\%$ [36]. However, one of the major challenges is the design of improved charge transport. This is because of the tendency for charge recombination to occur before the charges reach the electrodes. The challenges are further exacerbated by the imperfect adhesion and contact at the interfaces between the layers that are relevant to organic electronics structures [40, 56, 74].

There is, therefore, a need to engineer new ways of improving charge mobility and adhesion/contact within/between the layers that are relevant to organic solar cells and organic light emitting devices. There is also a potential for improving charge transport via incorporation of nanoscale titanium dioxide (TiO_2) particles into the active layers of organic solar cells and light emitting devices [83]. In the case organic solar cells, the results show that, in selected cases, the device performance may be improved, depending on the morphology and sizes of the nanoscale TiO_2 particles.

McGehee *et al.* [79] explored the fabrication of highly efficient composite solar cells with improved exciton and charge conduction in the ordered bulk heterojunction solar cells. Kuo *et al.* [62] have developed fabrication processes for the processing of composite organic/inorganic solar cells with well aligned TiO_2 nanorods in P3HT matrix layers. These were shown to have higher efficiencies than bilayer

TiO_2 film/P3HT cells. Her *et al.* [37] have also processed composite photovoltaic cells with well-ordered nanoporous TiO_2 /P3HT structures. These composite cells had higher efficiencies than traditional thin film TiO_2. Similarly, Yodyingyong *et al.* [117] demonstrated higher efficiencies in composite solar cells with active layers containing P3HT/PCBM mixtures and highly oriented TiO_2 nanotubes with smaller diameters and larger surface areas. Kwong *et al.* [63] have also studied the influence of TiO_2 volume fraction on (P3HT):TiO_2 nanocomposite solar cells. The device performance was found to be optimum for TiO_2 volume fractions of 50% and 60%.

Due to the attractive characteristics of the stretchable electronics, considerable efforts have been made to design and fabricate stretchable electronic devices [17, 68, 76]. Intrinsically stretchable polymer light emitting devices have been fabricated using carbon nanotube-polymer composite electrodes [122]. These are metal-free and can be linearly stretched to strains of up to 45% [122]. Stretchable organic solar cells have also been fabricated on a pre-stretched substrate [75, 96, 122]. These were observed to have similar photovoltaic characteristics in the unstretched and stretched conditions [76, 122]. Polymer-based photovoltaic devices on plastic foil substrates with thicknesses less than $2\mu m$ have also been shown to have equal power conversion efficiencies to those on rigid glass substrates. These can also withstand mechanical deformation. The mechanics of failure and the stretchability and ductility of metal films on elastomer substrates have also been studied by Li *et al.* [70, 71] and Xiang *et al.* [115], while Li *et al.* and Suo *et al.* [72] have investigated the adhesion between elastomer substrates and metal films.

In an effort to understand cohesion and reliability of organic solar cells, Brand *et al.* [8] have characterized the adhesive and cohesive properties of the materials and interfaces present in the layered structures of organic bulk heterojunction photovoltaic devices. They showed that adhesion and cohesion in these structures are affected by phase-separation, surface morphology, and electrochemical reactions. Dupont *et al.* [22, 23] have also improved the interfacial adhesion in bulk heterojunction solar cells by increasing the post deposition annealing temperature and time. Prior work by Bruner *et al.* [10] has recently shown that the cohesive properties of layers in buck heterojunction solar cells increase with increasing thickness. However, a steady decrease in power conversion efficiency was also observed with increasing thickness.

Earlier work by Tong *et al.* [106] has also studied the adhesion between layers that are relevant to organic solar cells and light emitting devices on rigid glass substrates. However, there have been only limited studies of adhesion on composite organic/inorganic light emitting devices and solar cells on flexible substrates [107]. In this chapter, we present the results of an experimental study of adhesion between bi-material pairs that are relevant to organic and composite organic/inorganic light emitting devices and solar cells on flexible substrates. Atomic force microscopy (AFM) is used to measure the adhesion between the possible bi-material pairs that are relevant to organic and composite organic/inorganic light emitting devices and solar cells. The origins of the adhesion are then explored before discussing the implications of the results for the design of robust organic and composite organic/ inorganic light emitting devices and solar cells.

4.2 Expermental Procedures

4.2.1 Material Processing

The layered structures of the flexible organic and composite organic/inorganic light emitting devices are presented in Figures 4.1(a) and 4.1(b). The flexible organic light emitting device has the PDMS/Cr/PEDOT:PSS/MEH:PPV/Al structure, while the flexible composite organic/inorganic light emitting device has the PDMS/Cr/PEDOT:PSS/MEH:PPV:TiO_2/Al structure. The layered structures of the flexible organic and composite organic/inorganic solar cells are presented in Figures 4.1(c) and 4.1(d). The flexible organic solar cell has the PDMS/ Cr/PEDOT:PSS/P3HT:PCBM/Al structure. However, in the flexible composite solar cell, the active layer of P3HT:PCBM blend was replaced with P3HT:TiO_2 or a mixture of P3HT:PCBM:TiO_2, with the other layers being the same as those in the flexible organic solar cell.

4.2.1.1 Processing of The Flexible Organic and Composite Organic/Inorganic Light Emitting Devices

In the case of the flexible OLED, the PDMS substrate was prepared by first mixing a Slygard 184 silicone elastomer curing agent with a Slygard 184 silicone elastomer base (Dow Corning Corporation, Midland MI), with a 1:10 weight ratio. The mixture was then processed under a vacuum pressure of 6 kPa for 30 minutes. This was done to remove internal bubbles from the PDMS. This mixture was spin cast onto glass

for 60 seconds. This was done at 400 revolutions per minute (rpm). The mixture was then cured for 2 hours at 80 ℃.

The chromium (Cr) adhesive layer of 5 nm was deposited on top of the PDMS-coated glass using an electronbeam evaporator (Denton DV 502 A, Denton Vacuum, Moorestown, NJ). Baytron P VP Al-4083 PEDOT:PSS (now Heraeus Clevios, Hanau, Germany) was filtered through a 0.2 μm filter to further improve uniformity and smoothness. The filtered mixture was spin-coated at 3000 rpm for 1 minute. It was then cured at 120 ℃ for 5 minutes to remove moisture from the mixture.

The poly[2-methoxy-5 -(20-ethyl-hexyloxy)1,4-phenylene vinylene] (MEH:PPV) (Sigma Aldrich, St. Louis, MO) was mixed with chloroform at a $5g/L$ ratio. The mixture was stirred continuously for 6 h at room-temperature. It was then passed through a $0.45\mu m$ teflon filter, prior to spin-coating at 1000 rpm for 1 minute. Finally, a 100 nm thick aluminum (Al) cathode layer was thermally evaporated onto the MEH:PPV active layer using an Edwards E306A deposition system (Edwards, Sussex, UK).

In the case of the flexible composite light emitting devices, the active layer was prepared differently, with other layers being the same as the ones in the flexible organic light emitting device. The TiO_2 nanoparticles were added into the MEH:PPV single polymer blend to form MEH:PPV:TiO_2 mixtures/composites. Subsequently, 15 mg of MEH:PPV (in 2ml of chloroform) was mixed at room-temperature for 6 hours. Consequently, 5 mg of TiO_2 was sonicated in $2ml$ of chloroform for 45 minutes. The resulting two mixtures were then mixed and sonicated for 30 minutes.

4.2.1.2 Processing of Flexible Organic and Composite Organic/ Inorganic Solar Cells

In the case of the flexible organic solar cells, the PDMS substrate and Cr layer were prepared using procedures described previously in Section 4.2.1. Baytron P PEDOT:PSS obtained from H. C. Starck (now Heraeus Clevios, Hanau, Germany) was used for the electron-hole pair separation. It served as the hole extraction layer. The PEDOT:PSS solution was filtered through a 0.2 lm filter. It was then spin-coated onto the PEDOT:PSS layer for 1 minute at 3000 rpm. It was cured for 5 minutes at 120 ℃. The bulk heterojunction active layer consisted of a mixture of poly(3-hexylthiophene) (Sigma Aldrich, St. Louis, MO) and phenyl-C61-butyric acid methyl ester (Sigma Aldrich, St. Louis, MO). It was mixed with chloroform in the ratio of 1:0.8. This mixture was spin cast onto the PEDOT:PSS at 1500 rpm for 1 minute. It was then cured for 10 minutes at 150 ℃. Finally, the aluminum (Al) cathode layer was thermally evaporated onto the P3HT:PCBM active layer using an Edwards E306A deposition system (Edwards, Sussex, UK).

In the case of the flexible composite solar cells, the active layer was prepared differently, with other layers being prepared with the same protocols as the flexible organic solar cell. The active layer of the P3HT:TiO_2 or the P3HT:PCBM:TiO_2 blend was prepared as follows. For the P3HT:TiO_2 blend, the PCBM was replaced entirely with TiO_2(Sigma Aldrich, St. Louis, MO). The best weight ratio of P3HT:TiO_2 blend was found to be $1 : 2.3$ [63]. In the case of P3HT:PCBM:TiO_2 blend, the weight ratio was chosen to be $1 : 0.4 : 0.4$. This ratio replaced half the PCBM with TiO_2. The TiO_2 nanoparticles were dissolved in chlorobenzene and sonicated

for at least 30 minutes to form a uniform solution. The TiO_2 solution was then mixed with P3HT or P3HT:PCBM solution and placed in an ultrasonic bath for an additional 30 minutes. The blend was then spin coated for 60 seconds at 150 rpm, before annealing for 10 minutes at 150 ℃.

4.2.2 AFM Adhesion Experiments

Etched silicon contact mode AFM tips were purchased from Veeco Instruments (now Bruker Instruments) Woodbury, NY. The PDMS substrates were coated with Cr, while the AFM tips were coated separately with Cr and Al, using an Edwards E306A evaporation system (Edwards, Sussex, UK). The PDMS substrates were coated with Cr to improve their adhesion to PDMS substrates. PEDOT:PSS solution was then spin-coated onto Cr-coated PDMS substrates. AFM tips were dip-coated with organic (P3HT:PCBM, MEH:PPV and P3HT) and organic/inorganic (P3HT:PCBM:TiO_2, MEH:PPV:TiO_2, P3HT:TiO_2, and TiO_2) active materials. To measure the adhesion forces between the active materials and Al, both organic and composite organic/inorganic active materials were spin-coated onto glass substrates. PCBM was also spin-coated onto glass in the order to measure the adhesion between P3HT (coated on the AFM tip) and PCBM (coated on glass).

The AFM measurements were performed in air of a temperature range of $22 \sim 25$ ℃ and a relative humidity range of $31\% \sim 46\%$. A schematic of the interaction between the substrate (material 1) and the tip of AFM (material 2) is presented in Figure 4.2. About ten force-displacement curves were obtained for each interaction. The force-displacement measurements were obtained using a Digital Instruments

Dimension 3000 AFM (Digital Instruments, Plainview, NY). The spring constant of each tip was measured using the thermal tune method [49]. The measurements were performed in a Digital Instruments Nanoscope IIIa atomic force microscope (Digital Instruments, Plainview, NY). The measurements of the tip deflections and the spring constants were then substituted into Eq. (2.1) to determine the adhesion forces.

Due to the high sensitivity of AFM measurements to surface roughness, the substrate roughnesses and the tip radii were measured for each of the interaction pairs. The surface roughnesses were obtained using tapping mode AFM. About 10 height and phase images of each substrate were obtained. These were used to measure the root mean squared roughnesses in areas ranging from 1×1 to 10×10 μm^2. The AFM tips were examined in a Scanning Electron Microscope (SEM) that was instrumented with an Energy Dispersive X-ray Spectroscopy (EDS) system (Philips FEI XL30 FEGSEM, Hillsboro, OR). This was done before and after the AFM adhesion measurements. The tip radii were calculated from tip images obtained from SEM (Figure 4.3). The measurements of the surface roughness and the tip radii were then used to estimate the effective tip radii and the adhesion energies from Eqs. (2.3) and (2.2), respectively. The SEM/EDS images of the AFM tips (before and after measurements) were also used to check for any changes in the morphology and atomic number contrast (composition differences) of the AFM tips after the AFM adhesion measurements. In this way, the SEM images of the AFM tips were used to check for possible occurrences of cohesive and adhesive failure.

4.3 Results and Discussion

4.3.1 Surface Characterization

4.3.1.1 Surface Morphologies and Roughness Measurements

The root mean squared (rms) surface roughnesses of the different layers in the organic light emitting device that were examined in this are presented in Figure 4.4. The average rms roughness values obtained for the different layers are presented in Table 4.1. The layers in the flexible light emitting device had low surface roughnesses that ranged from 0.6 nm to 2.4 nm, while the Cr layer had a higher roughness value of $9.9 \pm 2.2\ nm$. It is important to note that the surface roughness values obtained for PDMS spun on glass was very low (below 1 nm). This is expected from a conformal, elastomeric polymer surface. The average tip radius of the coated tip was about 170 nm. Since the surface roughnesses were much smaller than the tip radii, it can be concluded from Eqs. (2.2) and (2.3) that the surface roughnesses dominated the adhesion energy calculations.

Table 4.1: Average rms roughness values for layers in the flexible light emitting device.

Surface layer	**Roughness (nm)**
PDMS on glass	0.6 ± 0.1
Cr	9.9 ± 2.2
PEDOT:PSS	0.6 ± 0.1
MEH:PPV	2.2 ± 0.7
Al	2.4 ± 0.4

The different materials in the layers of the flexible solar cells exhibited different surface morphologies, as shown in Figure 4.5. The average rms roughness values

obtained for the different layers are present in Table 4.2. The layers in the flexible solar cell had low rms surface roughness values, ranging from 0.6 nm to 2.4 nm, while the Cr layer had higher rms roughness values of $9.9 \pm 2.2\ nm$. The average tip radius of the coated tip was about 180 nm. Since the surface roughnesses were much smaller than the tip radii, it can be concluded that the surface roughnesses dominated the adhesion energy calculations. In the SEM/EDS images of the tips, no significant changes were observed. Furthermore, the highest magnification SEM images did not reveal any evidence of cohesive failure. Hence, we conclude that the measured AFM pull-off forces correspond to adhesive failures.

Table 4.2: Average rms roughness values for layers in the flexible solar cells.

Surface layer	**Roughness (nm)**
PDMS on glass	0.6 ± 0.1
Cr	9.9 ± 2.2
PEDOT:PSS	0.8 ± 0.1
P3HT:PCBM	0.7 ± 0.1
Al	2.4 ± 0.4

4.3.2 Adhesion of Flexible Organic and Composite Organic/ Inorganic Light Emitting Devices (LEDs)

4.3.2.1 Adhesion Forces

The adhesion forces obtained for the bi-material pairs in the model flexible organic and composite light emitting device are summarized in Figure 4.6. These show that the adhesion force between PEDOT:PSS and MEH:PPV:TiO_2 had the highest value of 82 nN. The Cr layer also adhered well to the PDMS layer and also to the

PEDOT:PSS layer. The adhesion force between PEDOT:PSS and MEH:PPV was found to be 59 nN, while the adhesion force between the MEH:PPV and the Al layer was $\sim$ 10 nN. The addition of TiO_2 nanoparticles to the MEH:PPV increased the adhesion force between PEDOT:PSS and MEH:PPV:TiO_2. The adhesion force between the MEH:PPV:TiO_2 and Al layer was ~ 31 nN.

4.3.2.2 Adhesion Energies

The non-dimensional parameter for the calculation of the adhesion energy was found by performing the iterative calculations to be $\sim 10^{-8}$. Since this is $\ll 0.1$ [106, 107], the DMT model applies. By taking into account of the surface roughness and the AFM tip radius, the adhesion energy can be obtained from Eqs. (2.2) and (2.3). This DMT model had been used in this way for interfacial fracture toughness calculations [81, 89, 106, 107] in different multilayered structures. The adhesion energy results obtained for the bi-material pairs in flexible organic and composite light emitting devices are summarized in Figure 4.7. The results show that the Cr layer adhered strongly to the PDMS substrate, with a high adhesion energy of 18.9 J/m^2. The adhesion energy between PEDOT:PSS and MEH:PPV was 15 J/m^2. After adding TiO_2 nanoparticles to the MEH:PPV single polymer blend, the adhesion energy between PEDOT:PSS and MEH:PPV:TiO_2 had a higher value of 20.8 J/m^2.

It is important to note here that the increase in the adhesion energy of PEDOT:PSS-MEH:PPV:TiO_2 interface can be attributed to changes in surface morphology and phase separation of MEH:PPV:TiO_2, as well as electrochemical reactions between PEDOT:PSS and MEH:PPV:TiO_2 . The latter occur due to

the introduction of TiO_2 . Similar phenomena have been reported by Dauskardt and co-workers [8, 10] in research on P3HT:PCBM mixtures. Also, the adhesion energy between MEH:PPV and Al was 0.8 J/m^2. Furthermore, the addition of TiO_2 nanoparticles to the MEH:PPV single polymer blend resulting in an adhesion energy between MEH:PPV:TiO_2 and Al of 5.9 J/m^2. The composite light emitting device with the MEH:PPV:TiO_2 active layer, therefore, had higher adhesion energies at the two interfaces with its adjacent layers.

4.3.3 Adhesion of Flexible Organic and Composite Organic/ Inorganic Solar Cells(SCs)

4.3.3.1 Adhesion Forces

The adhesion forces obtained for the bi-material pairs in the model flexible organic and composite solar cell are summarized in Figure 4.8. The adhesive interactions in PEDOT:PSSP3HT: TiO_2 and PEDOT:PSS-P3HT:PCBM:TiO_2 structures are compared with those of the PEDOT:PSS-P3HT:PCBM bi-material couples. The results show that the adhesive interactions between PEDOT:PSS and P3HT:PCBM result in the highest adhesion force of $\sim$ 187 nN. The adhesive interactions between PEDOT:PSS and P3HT:TiO_2 had the second highest adhesion force values of 69 nN, while the adhesive interactions between PEDOT:PSS and P3HT:PCBM:TiO_2 resulted in the lowest adhesion forces of $\sim$ 40 nN. The adhesion force between P3HT and TiO_2 was low, with a value of $\sim$ 8 nN. The adhesive interactions between P3HT and PCBM resulted in an adhesion force of $\sim$ 23 nN. The

adhesive interactions of P3HT:TiO_2 -Al and P3HT:PCBM:TiO_2 -Al were compared with that of P3HT:PCBM-Al. The adhesion force between Al and P3HT:TiO_2 was the highest (306 nN), while that between Al and P3HT:PCBM:TiO_2 had the second highest value of 140 nN. The lowest adhesion force of $\sim 50\ nN$ occurred between Al and P3HT:PCBM.

4.3.3.2 Adhesion Energies

The non-dimensional parameter for the calculation of the adhesion energy was found by performing the iterative calculations to be $\sim 10^{-6}$ [106,107]. Since the parameter is much smaller than 0.1, the DMT model applies. By taking into account of the surface roughness and the AFM tip radius, the adhesion energies were obtained from Eqs. (2.3) and (2.2). The adhesion energy results were presented in Figure 4.9 for the possible bi-material pairs in the flexible organic and composite solar cell.

The results presented in Figure 4.9 show that the Cr layer adhered strongly to the PDMS substrate, with the high adhesion energy of 18.9 J/m^2. The P3HT:PCBM layer adhered strongly to PEDOT:PSS layer, with the highest adhesion energy value of 40.3 J/m^2. The high adhesion energy of the PEDOT:PSS-P3HT:PCBM interface may be due to the physical intermixing of P3HT and PSS. These react electrochemically to form $P3HT^+$ and PSS^-, as reported by Brand *et al.* [8]. and Huang*et al.* [42]. Also, the adhesion between PEDOT:PSS and P3HT:PCBM layer was much bigger than the adhesion energies of PEDOT:PSS-P3HT:TiO_2 and PEDOT:PSSP3HT: PCBM:TiO_2. Furthermore, the adhesion energy between

PEDOT:PSS and P3HT:TiO_2 was greater than that between PEDOT:PSS and P3HT: PCBM:TiO_2 .

It is also important to note here that the reduction in adhesion energy in PEDOT:PSS-P3HT:PCBM:TiO_2 can be attributed to possible effects of electrochemical reactions, due to introduction of TiO_2 nanoparticles. This can be as a result of secondary bonds that are formed when hydrogen atoms in P3HT:PCBM are attracted to oxygen atoms in TiO_2 during the chemical reactions.

The adhesion energy between P3HT and TiO_2 had the lowest with a value of 0.1 J/m^2. The adhesion energy between P3HT and PCBM was also small (1.3 J/m^2). This is in the range of the values reported by Brand *et al.* [8]. Furthermore, considering the adhesion energies between Al and different active layers, the adhesion energy between Al and P3HT:TiO_2 was the highest (with a value of 25.8 J/m^2). This was greater than the adhesion energies of the Al-P3HT:PCBM:TiO_2 and the Al-P3HT:PCBM structure. Hence, from the robustness point of view, the active layer of P3HT:TiO_2 blend was more robust than the active layer consisting of P3HT:PCBM:TiO_2 blends.

4.4 Summary and Concluding Remarks

In this chapter, a force microscopy technique was used to measure the adhesion between possible bi-material pairs that are relevant to flexible organic and composite organic/inorganic light emitting devices and solar cells. A summary of the salient conclusions arising from this chapter is presented below.

1. The AFM technique provides a simple method for the ranking of the adhesion forces and energies between different layers in flexible organic and composite organic/inorganic light emitting devices and solar cells. This could facilitate the future design of robust flexible organic and composite organic/ inorganic light emitting devices and solar cells.

2. In the case of the composite organic/inorganic light emitting device in which the active layer of MEH:PPV blend is replaced by MEH:PPV:TiO_2 mixture, the MEH:PPV:TiO_2 active layer had higher adhesion energies with the adjacent layers (PEDOT:PSS and Al). Therefore, from the robustness point of view, the blended active layer of MEH:PPV:TiO_2 adheres better to the adjacent Al and PEDOT:PSS layers than the active layer consisting of MEH:PPV.

3. In the case of the composite organic/inorganic solar cell in which the active layer of P3HT:PCBM blend is replaced with P3HT:TiO_2 or P3HT:PCBM:TiO_2 mixture, the P3HT:PCBM layer adhered better to the adjacent PEDOT:PSS and Al layers. However, although the incorporation of TiO_2 particles into the active layers has the potential of improving charge transport, the TiO_2 in the P3HT:TiO_2 layer reduces the adhesion to the adjacent PEDOT:PSS layer. Furthermore, the P3HT:PCBM:TiO_2 layer adheres poorly to the two adjacent layers (PEDOT:PSS and Al).

4. The incorporation of TiO_2 nanoparticles into the active layers of bulk heterojunction (P3HT:PCBM) organic solar cells reduces the adhesion to the adjacent hole transport and cathode layers. This is attributed to the potential

effects of electrochemical reactions that are associated with the introduction of TiO_2 . Hence, the improvements in charge transport facilitated by TiO_2 must, therefore, be balanced against potential reductions in the adhesion that might occur as a result of the incorporation of TiO_2 nanoparticles into the active layers of bulk heterojunction solar cells.

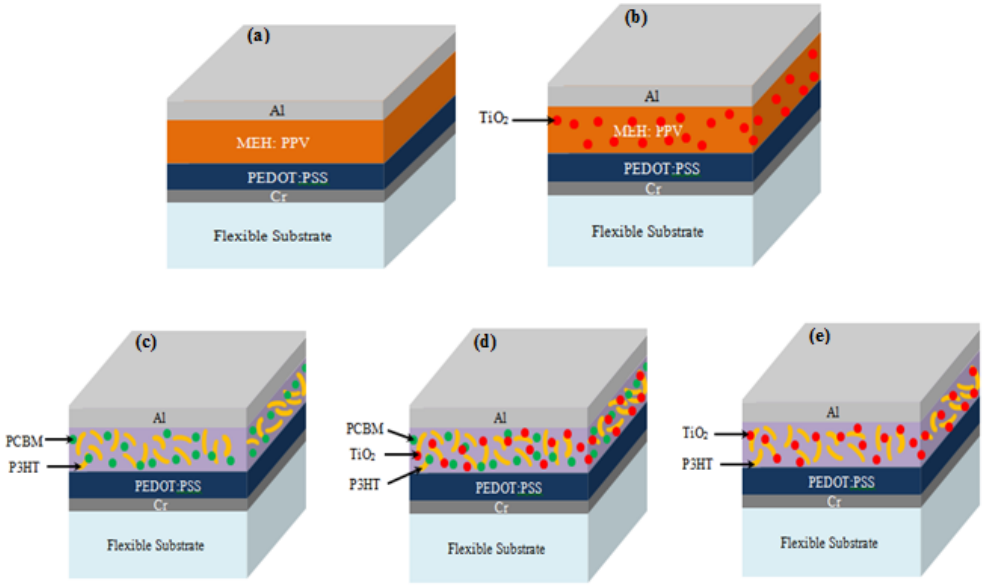

Figure 4.1: Layered structures for flexible organic and composite light emitting device and solar cells (a) flexible organic light emitting device (b) flexible composite light emitting device (c) flexible organic solar cell (d and e) flexible composite organic/inorganic solar cell.

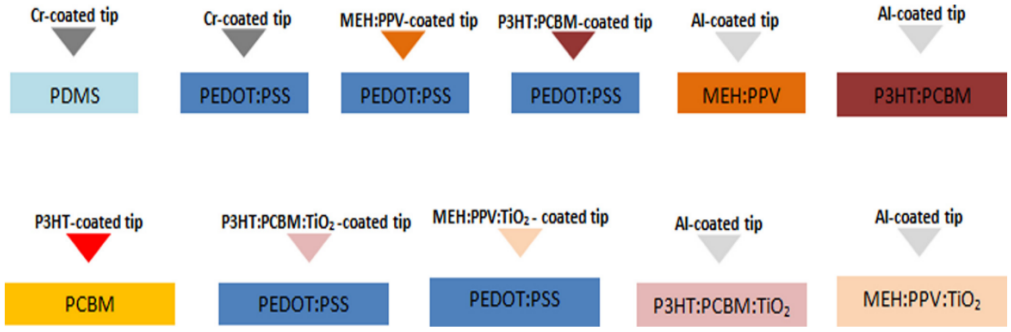

Figure 4.2: Schematic of interaction between material 1 and the tip of AFM (material 2).

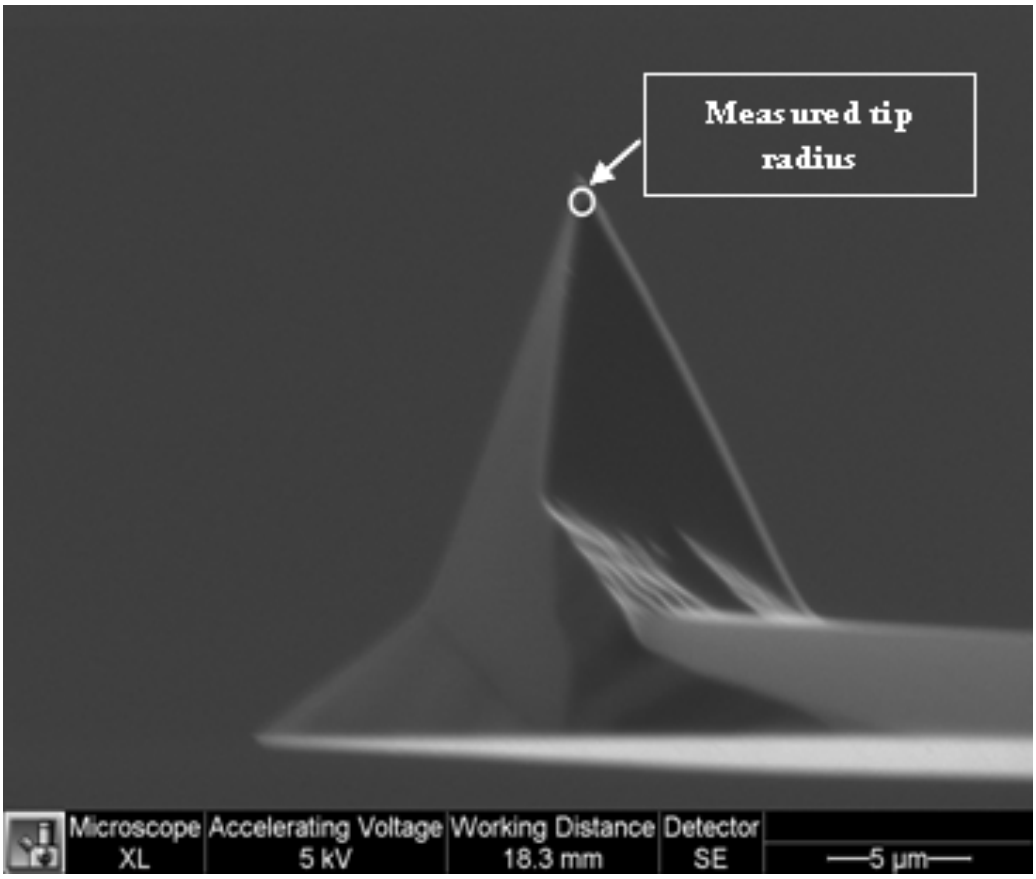

Figure 4.3: SEM image of a typical AFM tip profile.

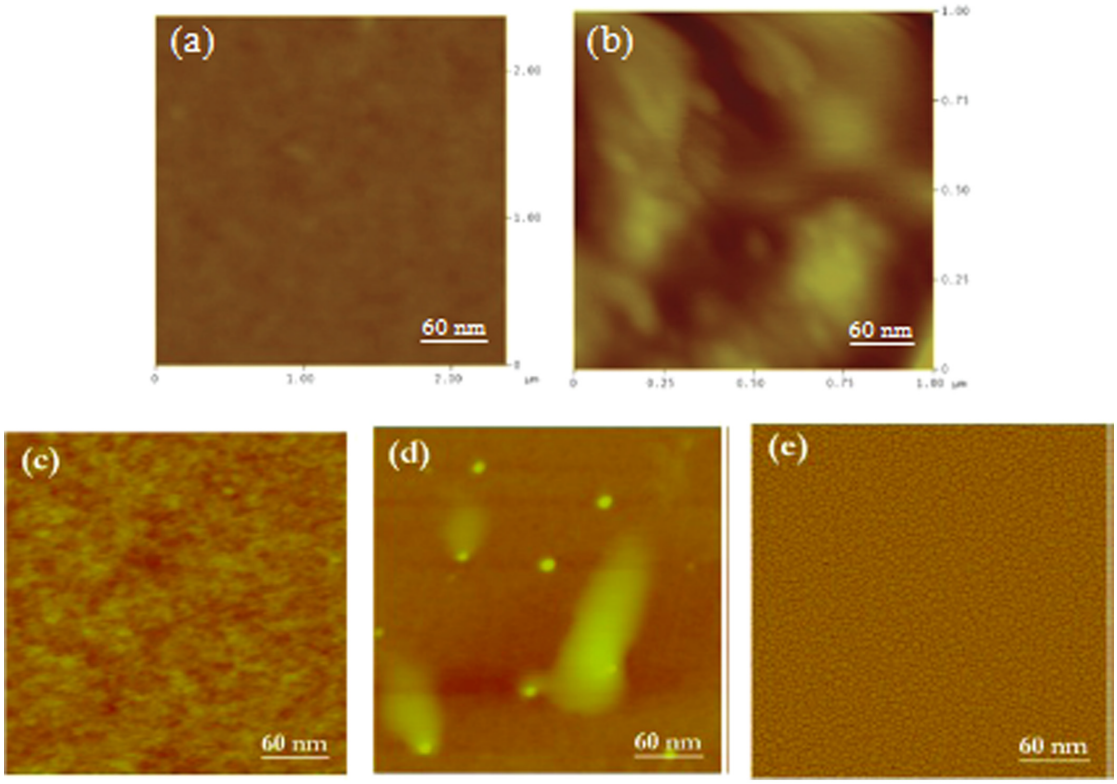

Figure 4.4: AFM surface morphologies for different layers in the flexible light emitting device: (a) PDMS (b) Cr (c) Baytron P VP AL-4083 PEDOT:PSS (d) MEH:PPV (e) Al.

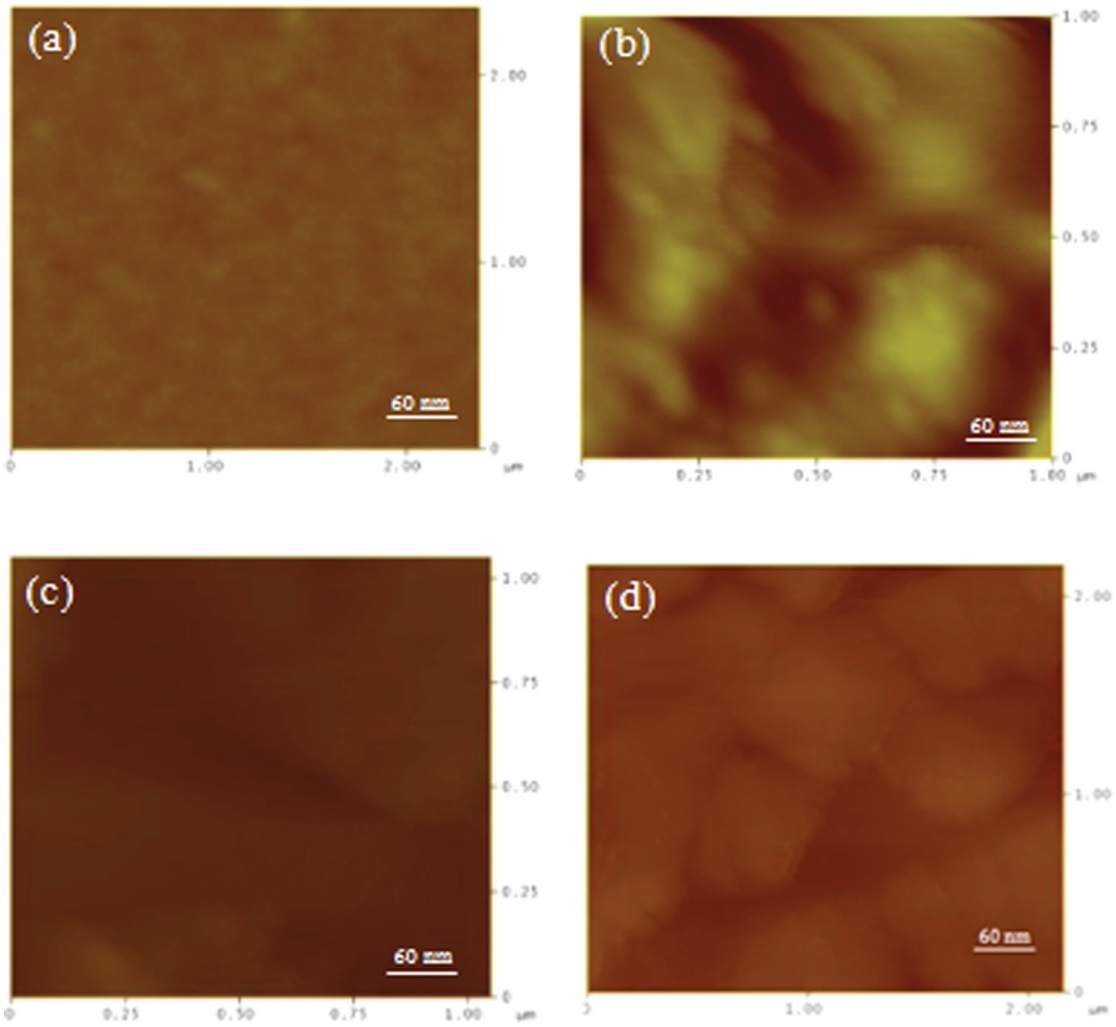

Figure 4.5: AFM surface morphologies for different layers in the flexible solar cells: (a) PDMS on glass (b) Cr (c) PEDOT:PSS (d) P3HT:PCBM.

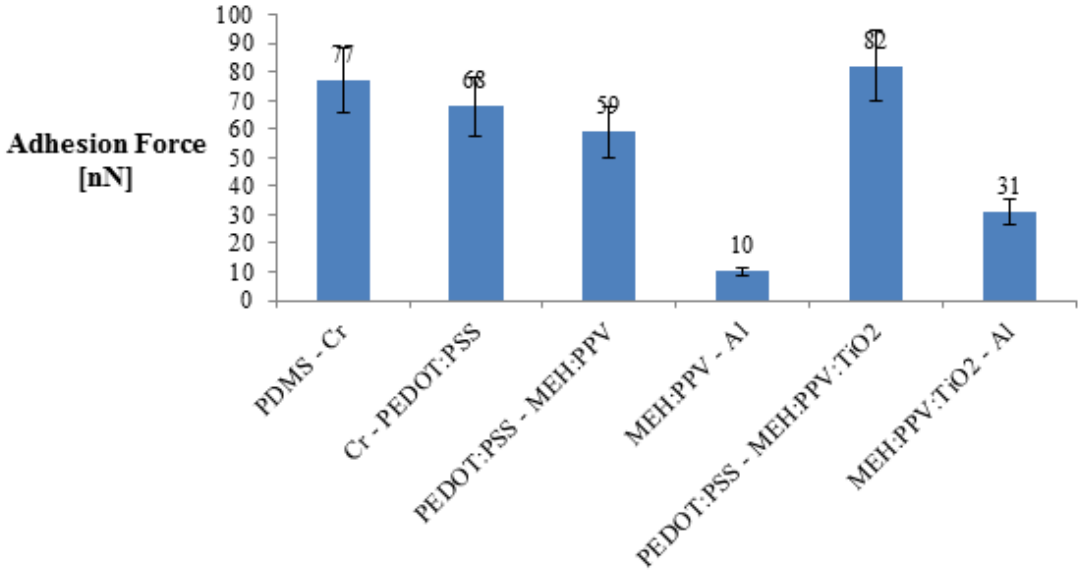

Figure 4.6: Interfacial adhesion forces in flexible organic and composite organic/ inorganic light emitting devices.

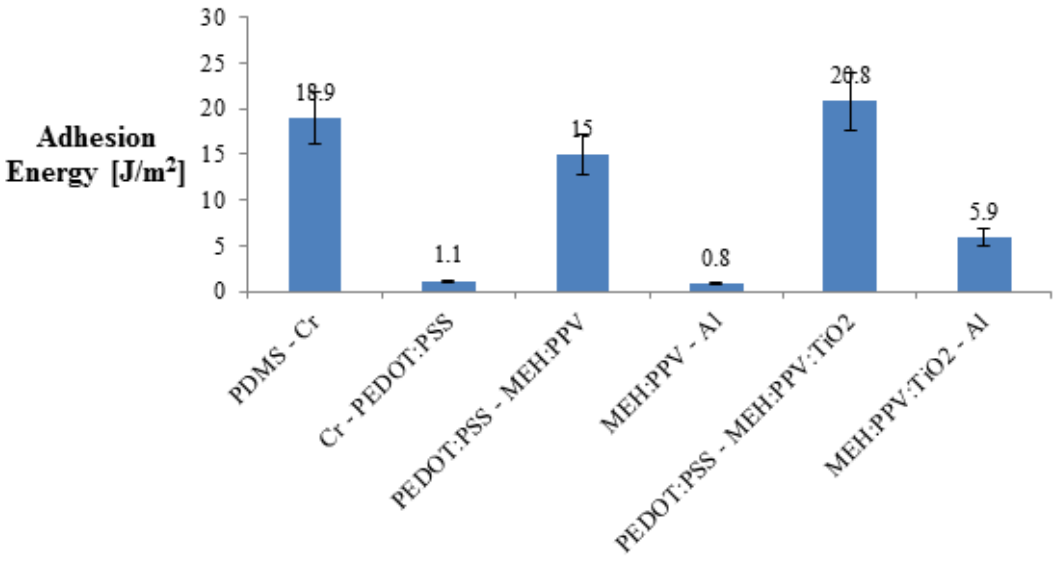

Figure 4.7: Interfacial adhesion energies in flexible organic and composite organic/ inorganic light emitting devices.

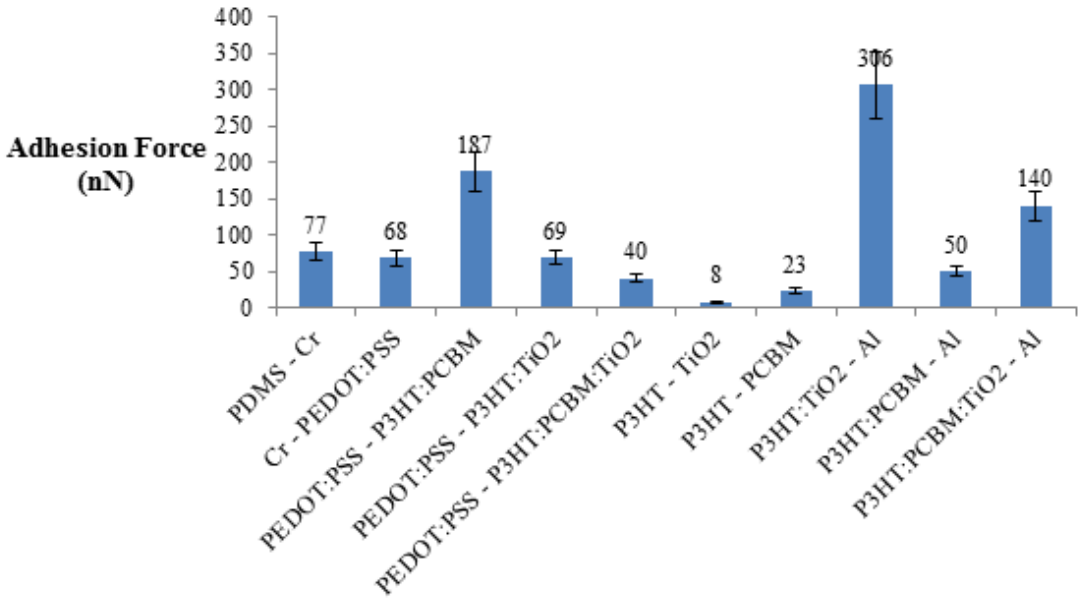

Figure 4.8: Interfacial adhesion forces in flexible organic and composite organic/ inorganic solar cell.

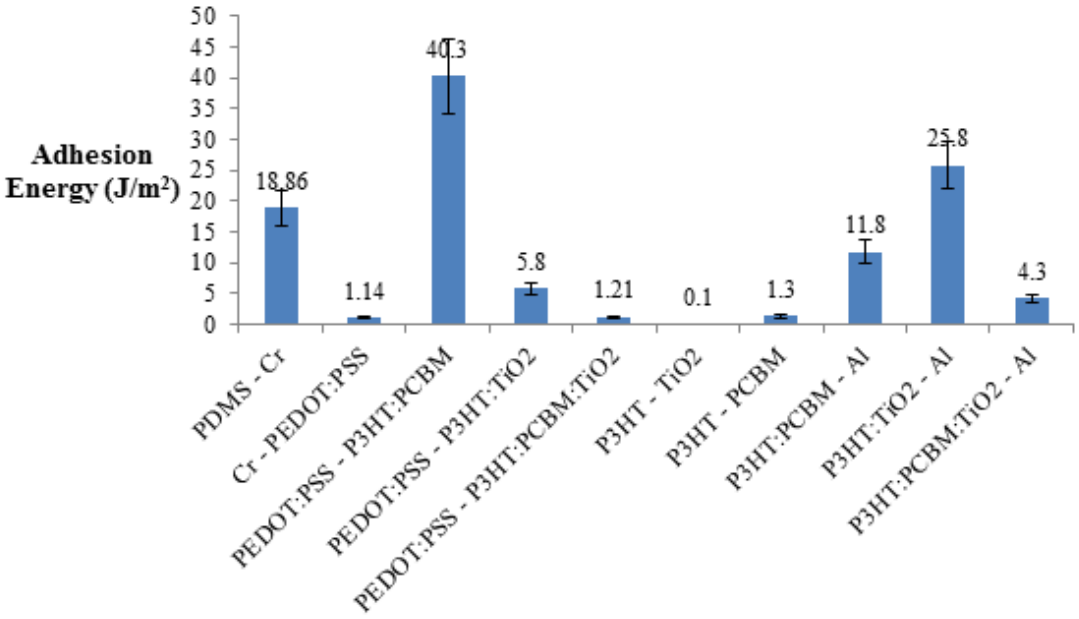

Figure 4.9: Interfacial adhesion energies in flexible organic and composite organic/ inorganic solar cell.

Chapter 5

Lamination of Organic Solar Cells and Organic Light Emitting Devices: Models and Experiments

In this chapter, a combined experimental, computational, and analytical approach is used to provide new insights into the lamination of organic solar cells and light emitting devices at macro- and micro-scales. First, the effects of applied lamination force (on contact between the laminated layers) are studied. The crack driving forces associated with the interfacial cracks (at the bi-material interfaces) are estimated along with the critical interfacial crack driving forces associated with the separation of thin films, after layer transfer. The conditions for successful lamination are predicted using a combination of experiments and computational models. Guidelines are developed for the lamination of low-cost organic electronic structures.

The contribution of this work is threefold. First of all, we developed models and conducted experiments to study the contact and interfacial fracture associated with the lamination of organic solar cells and light emitting devices. Secondly, the experimental and theoretical/computational results derive the following important conclusions:

- The contact length ratios increase with increasing pressure.
- The application of pressure may also result in excessive sink-in of trapped particles, which may damage the devices.
- Models suggest that the onset of interfacial crack growth or fracture occurred when the crack driving forces were equal to the measured adhesion energies for the relevant interfaces.
- Kinking in-and-out of cracks is thought to contribute to the partial interfacial separation that is observed during the pull-off stage of the lamination of selected OPV and OLED structures.

Finally, based on these results, we also developed guidelines for successful lamination of thin film structures for OLEDs and OPV cells.

5.1 Introduction

In the recent years, several deposition techniques have been used for the fabrication of organic solar cells and organic light emitting devices (OLEDs) [30, 33, 43, 69, 124]. These include cold welding [1], transfer printing [108], and lamination techniques

[33, 43, 69, 124] . In the case of lamination, deposition parameters, such as applied force for pre-lamination, pull-off force, and surface roughness must be controlled for successful lamination [12, 108]. In most cases, the presence of particles (e.g., silicon, dust, and organic materials) in clean room environment cannot be ignored. Such particles are trapped at the interfaces between layers during the fabrication of OLEDs and organic solar cells (organic photovoltaic cells (OPVs)) [12]. This results in the fabrication of micro-voids and partial contacts at the interfaces of layered electronics [1, 12].

Furthermore, during lift-off (separation of stamp from the transferred layer) in the process of lamination, stress concentrations occur at the edges of the entrapped voids/cracks. Since these can lead to interfacial plasticity or cracking, there is a need to understand the stresses and crack driving forces associated with contacts and pull-off stages of prelamination and pull-off forces. It is also important to identify the processing windows for contact and pull-off without indicating damage to organic electronic devices.

Since OPVs and OLEDs require charge transport across interfaces in layered structure (as shown in Figure 5.1), the process of charge transport across interfaces can be hindered by entrapped voids/cracks that are formed during contact and lamination processes [50]. Conversely, the contact between adjacent layers can be enhanced by increased pressure and interfacial adhesion. This can improve charge transport across layer structures that are relevant to organic solar cells and light emitting devices. However, excessive pressure can also lead to sink in of the interfacial

impurities and damage to the devices [21]. There is, therefore, a need for models that can guide the design of impurities.

Prior work [21, 33, 69] has been carried out on the lamination of solar cells, light emitting devices, and flexible batteries. Lee *et al.* [69] have demonstrated the lamination of top electrode in semitransparent organic photovoltaic cells. Low temperature lamination processes have also been studied by Guo *et al.* [33], while Huang *et al.* [43] have described a one-step process for the fabrication of semitransparent polymer solar cells. Furthermore, Hu *et al.* [41] have used a lamination process to integrate Li-ion battery materials onto a single sheet of paper. Cao *et al.* [12], Kim *et al.* [57] and Akande *et al.* [1] have reported a cold welding technique for the fabrication of gold-gold and gold-silver thin films that are relevant to OLEDs, while a computational approach has been used by Tucker *et al.* [108] to improve the overall quality of film transferred during the lamination of electronic devices.

However, most of the prior work on the lamination of organic solar cells and organic light emitting devices has involved experimental work, with limited modeling. There is, therefore, a need for combined experimental, computational, and analytical approaches that are designed to provide general insights for the design of lamination processes that are relevant to OPVs and OLEDs. This will be explored in this chapter using a combination of experiments and models that are designed to provide insights for the design of lamination processes that are relevant to OLEDs and OPVs. Following the introduction in Section 5.1, contact and pull-off models are presented in Section 5.2. The experimental procedures are then described in Section 5.3, before

presenting the results and discussion in Section 5.4. Salient conclusions arising from this work are summarized in Section 5.5.

5.2 Modeling

In an effort to laminate low-cost organic solar cells, analytical modeling and computational modeling were used to study interfacial contacts that occur during pre-lamination, as well as the interfacial failure that occurs during the interfacial separation associated with the lamination process. The success of the lamination depends on which of the two interfaces involved in the process fails first (Figure 5.2) [108].

If the top interface (between the poly-di-methyl-siloxane (PDMS) stamp and the transferred layer) fails before the critical condition for bottom interfacial failure is reached between the transferred layer and the substrate, the lamination is considered to be successful [108]. However, if the interface between the transferred layer and the substrate fails before the critical condition for interfacial failure between the PDMS stamp and the transferred layer, the lamination is deemed unsuccessful. The various possible results of separation in the lamination process have been described by Tucker *et al.* [108].

5.2.1 Adhesive Surface Contacts

Structures of OPV and OLED cells are typically fabricated from multilayers in contact. Each of these layers should have the right work function alignment for

increased charge transport to occur across the interfaces. However, improved contact at inorganic/organic and organic/organic material interfaces can also be enhanced by improved adhesion [120] and the application of pressure [21]. There is, therefore, a need to explore the effects of adhesion and pressure on the contacts between adjacent layers in organic electronic structures.

In the case of low cost lamination techniques that are used for the fabrication of OPVs and OLEDs, the layer to be laminated is often coated onto a PDMS stamp before transferring it to a substrate. During this process, as the coated PDMS stamp approaches the layered substrate (Figure 5.3(a)), the presence of distributed particles limits the contact with the underlying substrate. This results in the formation of voids as the layers wrap around the surface of impurities to create interfacial voids [12]. Such particles have been revealed in prior focused ion beam microscopy work by Akande *et al.* [1]. These have shown that nano-scale and micro-scale voids can form at the interfaces, depending on the sizes of the interfacial impurities (Figures 5.3(c) and 5.3(d)). Hence, the application of pressure can increase the contact of stamps around interfaces that are relevant to OPVs and OLEDs. The surface contact length that can be achieved can be estimated using an analytical model of contact around a dust particle. This is done by considering a scenario in which the particles of heights, h, are idealized between the transferred layer of thickness, t_f, and the substrate of thickness, t_s. The transferred layer can be likened to a cantilever beam that bent to an S-shape (Fig. 5.2(d)) [1, 12] under uniform compressed force, F, on the stamp.

Table 5.1: Properties of the materials used in the modeling.

Material	Young's modulus (GPa)	Poisson ratio	References
Particle	70	0.3	[108]
MEH:PPV	11.5	0.3	[21]
PEDOT:PSS	1.56	0.3	[21]
P3HT:PCBM	6.02	0.35	[105]
Glass	69	0.3	[99]
PDMS	0.003	0.3	[5, 106]

The length, L, of the layered structure is given by

$$L = S + L_c, \tag{5.1}$$

where L_c is the length of the contact and S is the length of the void. The relationship between the contact length and applied force, F, (the detailed derivation is presented in Appendix A) is given by

$$\frac{L_c}{L} = 1 - (\frac{3E_f t_f^3 hw}{2FL^3})^{\frac{1}{4}}, \tag{5.2}$$

where w and E_f are the width and the Young's modulus of the transferred layer, respectively. Using the material properties presented in Table 5.1 [5, 21, 99, 105, 108], the normalized contact length can be calculated as a function of the applied compressive force.

5.2.2 Fracture Mechanics Modeling

The lamination of a thin film layer from a coated stamp to a substrate is basically in two stages: pre-lamination and lift-off. During pre-lamination, a compressive force is applied to the stamp to ensure that the layer makes good contact with the substrate. In the case of lift-off, a lift-off force is applied to separate the stamp from the laminated layer. This lift-off process will be considered as an interfacial fracture process in this study. During the pre-lamination process, the application of uniform compressive force (as described above in Section 5.2.1) can induce stresses in layered organic electronics. The stress concentrations become more significant when the dust particles are sandwiched between the interfaces. This can lead ultimately to interfacial crack growth and fracture in the layered structure.

Prior work on the fracture mechanics modeling of pre-lamination and interfacial fracture of OLEDs and OPVs has been carried out by Tucker *et al.* [108] for transfer printing. However, the sizes of the particle can affect the interfacial mechanics during the separation of stamps from the laminated structures, as described by Cao *et al.* [12]. During the separation process at the micro scale (Figure 5.2), the following are possible:

- steady interfacial delamination between the transferred layer and substrate-unsuccessful lamination (Figure 5.2(b));
- steady interfacial delamination between PDMS stamp and transferred layer-successful lamination (Figure 5.2(c));

- possible simultaneous delamination in interfaces of the transferred layer/substrate, and the PDMS stamp/ transferred layer-partial lamination (Figure 5.2(d)).

In an effort to model the fracture processes involved in lift-off process, Figure 5.2 shows an idealized nano particle between the layered interfaces produced after pre-lamination. Edge cracks are also idealized between the transferred layer and stamp and/or between transferred layer and substrate. The energy release rates at the tips of the edge cracks are measures of the crack driving force. In general, the energy release rate of the interfacial crack between the laminated film and the substrate is a function of plane strain elastic moduli of the film, $\bar{E}_f$, and substrate, $\bar{E}_s$, the length of top interfacial crack, d_t, the length of the bottom interfacial crack, d_b, the thickness of the film, t_f, thickness of the substrate, t_s, and the lift-up stress, σ. This is given by

$$G = f(\bar{E}_s, \bar{E}_f, t_f, t_s, d_b, d_t, \sigma), \tag{5.3}$$

where $\bar{E}_f = E_f/(1-\upsilon^2)$ and $\bar{E}_s = E_s/(1-\upsilon^2)$. Using the Buckingham pi-theorem method of dimensional analysis (Appendix B), Equation (5.3) can be expressed as

$$G = f(\frac{\bar{E}_s}{\bar{E}_f}, \frac{t_s}{t_f}, \frac{d_b}{t_f}, \frac{d_t}{t_f})\frac{\sigma^2 t_f}{\bar{E}_f}. \tag{5.4}$$

Since $\sigma = F_{\text{lift-off}}/wL$, where $F_{\text{lift-off}}$ is the lift-up force, Eq. (5.4) can be written as

$$G = f(\frac{\bar{E}_s}{\bar{E}_f}, \frac{t_s}{t_f}, \frac{d_b}{t_f}, \frac{d_t}{t_f})\frac{F^2_{\text{lift-off}} t_f}{w^2 L^2 \bar{E}_f}, \tag{5.5}$$

where w and L represent the width and length of the structure, respectively.

5.2.3 Computational Modeling

The ABAQUS^TM software package (ABAQUS 6.12, Dassault Systèmes Incorporation, Rhode Island) was used to simulate the changes of contact profiles between the transferred layer and the substrate during pre-lamination along with the possible interfacial failure during the separation of the stamp from the transferred (laminated) layer. First, the effects of applied forces (on the surface contact lengths of the active layers of OPV cells and OLEDs) were simulated on poly(3,4-ethylenedioxythiophene):polystyrene sulfonate (PEDOT:PSS)-coated substrates. It was also assumed that particles are sandwiched between the laminated layer and the substrate. The size ranges ($\sim 0.1 - 10\mu m$) are typical of particles that are present in clean room environments. These include silicon, organics, and other dust particles that are often found in the clean room environment [12].

By considering a unit width ($w = 1$), axisymmetric models were developed using the ABAQUS software package. A four-node elemental mesh was used. The elements were dense near the particles and the contact surface (Figure 5.4). The bottom boundary of the substrate was fixed for stability during the simulations, while a range of uniform forces ($0\ N - 500\ N$) was applied to the top of the stamp (Figure 5.5). The materials used (Table 5.1) were assumed to exhibit isotropic behavior. Also, the height of the particle was varied, while the length of the contact surface was studied as a function of the applied force. This was done for laminating layers of model OPVs and OLEDs.

In the case of interfacial failure (during the separation of PDMS stamps from the laminated layered structures in the lift-off process in lamination), 2D models (with

a unit width) were built using the ABAQUS software. These were used to study the interfacial cracking between the laminated layer and the stamp (top interface), as well as the interfacial cracking between the laminated layer and the substrate (bottom interface). Again, a four-node elemental mesh was used, while the elements were dense near the crack tips. The finite element simulations were used to determine the interfacial fracture energies corresponding to the lift-off forces that were applied to separate the stamps from the laminated film materials.

In the lamination process, two different interfaces (the top and the bottom) are possible. By assuming respective existing edge cracks of lengths, d_t and d_b, at the top and bottom interfaces, the energy release rate at the tip of the edge crack at the top interface is denoted as G_t, while the energy release rate at the tip of the edge crack at the bottom interface is denoted as G_b. The thicknesses of the layers were maintained constant, while the energy release rates of the crack tips were calculated using J-integral as functions of the crack length. The energy release rates of the interfacial crack tips were computed for a range of applied lift-off forces.

The success of the lamination process can be explained in form of differentials of the driving forces of the propagating cracks along the interfaces that are involved in the process [108]. At a critical condition, the differential of the interfacial energy release rates (G_t^c and G_b^c) of the edge cracks at the top and bottom interfaces can be expressed as

$$\frac{G_t}{G_b} = \frac{G_t^c}{G_b^c} \tag{5.6}$$

where G_t^c and G_b^c are the critical interfacial energy release rates at the top and bottom interfaces, respectively.

If $G_t/G_b > G_t^c/G_b^c$, the interfacial crack will propagate along the top interface. This will result ultimately in the delamination of the stamp from the transferred layer. In this case, the lamination is successful. However, the lamination will be considered unsuccessful, if $G_t/G_b < G_t^c/G_b^c$; the crack propagates along the bottom interface, causing delamination of the laminated layer from the substrate. In these two scenarios, the lift-up force for successful lamination of materials in OPVs and OLEDs can be predicted.

5.3 Experimental Methods

5.3.1 Pre-lamination of Layers of OPV Cells and OLEDs

First, the PDMS substrate was prepared by mixing a Sylgard 184 silicone elastomer curing agent with a Sylgard 184 silicone elastomer base (Dow Corning Corporation, Midland, MI) with a 1 : 10 weight ratio. Then, the mixture was then processed under a vacuum pressure of 6 kPa for 30 min. This was done to eliminate all of the possible bubbles. The processed PDMS was then poured into a flat aluminum mold with dimensions of 15 $mm \times 10\ mm \times 2\ mm$. This was followed by annealing in an oven at 80 ℃ for 2 hours, resulting in the formation of an $\sim 2\ mm$ thick PDMS stamp. The PEDOT:PSS solution (Hareous, Clevios, Hanau, Germany) was spin-coated onto a clean glass slide at 3000 rpm for 1 min to obtain a film with thickness of 100 nm.

In the case of the OLED, the poly [2-methoxy-5-(2-ethyl-hexyloxy)-1,4-phenylene vinylene] (MEH-PPV) solute (Sigma Aldrich, St. Louis, MO) was mixed with chloroform (at a 5 g/l solute-solvent ratio) to form a solution. The mixture was stirred continuously for 6 h at room-temperature before passing it through a 0.45 μm teflon filter. The cured PDMS was attached to a flat stub using a double-sided tape. This was done before dip coating the PDMS stamp with MEH-PPV solution. The stub was then attached to the head of an Instron machine (Instron 5848, Canton, MA, USA) along with the PEDOT:PSS-coated glass plate that was fixed under the dip-coated PDMS stamp. The MEH-PPV was laminated onto PEDOT:PSS by applying loads in the ranges from 100 N to 500 N for 2 min before lift -off. The stamp was lifted 3 mm apart from the laminated MEH-PPV with the head of the Instron testing machine moving up at a displacement rate of 0.01 mm/s.

For the lamination of the OPV cells, the poly (3-ethylthiophene) (P3HT) (Sigma Aldrich, St. Louis, MO):phenylC61-butyric acid methyl ester (PCBM) (Sigma Aldrich, St. Louis, MO) layer was first prepared by mixing P3HT and PCBM in chlorobenzene. This was mixed in ratio of 1 : 0.8 by weight. The mixture was then stirred continuously for 5 h at room temperature, before spin coating it onto the PDMS stamp at 750 rpm for 30 s. The P3HT:PCBM was laminated from the P3HT:PCBM-coated stamp to the PEDOT:PSS layer with the same protocol that was used for the lamination of the MEH-PPV layer in the OLED structure.

5.3.2 Pull-off of The Laminated and Spin-coated Active Layers

First, a sticky foam pad with a cross sectional area $25mm \times 8\ mm$ was cut and attached to a stub using a double-sided tape. The stub was then attached to the head of an Instron testing machine, while the bottom of the substrate (P3HT:PCBM/PEDOT:PSS/glass) was attached to the bottom stub. Note that the double-sided tape covered the sectional area that was used to pull-off the laminated active layer. The sticky foam pad was then brought into contact with the P3HT:PCBM layer with a near zero force. This was done before scratching off the active layer on the border of the foam pad to maintain the same stress state in each sample. A schematic of the experimental set-up is presented in Figure 5.6.

A load of 100 N was applied to the pad for 60 s. This load was then maintained for another 60 s, before lifting up the head at a rate of 0.01 mm/s. The same protocol was applied for the pull-off of the laminated MEH-PPV, as well as the spin-coated MEH-PPV and P3HT:PCBM. In each case, the force-displacement curves were obtained. The surface of substrate (PEDOT:PSS/glass) was also observed using AFM.

5.4 Results and Discussion

5.4.1 Modeling of Contact During Pre-lamination

The effects of the compressive force (on the contacts between the active layers and PEDOT:PSS-coated substrates of the organic light emitting devices and organic solar cells) are presented in Figure 5.7. The results obtained from the analytical (Eq. (5.2)) and computational modeling show that the contact lengths between pre-lamination of P3HT:PCBM (Figure 5.7(a)) or MEH-PPV (Figure 5.7(b)) onto the substrates. These increase with increasing applied force.

The pre-laminated active layers sink more into the substrate as the applied force increases. The sink-in is also more significant in the case of flexible PDMS substrates. These results suggest that, in the case of rigid and flexible substrates, the desired interfacial contact between the active layers and substrates can be damaged due to excessive applied force. The results also show that, at an applied force of $\sim 250N$, the predicted contact length is $\sim 95\%$ (by FEM) and $\sim 100\%$ (by analytical modeling).

5.4.2 Pre-lamination of Active Layers

In this section, the force needed to separate the stamp from the pre-laminated active layers is determined. It is important to note here that the stamp can be separated from pre-laminated layers if the interfacial contact between the active layers and the substrate is maintained with the applied pre-laminated compressive force. The force-displacement curves for successful pre-lamination of P3HT:PCBM and MEH-PPV onto PEDOT:PSS-coated glass are presented in Figure 5.8. First,

the force increases with increasing displacement, before returning to zero force. At an applied compressive force of $\sim 200N$, the force-displacement curves have a peak $\sim 0.06N$ for pre-lamination of P3HT:PCBM and $\sim 1.10N$ for pre-lamination of MEH-PPV. The peaks of the curves represent the interfacial work of adhesion in the top interfaces (stamp/P3HT:PCBM and stamp/MEH-PPV) of the active layers.

5.4.3 Pull-off Experiments

The results of the pull-off tests (on the laminated and spin-coated active layers) are presented in Figure 5.9. The peaks of the force-displacement curves represent the interfacial adhesion force between the active layers and the PEDOT:PSS-coated substrates. In Figures 5.9(c) and 5.9(d), the adhesion force in laminated P3HT:PCBM/PEDOT:PSS is comparable to the adhesion force, when the P3HT:PCBM is spin-coated onto the substrate.

From the results, the adhesion forces at the interfaces of P3HT:PCBM/PEDOT:PSS coated glass substrate and MEH:PPV/PEDOT:PSS-glass are more than the measured adhesion forces at the interfaces of Stamp/P3HT:PCBM (Figure 5.8(a)) and Stamp/MEH:PPV (Figure 5.8(b)), respectively. This suggests that the lamination of organic active layers of OPV cells and OLEDs can be improved in the case where the active layers are deposited on PEDOT:PPS-coated substrates. Since the adhesion forces between the active layers and the substrates are more than the adhesion forces between stamps and the active layers, the stamps can be removed easily from the laminated active layers, without damaging the interfaces between the active layers and PEDOT:PSS-coated glass.

Typical AFM images of the substrates (after the pull-off of MEH-PPV and P3HT:PCBM) are presented in Figure 5.10. In the case of successful pull-off, no remnant of the MEH-PPV and P3HT:PCBM was observed on the substrates after pull-off (Figures 5.10(a) and 5.10(b)). The patches of the laminated MEH-PPV and P3HT:PCBM layers are evident in the case where the layers are not fully pulled off from the substrate (Figures 5.10(c) and 5.10(d)).

5.4.4 Interfacial Fracture During Lift-off

It is crucial to understand the fracture along the interfaces that are involved in the lift-off stage of the lamination process. For successful lamination of any layer onto a substrate, the stamp must be lifted up successfully, without damaging the interface of interest (laminated active layers/substrates). The different categories of the possible laminations that can be achieved, based on the properties of the interfaces, have been described previously in Section 5.2.2.

First, the bottom interface was maintained intact, with zero edge crack length. This was done to calculate the interfacial energy release rate as a function of edge crack length at the top interface. This was done for both the lamination of P3HT:PCBM and MEH:PPV onto PEDOT:PSS-coated glass substrates. The interfacial energy release rates of the crack tips at the bottom interfaces (P3HT:PCBM/PEDOT:PSS-coated glass and MEH:PPV/ PEDOT:PSS-coated glass) were also calculated for different lengths of the bottom edge cracks, keeping the top (stamp/P3HT:PCBM and stamp/ MEH:PPV) edge crack length at zero. In both cases, the top and bottom energy release rates increased with increasing crack

length. The differences between the energy release rates at the top and bottom interfaces can be observed clearly at short crack lengths (Figure 5.11). However, at longer crack lengths, there were no significant differences between the energy release rates of the top and bottom interfaces. Similar results have been reported by Tucker *et al.* [108]. The significant difference in the energy release rates at short crack lengths is attributed to the fact that the cracks propagate along the top and bottom interfaces, as the stamp is lifted off from the laminated layer. As such, the PDMS stamp absorbs the deformation due to lift-off.

The delamination of the stamp from the laminated layer, and the laminated layer from the substrate, during the lift-off process, becomes more interesting at the micron-scale, considering the voids that are produced as a result of the wrapping of the thin films around the nano- and micro-particles that are trapped between the substrates and laminated layers. Figure 5.12 presents the results of the interfacial fracture that occurs during the lift-off process.

For the lamination of both P3HT:PCBM and MEH:PPV layers, the initial energy release rate at the top interface was the maximum value. This decreased to zero, while the energy release rate at the bottom interface (that was initially at zero) increased, as the energy release rate at the top interface decreased. Meanwhile, the energy release rates of the top and bottom cracks decreased, as the length of the crack (void) created by particle increased.

Furthermore, Figure 5.12 shows the energy release rates G_{void} at the tips of the cracks, which were created by the trapped particles, increased with increasing size of the particle and the length of the bottom interface edge crack. However, G_{void} is

very small for small particle size even as the bottom crack length increases. This is an indication that the particles can weaken the adhesion of the interface of interest during lamination. It is, therefore, important to ensure surface cleaning using laser or ozone/UV surface cleaner prior to lamination, for improving interfacial contact and adhesion between the active layer and the substrate.

The success of lamination of the active layers, P3HT: PCBM and MEH:PPV, of the electronics can be predicted in form of the differential of the interfacial energy release rates of the edge cracks at the top and bottom interfaces. This is shown in Figures 5.13(a) and 5.13(b), in which computed energy release rates are presented as a function of the normalized bottom crack length. In both cases (of the active layers), the differential energy release rates decrease with increasing normalized bottom crack length, while the increasing particle size increases the energy difference. For a critical measured value of the interfacial energy difference, we can predict the success of the lamination (as described in Section 5.2.3).

It is of interest to compare the computed crack driving forces with the adhesion energies [6, 45, 107, 120] and interfacial fracture energies [22] reported previously for interfaces that are relevant to OLEDs and OPVs. These are summarized in Table 5.2. The results obtained from the computations are comparable to the previously reported results. In the case of the OLED, in which MEH:PPV film is laminated onto PEDOT:PSS-coated substrates using PDMS stamp, the measured interfacial energy along the bottom interface (PEDOT:PSS/MEH-PPV) is greater than the energy along the top interface (MEH-PPV/Stamp). The small value of the interfacial energy at the top interface is attributed to the hydrophobic nature of the PDMS stamp,

which facilitates successful lamination. The tendency of the crack paths to remain at the interface, or deviate away from the interface, can influence the magnitude of the computed interfacial energy, as well as the measured interfacial adhesion and fracture energies.

Table 5.2: Interfacial adhesion and fracture energies in OLEDs and OPV cells.

(a) Measured and computed interfacial energies			
P3HT:PCBM/PEDOT:PSS (bottom)	2.6 ([107])	1.6 ([22])	1.57 (this work)
MEH-PPV/PEDOT:PSS (bottom)	15 ([6, 120])	...	2.42 (this work)
P3HT:PCBM/PDMS (top)	...	...	0.75 (this work)
MEH-PPV/PDMS (top)	0.028 ([45])	...	0.36 (this work)

(b) Interfacial energy ratios	
Laminated layer	Computed $G_{top} = G_{bottom}$
P3HT:PCBM	0.478
MEH-PPV	0.149

Similarly, in the case of OPV, the interfacial energy at the bottom interface (PEDOT:PSS/P3HT:PCBM) is more than the energy at the top interface (P3HT:PCBM/Stamp). The crack paths being remained or deviated at the interface can also be attributed to the variation in the magnitude of the computed energies , the measured interfacial adhesion, and fracture energies. Hence, interfacial fracture should occur when the interfacial fracture toughness values and the adhesion energies are lower than the substrate critical energy release rates. However, the criteria for interfacial cracking versus substrate cracking also depend on mode mixity, as shown in the earlier work by Evans *et al.* [26, 27, 35] and Rahbar *et al.* [90].

Finally, it should be noted that interfacial cracks can kink in-and-out of interfaces, giving rise to patches of partial interfacial separation during material pull-off. This can occur when the mechanisms of micro-void nucleation around inclusions and interfacial impurities link with dominant interfacial cracks in ways that promote the extension of interfacial cracks into adjacent layers. In such cases, the crack can kink in-and-out of interfaces depending on the distribution of the inclusion/impurities that include the formation of voids that link up with the propagating cracks. This has been shown in earlier work by Rahbar *et al.* [90] using a combination of finite element simulations and experiments. The kinking of cracks (in-and-out of interfaces) has also been discussed in prior work by Evans *et al.* [26, 27, 35]. Their work suggests that the criteria for interfacial cracking depend on the crack driving forces, as well as on the mode mixity.

However, it did not consider the nano-scale mechanisms of microvoid nucleation and growth, as observed in the experiments and models of Rahbar *et al.* [90]. Further work is clearly needed to include the effects of inclusion distributions microstructure-based models for the prediction of interfacial/substrate cracking and the kinking of cracks during layer pull-off processes.

5.4.5 Implications

The results presented above are significant for the fabrication of cheap organic solar cells and organic light emitting devices. They can be used as guidelines for the design of fabrication of stamps and lamination conditions that can help to improve surface contact and device performance. Furthermore, in multilayered OLEDs and OPV

Table 5.3: Summary of the guidelines for successful lamination of thin film structures of OLEDs and OPV cells.

Void lenth(μm)	P3HT:PCBM	MEH-PPV	Result of lamination
2.0	$d_b/t_f \geq 20.0$	$d_b/t_f \geq 25.0$	Successful (unsuccessful otherwise)
5.0	$d_b/t_f \geq 24.5$	$d_b/t_f \geq 31.0.0$	Successful (unsuccessful otherwise)
9.0	$d_b/t_f \geq 25.0$	$d_b/t_f \geq 33.0$	Successful (unsuccessful otherwise)
12.0	$d_b/t_f \geq 32.0$	$d_b/t_f \geq 34.0$	Successful (unsuccessful otherwise)

cells, the alignments of the layer work functions are very important in the design of improved charge transport between layers. Lamination is, therefore, a good candidate for improving contact in the multilayered structures of OLEDs and OPV cells. The application of pressure (during lamination) also tends to improve interfacial contact. However, too much pressure may cause excessive sink in and device damage. Finally, the results above provide guidelines for successful lamination of thin film structures for OLEDs and OPV cells. These guidelines are summarized in Table 5.3.

5.5 Conclusion

This chapter presents the results of a combined experimental and theoretical/computational study of the contact and interfacial fracture associated with the lamination of organic electronic structures.

1. A combination of analytical and computational models is used to study the effects of pressure on the contacts around dust particles that are trapped between adjacent layers in model OLED and OPV structures. The studies show that the contact length ratios increase with increasing pressure. However, the

application of pressure may also result in excessive sink-in of trapped particles, which may damage the devices.

2. The subsequent pull-off stage of lamination was considered as an interfacial fracture process. This was studied using computational models of interfacial crack driving forces. The models suggest that the onset of interfacial crack growth or fracture occurred when the crack driving forces were equal to the measured adhesion energies for the relevant interfaces.

3. The effects of pre-existing defects need to be considered in greater detail, if we are to predict the critical conditions for the kinking in-and-out of cracks from different interfaces. Such kinking in-and-out is thought to contribute to the partial interfacial separation that is observed during the pull-off stage of the lamination of selected OPV and OLED structures.

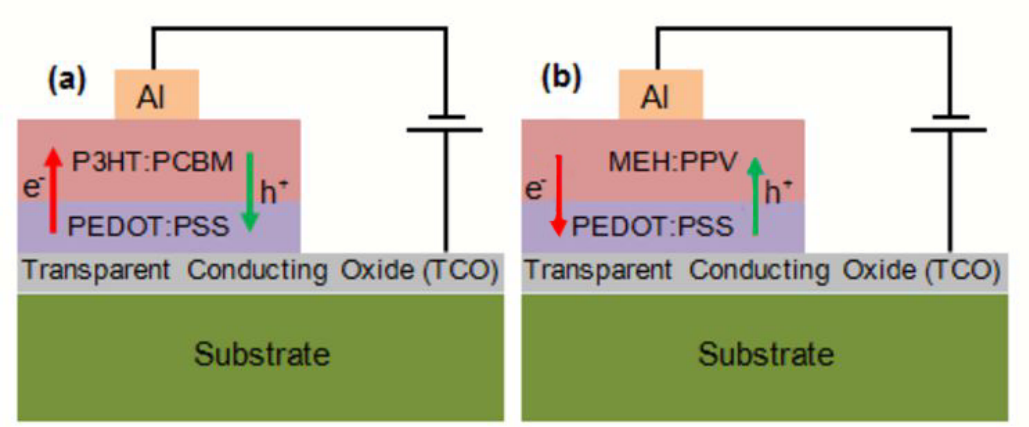

Figure 5.1: Schematics of simple (a) OPV structure and (b) OLED structure.

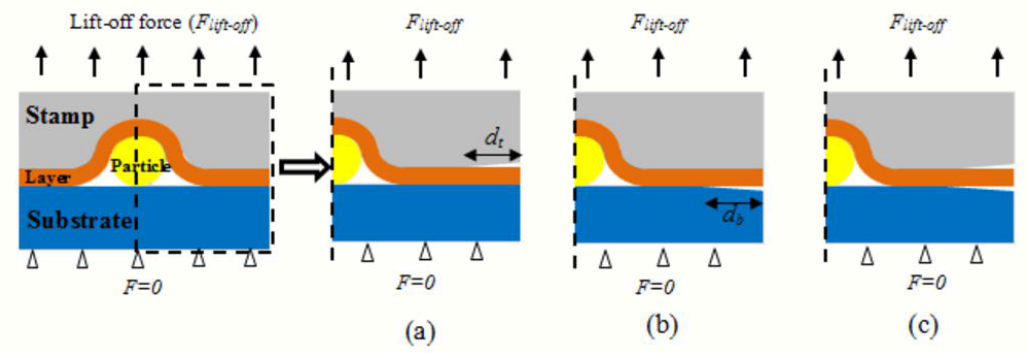

Figure 5.2: Schematics of micro scale models of interfacial fracture during the lift-off process of the lamination (a) model of the lift-off process after the press down of the layer on the substrate, (b) axisymmetric model of successful lift-off, (c) axisymmetric model of unsuccessful lift-off, and (d) axisymmetric model of partial interfacial fracture.

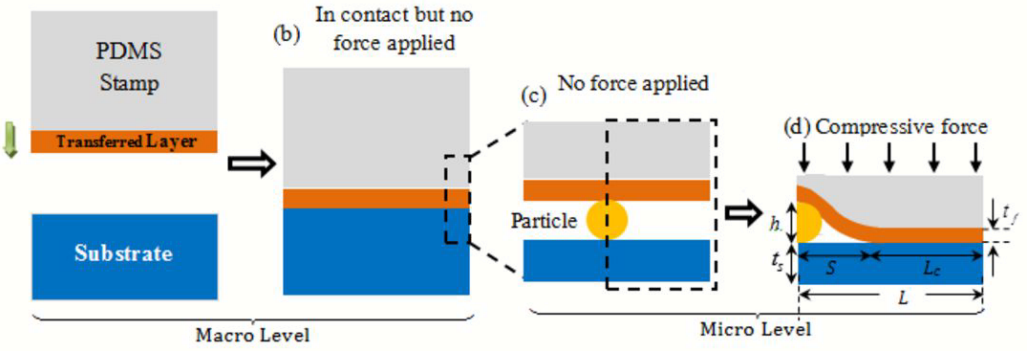

Figure 5.3: Schematics of micro/macro scale models of adhesion and contact during pre-lamination process of the lamination.

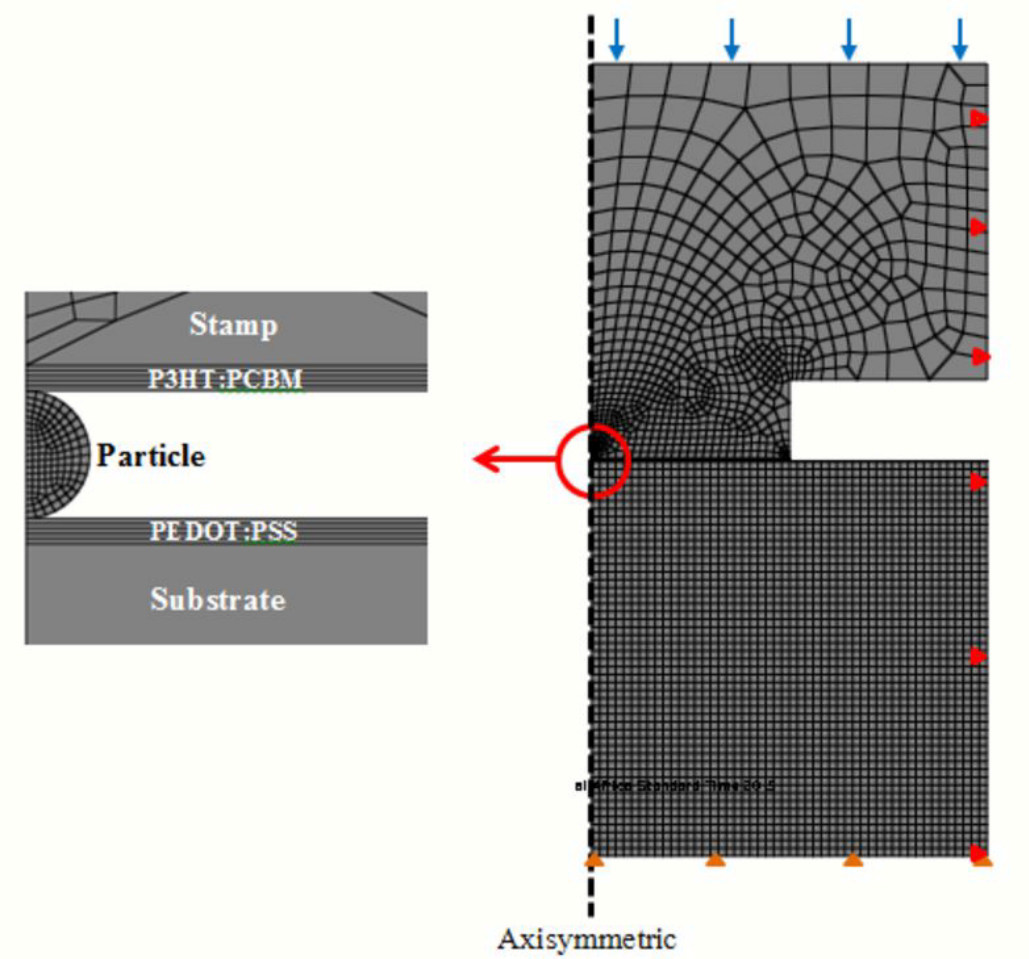

Figure 5.4: Geometry and mesh of finite element model of surface contact during pre-lamination of active layers of organic solar cells and light emitting devices.

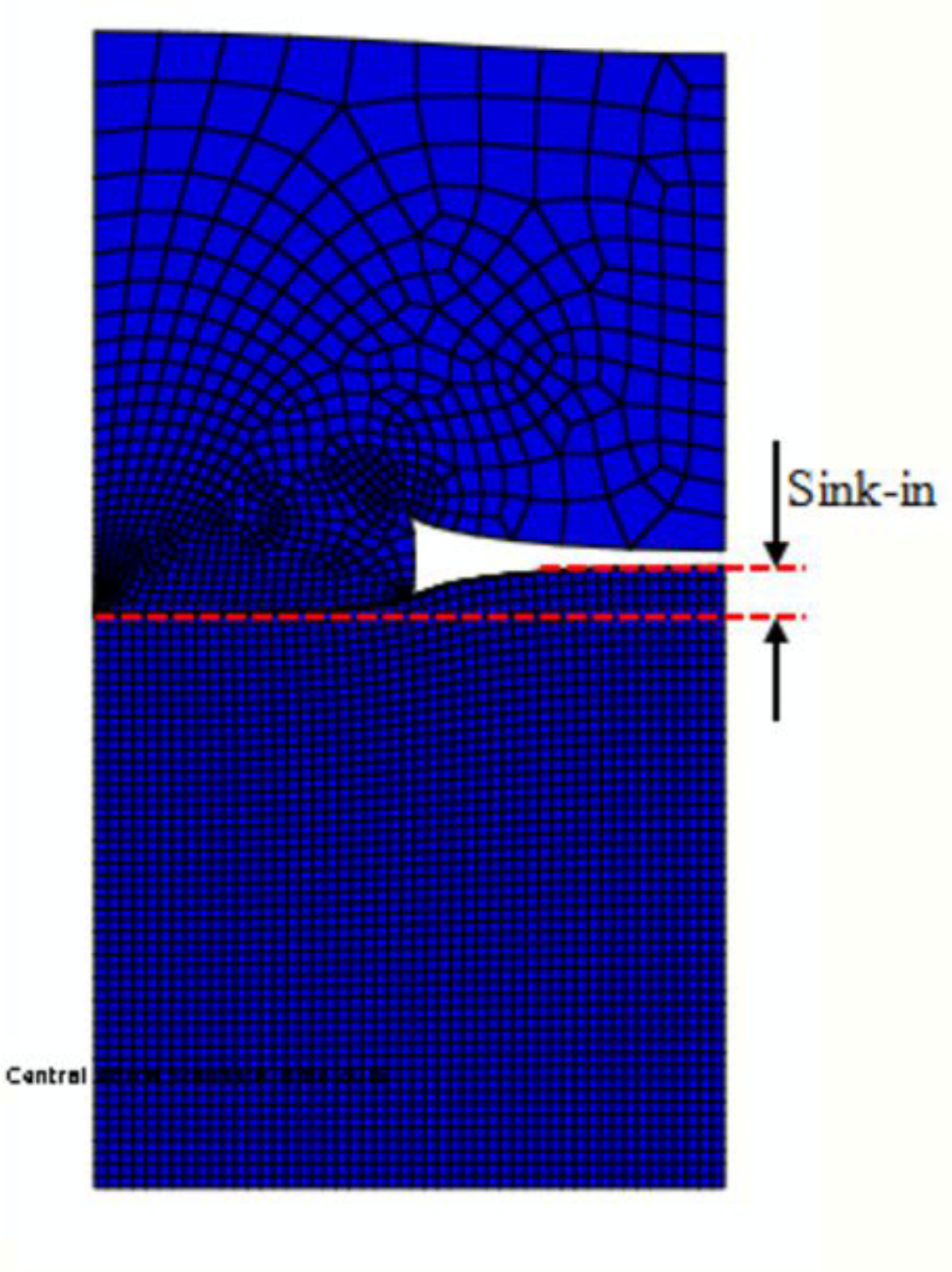

Figure 5.5: FEM of surface contact model after applying a range of forces ($0N \sim 500N$).

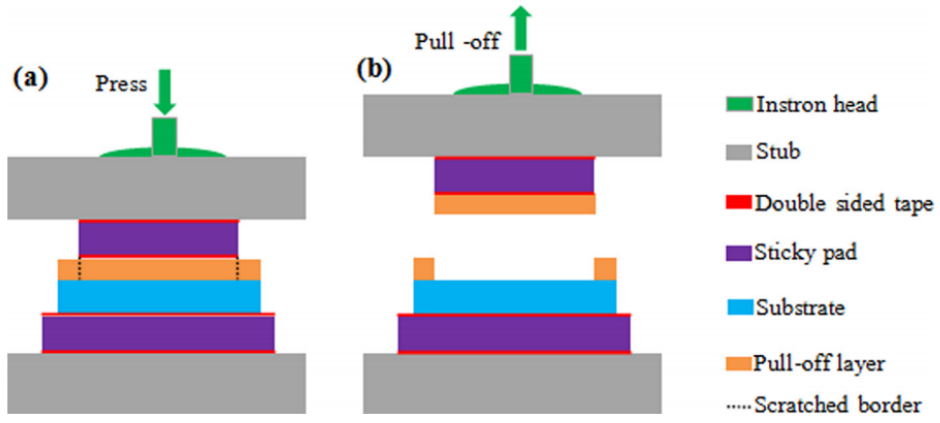

Figure 5.6: Schematic of experimental pull-off of spin-coated and laminated layer, showing the (a) press down process and (b) pull-off process.

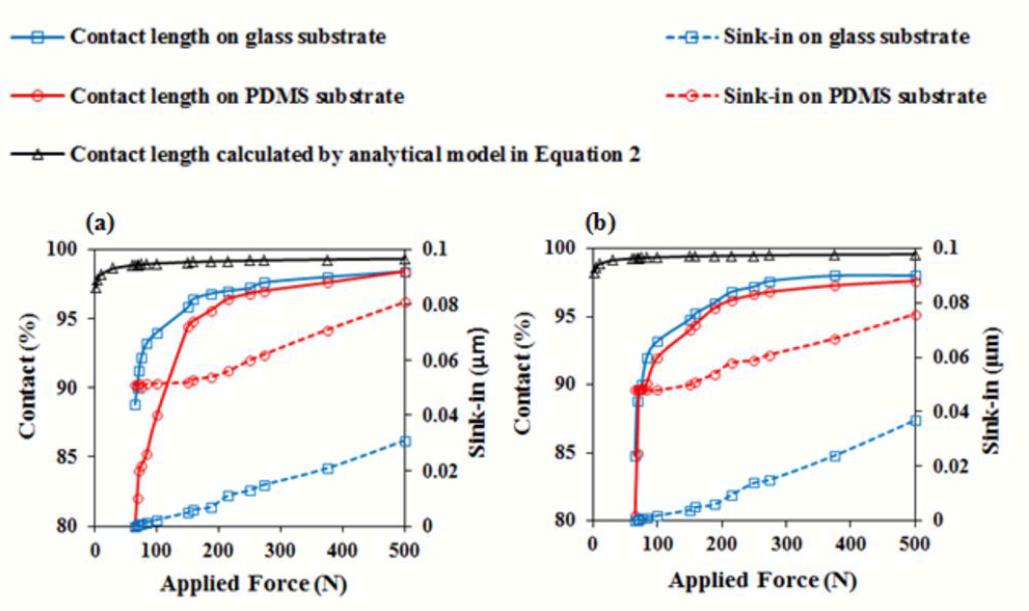

Figure 5.7: Effects of force on contact profiles of (a) P3HT:PCBM on PEDOT:PSS-coated substrate and (b) MEHPPV on PEDOT:PSS-coated substrate.

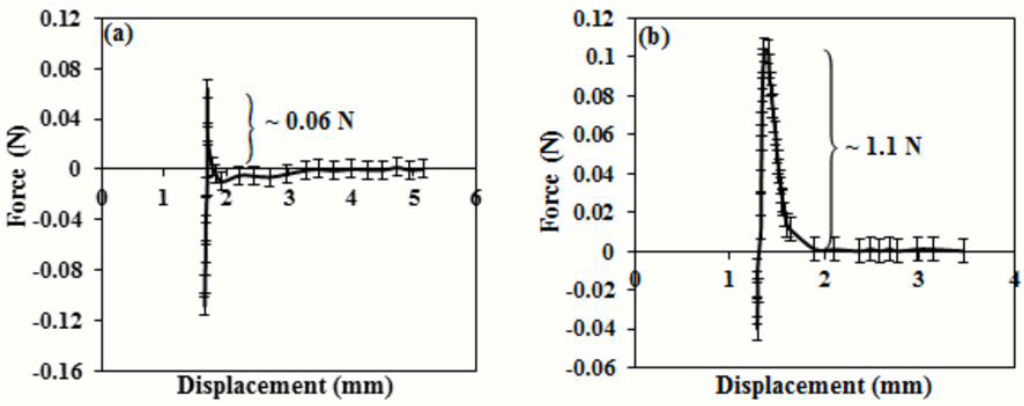

Figure 5.8: Force-displacement curves of pre-lamination of (a) P3HT:PCBM and (b) MEH-PPV on PEDOT:PPS-coated glass. The peaks represent the interfacial adhesion forces along PDMS/ MEH-PPV and PDMS/P3HT:PCBM interfaces during lift-off of the stamp from P3HT:PCBM and MEH-PPV.

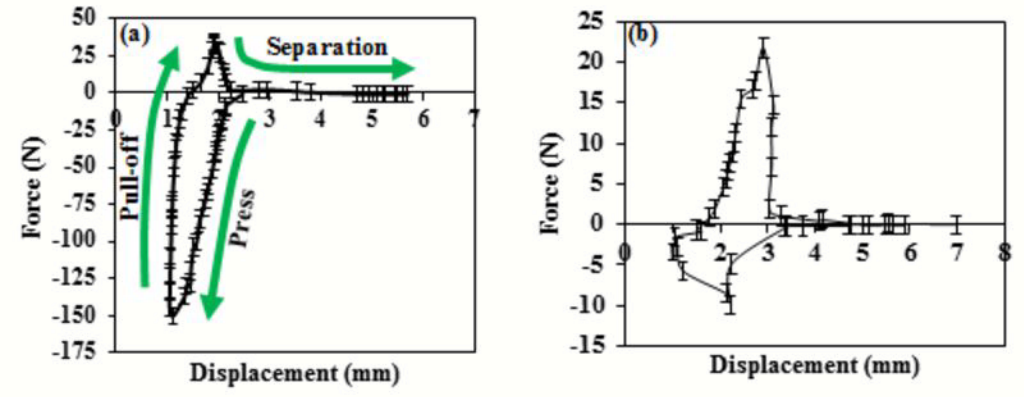

Figure 5.9: Force-displacement curves of pull-off of (a) spin-coated MEH-PPV, (b) laminated MEH-PPV, (c) spin-coated P3HT:PCBM , and (d) laminated P3HT:PCBM.

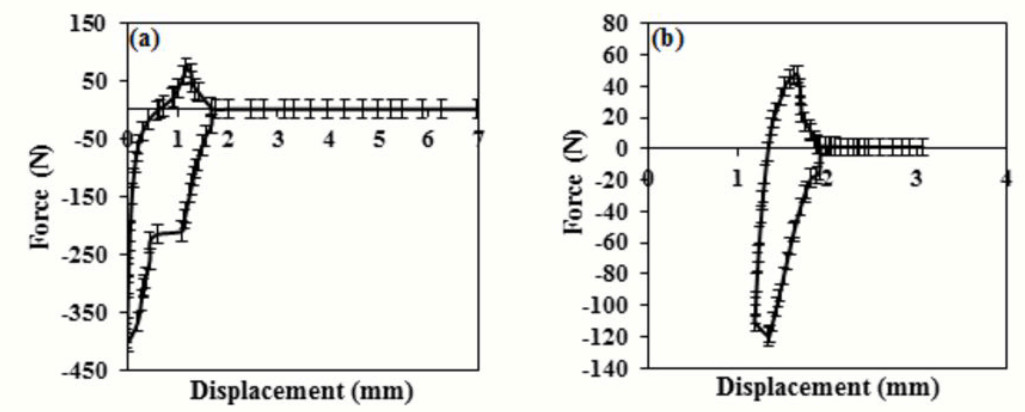

Figure 5.10: Samples of the AFM images of substrates after pull-off of active layers, MEH-PPV, and P3HT:PCBM for (a) and (b) successful pull-off, (c) and (d) pull-off with remnants left on the substrates.

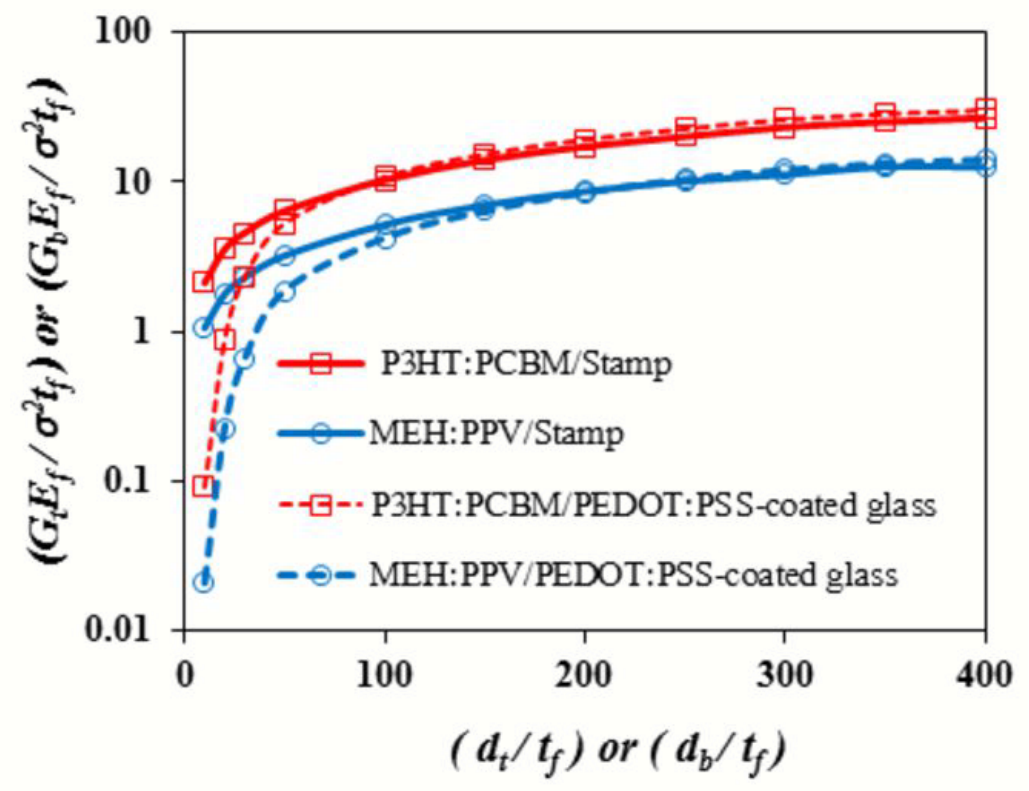

Figure 5.11: The normalized top/bottom energy release rate as a function of the normalized top/bottom crack length, respectively. The energy release rates of the edge cracks at the top interfaces (P3HT:PCBM/Stamp and MEH:PPV/ Stamp) were calculated with no edge crack at bottom interfaces (P3HT:PCBM/PEDOT:PSS-coated glass and MEH:PPV/PEDOT:PSS-coated glass). The energy release rates of the edge cracks at the bottom interfaces were also calculated with no edge crack at the top interfaces.

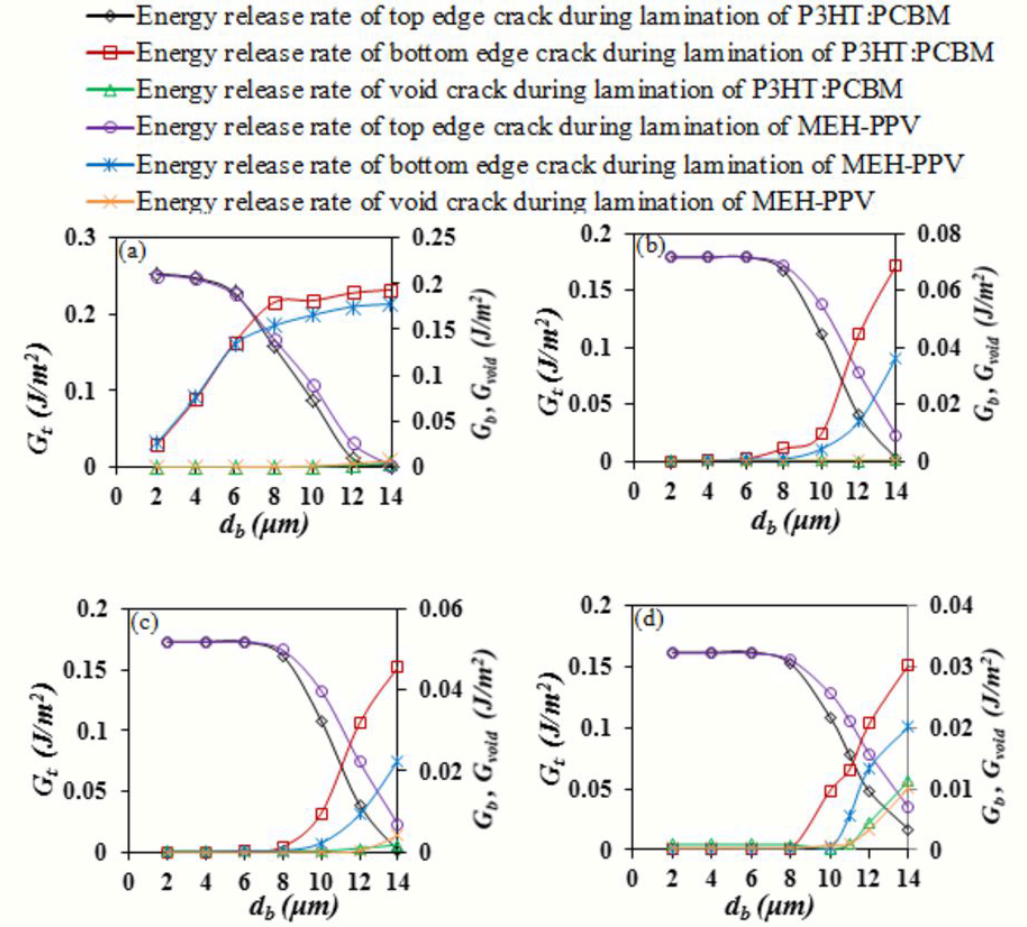

Figure 5.12: Interfacial fracture during lift-up of stamp from laminated P3HT:PCBM and MEH:PPV on PEDOT:PSS-coated substrates for different particle diameters. (a) $2\mu m$, (b)$6\mu m$, (c) $9\mu m$, and (d) $12\mu m$. The concomitant energy release rates of the tips of the edge cracks at the top and bottom interfaces as functions of bottom crack length. Here, the length of the top edge crack is $6\mu m$, while the thickness of the active layers is maintained at 200 nm.

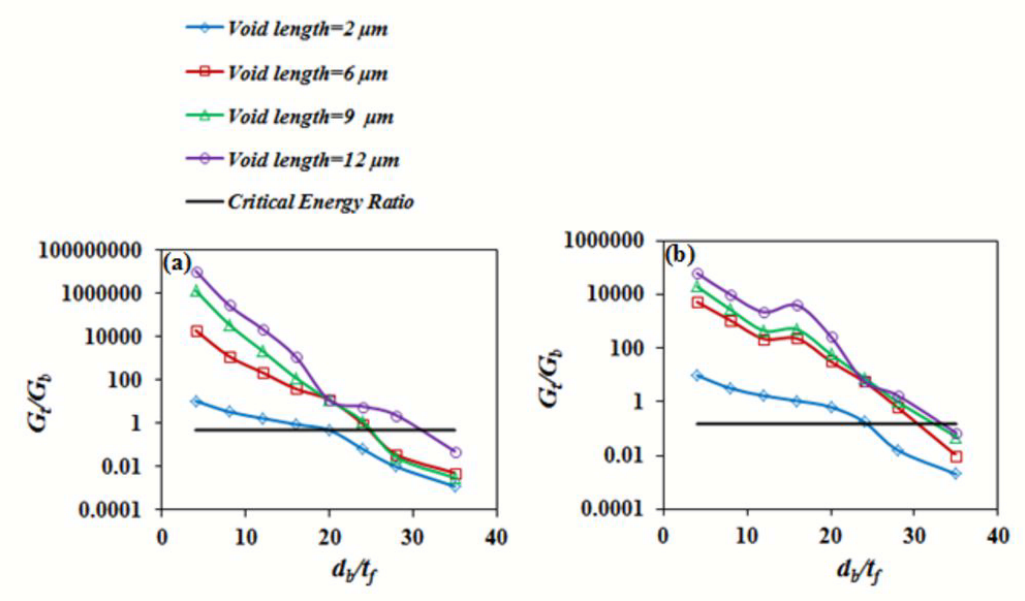

Figure 5.13: Ratio of the interfacial energy release rates G_t/G_b as a function of the normalized bottom crack length (d_b/t_f), showing the influence of the particle size for (a) lamination of P3HT:PCBM, (b) lamination of MEH-PPV. Here, the thickness of the active layer is 200 nm.

Chapter 6

Conclusions and Future Work

6.1 Conclusions

6.1.1 Adhesion in Flexible Organic and Composite Organic/Inorganic Light Emitting Device and Solar Cells

The AFM technique can be used to measure and rank the adhesion forces and energies between different layers in flexible organic and composite organic/inorganic light emitting devices and solar cells. This could facilitate the future design of robust flexible organic and composite organic/inorganic light emitting devices and solar cells.

For both the flexible organic and composite organic/inorganic light emitting devices and solar cells, the Cr layer adhered strongly to the PDMS substrate, with a high adhesion energy of 18.9 J/m^2. In the case of the composite organic/inorganic light emitting device, the adhesion energy between PEDOT:PSS and MEH:PPV

was 15 J/m^2, the adhesion energy increased to a higher value of 20.8 J/m^2 between PEDOT:PSS and MEH:PPV:TiO_2 after adding TiO_2 nanoparticles to the MEH:PPV single polymer blend. Also, the adhesion energy between MEH:PPV and Al was 0.8 J/m^2. After adding TiO_2 nanoparticles to the MEH:PPV single polymer blend, the adhesion energy between MEH:PPV:TiO_2 and Al increased to a higher value of 5.9 J/m^2. The composite light emitting device with the MEH:PPV:TiO_2 active layer, therefore, had higher adhesion energies at the two interfaces with its adjacent Al and PEDOT:PSS layers. From the robustness point of view, the active layer of MEH:PPV:TiO_2 adheres better to the adjacent layers than the active layer consisting of MEH:PPV.

In the case of the composite organic/inorganic solar cell, the P3HT:PCBM layer adhered strongly to PEDOT:PSS layer, with the highest adhesion energy value of 40.3 J/m^2. Also, the adhesion energy between PEDOT:PSS and P3HT:PCBM layer was much greater than the adhesion energies of PEDOT:PSS-P3HT:TiO_2 and PEDOT:PSS-P3HT:PCBM:TiO_2. The adhesion energy between PEDOT:PSS and P3HT:TiO_2 was bigger than that between PEDOT:PSS and P3HT: PCBM:TiO_2. Furthermore, the adhesion energy between Al and P3HT:TiO_2 had the highest value of 25.8 J/m^2. This was bigger than the adhesion energies of the Al-P3HT:PCBM:TiO_2 and the Al-P3HT:PCBM. Therefore, from the robustness point of view, the active layer of P3HT:TiO_2 was more robust than the active layer consisting of P3HT:PCBM:TiO_2.

The incorporation of TiO_2 nanoparticles into the active layers of P3HT:PCBM in the organic solar cells reduces the adhesion to the adjacent hole transport and

cathode layers. Therefore, the improvements in charge transport facilitated by TiO_2 must be balanced against potential reductions in the adhesion that might occur as a result of the incorporation of TiO_2 nanoparticles into the active layers of bulk heterojunction solar cells.

6.1.2 Micro-wrinkling and Delamination-induced Buckling of Stretchable Electronic Structure

The evidence of micro-wrinkle and delamination-induced buckle formation is presented on the surfaces of stretchable poly-dimethylsiloxane (PDMS) coated with nano-scale Gold (Au) layers. The wrinkles and buckles are formed by the unloading of pre-stretched PDMS/Au structures after the evaporation of nano-scale Au layers. The wavelengths of the micro-wrinkled and buckled profiles decreased with the increase of pre-strain. The critical buckling stress also decreased with the increase of the wavelength. The pre-strain technique was applied for the measurement of the interfacial fracture toughness between hard and soft materials. The measurements of interfacial fracture toughness for Au films on PDMS substrates are comparable to AFM measurements of adhesion energy. The results suggest that pre-strain-controlled profiles can be considered for potential biomedical and optoelectronic applications. The potential biomedical applications may include implantable biomedical devices for sensing and drug delivery, while the opto-electronic structures may include diffraction gratings and electronic textiles. A basic understanding of micro-wrinkle and buckle formation is useful in the design and

fabrication of micro-scale features in the biomedical applications and opto-electronic structures.

6.1.3 Lamination of Organic Solar Cells and Organic Light Emitting Devices: Models and Experiments

The results of a combined experimental and theoretical/computational study are presented for the contact and interfacial fracture associated with the lamination of organic electronic structures. These are significant for the fabrication of cheap organic solar cells and organic light emitting devices. They can be applied as guidelines for the design of fabrication of stamps and lamination conditions that can help to improve surface contact and device performance. They also provide guidelines for the successful lamination of thin film structures for OLEDs and OPV cells. Lamination is a good candidate for improving contact in the multilayered structures of OLEDs and OPV cells.

A combination of analytical and computational models was applied to study the effects of pressure on the contacts around dust particles that are trapped between adjacent layers in the OLED and OPV structures. The results show that, at an applied force of $\sim 250\ N$, the predicted contact length is $\sim 95\%$ (by FEM) and $\sim 100\%$ (by analytical modeling). The results also show that the contact length ratios increase with the increase of pressure. However, too much pressure may cause excessive sink in of trapped particles and device damage. The pre-laminated active layers sink more into the substrate, with increasing applied force. The sink-in is more significant in the case of flexible PDMS substrates.

The pull-off process of lamination was considered as an interfacial fracture process. This was investigated using computational models of interfacial crack driving forces. The models suggest that the onset of interfacial crack growth or fracture occurs when the crack driving forces are equal to the measured adhesion energies for the relevant interfaces.

6.2 Suggestions for Future Work

The ability to control the surface profiles by micro-wrinkling and buckling may also provide the ability for the biomedical electronic systems to integrate well with biological tissue. For example, prior work [14] has shown that microgrooves with depths and spacings of $\sim 10 - 20\ \mu m$ can promote the contact guidance/alignment of biological cells in ways that can lead to increased cell/surface integration [32] and reduced scar tissue formation. Therefore, future work on wrinkled and buckled structures can facilitate cell/surface interactions and their integration with biological tissue.

Also, the stretchable electronics, which include solar cells and light emitting devices, require the design of robust systems that are stretchable without significant interfacial failure [59]. Hence, there is a need to extend the strain-induced micro-wrinkling and buckling testing technique to a more general framework for the measurement of thin film interfacial fracture toughness.

The kinking in-and-out of interfacial cracks is thought to contribute to the partial interfacial separation that is observed during the pull-off stage of the lamination

of OPV structures. The prediction of such phenomena requires more detailed considerations of the interactions between cracks and pre-existing defects.

Appendix A

Analytical Calculation of Contact Length as A Function of Compressive Force

Let us consider a scenario whereby a particle is at the surface of a substrate. Any film deposited on the substrate bends round the particle like a cantilever beam with a bending energy. This is given by [123]:

$$U_b = \frac{6E_f I h^2}{S^3}, \tag{A.1}$$

where E_f is the film Young's modulus, I is the second moment of inertial, h is the height of the particle, and S is the length of the void created by the particle.

For a rectangular geometry, the contact surface area is given by

$$A_c = L_c \times w, \tag{A.2}$$

where L_c is the contact length and w is the width of the structure. The uniform pressure, P, which is applied to a crosssection area, $A_f = L \times w$, of the film can be related to the corresponding compressive force, F. This is given by:

$$P = \frac{F}{Lw}, \tag{A.3}$$

where L is the length of the structure. Hence, the surface energy between the film and the substrate can be written as the product of the pressure, the contact area, and the height of the particle. This is given by

$$U_s = -\frac{F}{Lw} \times (L_c \times w) \times h = -\frac{FL_c h}{L_c} \tag{A.4}$$

By substituting $Lc = L - S$ into Eq. (A.4), the surface energy becomes

$$U_s = -Fh(1 - \frac{S}{L}) \tag{A.5}$$

The total energy, UT, is the addition of Eqs. (A.1) and (A.5). This is given by

$$U_T = \frac{6E_f I h^2}{S^3} - Fh(1 - \frac{S}{L}) \tag{A.6}$$

The length of the void can be calculated from Eq. (A.6) at equilibrium, $dU_T/d_S = 0$. This is given by

$$S = (\frac{18E_f IhL}{F})^{\frac{1}{4}} \tag{A.7}$$

By substituting the second moment of inertial, $I = wt_f^3/12$, into Eq. (A.7), the length of the void becomes

$$S = L - L_c = (\frac{3E_f t_f^3 hLw}{2F})^{\frac{1}{4}} \tag{A.8}$$

From Eq. (A.8), we write the contact length as a function of the compressive force. This is given by

$$\frac{L_c}{L} = 1 - (\frac{3E_f t_f^3 hw}{2FL^3})^{\frac{1}{4}} \tag{A.9}$$

Appendix B

Interfacial Energy Release Rate

$G = f(\bar{E}_s, \bar{E}_f, t_f, t_s, d_b, d_t, \sigma)$ Number of parameters = 8 Number of fundamental dimension = 3 Number of dimensionless quantities=$8 - 3 = 5$

The core variables are

$$\sigma = [ML^{-1}T^{-2}], \bar{E}_f = [ML^{-1}T^{-2}], t_f = [L].$$

$$\sigma^2 t_f^2 = [M^2L^{-2}T^{-4}][L^2] = [M^2T^{-4}] \tag{B.1}$$

$$\bar{E}_f t_f = [ML^{-1}T^{-2}][L] = [MT^{-2}]. \tag{B.2}$$

By dividing Eq. (B.1) by (B.2)

$$\frac{\sigma^2 t_f^2}{\bar{E}_f t_f} = \frac{\sigma^2 t_f}{\bar{E}_f} = \frac{M^2T^{-4}}{MT^{-2}} = [MT^{-2}]. \tag{B.3}$$

First dimensionless quantity (π_1):

$$G = [MT^{-2}] = \frac{\sigma^2 t_f}{\bar{E}_f},$$

$$\pi_1 = \frac{G\bar{E}_f}{\sigma^2 t_f}.$$

Second dimensionless quantity (π_2):

$$\bar{E_f} = [ML^{-1}T^{-2}],$$

$$\pi_2 = \bar{E_s}[LT^2M^{-1}] = \frac{\bar{E_s}}{\bar{E_f}}.$$

Third dimensionless quantity (π_3):

$$t_s = [L],$$

$$\pi_3 = t_s[L^{-1}] = \frac{t_s}{t_f}.$$

Fourth dimensional quantity (π_4):

$$d_b = [L],$$

$$\pi_4 = d_b[L^{-1}] = \frac{d_b}{t_f}.$$

Fifth dimensional quantity (π_5):

$$d_t = [L],$$

$$\pi_5 = d_t[L^{-1}] = \frac{d_t}{t_f},$$

$$\pi_1 = f(\pi_2, \pi_3, \pi_4, \pi_5),$$

$$\frac{G\bar{E_f}}{\sigma^2 t_f} = f(\frac{\bar{E_s}}{\bar{E_f}}, \frac{t_s}{t_f}, \frac{d_b}{t_f}, \frac{d_t}{t_f}),$$

$$G = f(\frac{\bar{E_s}}{\bar{E_f}}, \frac{t_s}{t_f}, \frac{d_b}{t_f}, \frac{d_t}{t_f})\frac{\sigma^2 t_f}{\bar{E_f}} \tag{B.4}$$

Bibliography

[1] Wali O Akande, Yifang Cao, Nan Yao, and Wole Soboyejo. Adhesion and the cold welding of gold-silver thin films. *Journal of Applied physics*, 107(4):043519, 2010.

[2] Onobu Akogwu, David Kwabi, Swaminadham Midturi, Marcus Eleruja, Babaniyi Babatope, and WO Soboyejo. Large strain deformation and cracking of nano-scale gold films on pdms substrate. *Materials Science and Engineering: B*, 170(1):32–40, 2010.

[3] Onobu Akogwu, David Kwabi, Auxillia Munhutu, Tiffany Tong, and WO Soboyejo. Adhesion and cyclic stretching of au thin film on poly (dimethyl-siloxane) for stretchable electronics. *Journal of Applied Physics*, 108(12):123509, 2010.

[4] VI Arkhipov and H Bässler. Exciton dissociation and charge photogeneration in pristine and doped conjugated polymers. *Physica Status Solidi (a)*, 201(6):1152–1187, 2004.

[5] Alexander Bietsch and Bruno Michel. Conformal contact and pattern stability of stamps used for soft lithography. *Journal of Applied Physics*, 88(7):4310–4318, 2000.

[6] Ned Bowden, Scott Brittain, Anthony G Evans, John W Hutchinson, and George M Whitesides. Spontaneous formation of ordered structures in thin films of metals supported on an elastomeric polymer. *Nature*, 393(6681):146–149, 1998.

[7] Ned Bowden, Wilhelm TS Huck, Kateri E Paul, and George M Whitesides. The controlled formation of ordered, sinusoidal structures by plasma oxidation of an elastomeric polymer. *Applied Physics Letters*, 75(17):2557–2559, 1999.

[8] Vitali Brand, Christopher Bruner, and Reinhold H Dauskardt. Cohesion and device reliability in organic bulk heterojunction photovoltaic cells. *Solar Energy Materials and Solar Cells*, 99:182–189, 2012.

[9] William F Brown. *Developments in Fracture Mechanics Test Methods Standardization: A Symposium Presented at St. Louis, Mo., 4 May, 1976*. Number 632. ASTM International, 1977.

[10] Christopher Bruner and Reinhold Dauskardt. Role of molecular weight on the mechanical device properties of organic polymer solar cells. *Macromolecules*, 47(3):1117–1121, 2014.

[11] HC Cao and AG Evans. An experimental study of the fracture resistance of bimaterial interfaces. *Mechanics of Materials*, 7(4):295–304, 1989.

[12] Yifang Cao, Changsoon Kim, Stephen R Forrest, and Wole Soboyejo. Effects of dust particles and layer properties on organic electronic devices fabricated by stamping. *Journal of Applied Physics*, 98(3):033713, 2005.

[13] Robert W Carpick, D Frank Ogletree, and Miquel Salmeron. A general equation for fitting contact area and friction vs load measurements. *Journal of Colloid and Interface Science*, 211(2):395–400, 1999.

[14] J Chen, S Mwenifumbo, C Langhammer, J-P McGovern, M Li, A Beye, and WO Soboyejo. Cell/surface interactions and adhesion on ti-6al-4v: Effects of surface texture. *Journal of Biomedical Materials Research Part B: Applied Biomaterials*, 82(2):360–373, 2007.

[15] A Concha, JW McIver III, P Mellado, D Clarke, O Tchernyshyov, and RL Leheny. Wrinkling of a bilayer membrane. *Physical Review E*, 75(1):016609, 2007.

[16] H Corten. Fracture toughness: Part ii. *Proceedings of the 1971 National Symposium on Fracture Mechanics*, pages 1–10, 1972.

[17] G Dennler, C Lungenschmied, H Neugebauer, NS Sariciftci, and A Labouret. Flexible, conjugated polymer-fullerene-based bulk-heterojunction solar cells: basics, encapsulation, and integration. *Journal of Materials Research*, 20(12):3224–3233, 2005.

[18] Gilles Dennler, Markus C Scharber, and Christoph J Brabec. Polymer-fullerene bulk-heterojunction solar cells. *Advanced Materials*, 21(13):1323–1338, 2009.

[19] Boris V Derjaguin, Vladimir M Muller, and Yu P Toporov. Effect of contact deformations on the adhesion of particles. *Journal of Colloid and Interface Science*, 53(2):314–326, 1975.

[20] G Domokos, P Holmes, and B Royce. Constrained euler buckling. *Journal of Nonlinear Science*, 7(3):281–314, 1997.

[21] Jing Du, Tiffany Tong, Wali Akande, Androniki Tsakiridou, and Wole Soboyejo. Pressure effects on the lamination of organic light-emitting diodes. *Journal of Display Technology*, 9(8):601–606, 2013.

[22] Stephanie R Dupont, Mark Oliver, Frederik C Krebs, and Reinhold H Dauskardt. Interlayer adhesion in roll-to-roll processed flexible inverted polymer solar cells. *Solar Energy Materials and Solar Cells*, 97:171–175, 2012.

[23] Stephanie R Dupont, Eszter Voroshazi, Paul Heremans, and Reinhold H Dauskardt. Adhesion properties of inverted polymer solarcells: Processing and film structure parameters. *Organic Electronics*, 14(5):1262–1270, 2013.

[24] Yuri Ebata, Andrew B Croll, and Alfred J Crosby. Wrinkling and strain localizations in polymer thin films. *Soft Matter*, 8(35):9086–9091, 2012.

[25] AG Evans and BJ Dalgleish. The fracture resistance of metal-ceramic interfaces. *Acta Metallurgica et Materialia*, 40:S295–S306, 1992.

[26] Anthony G Evans, BJ Dalgleish, M He, and JW Hutchinson. On crack path selection and the interface fracture energy in bimaterial systems. *Acta Metallurgica*, 37(12):3249–3254, 1989.

[27] Anthony G Evans and John W Hutchinson. Effects of non-planarity on the mixed mode fracture resistance of bimaterial interfaces. *Acta Metallurgica*, 37(3):909–916, 1989.

[28] Huiyang Fei, Hanqing Jiang, and Dahl-Young Khang. Nonsinusoidal buckling of thin gold films on elastomeric substrates. *Journal of Vacuum Science & Technology A*, 27(3):L9–L12, 2009.

[29] Stephen R Forrest. The road to high efficiency organic light emitting devices. *Organic Electronics*, 4(2):45–48, 2003.

[30] Stephen R Forrest. The path to ubiquitous and low-cost organic electronic appliances on plastic. *Nature*, 428(6986):911–918, 2004.

[31] WW Gerberich and MJ Cordill. Physics of adhesion. *Reports on Progress in Physics*, 69(7):2157, 2006.

[32] Alexander Gottschalk and William R Schafer. Visualization of integral and peripheral cell surface proteins in live caenorhabditis elegans. *Journal of Neuroscience Methods*, 154(1):68–79, 2006.

[33] Tzung-Fang Guo, Seungmoon Pyo, Shun-Chi Chang, and Yang Yang. High performance polymer light-emitting diodes fabricated by a low temperature lamination process. *Advanced Functional Materials*, 11(5):339–343, 2001.

[34] John M Harris, Ganjigunte R Swathi Iyer, Anna K Bernhardt, Ji Yeon Huh, Steven D Hudson, Jeffrey A Fagan, and Erik K Hobbie. Electronic durability of flexible transparent films from type-specific single-wall carbon nanotubes. *ACS Nano*, 6(1):881–887, 2011.

[35] MY He, HC Cao, and AG Evans. Mixed-mode fracture: the four-point shear specimen. *Acta Metallurgica et Materialia*, 38(5):839–846, 1990.

[36] Heliatek. Heliatek achieves new world record for organic solar cells with certified 9.8 percent cell efficiency. White Paper, Dienstag, December 5, 2011.

[37] Hyun-Jung Her, Jung-Min Kim, CJ Kang, and Yong-Sang Kim. Hybrid photovoltaic cell with well-ordered nanoporous titania–p3ht by nanoimprinting lithography. *Journal of Physics and Chemistry of Solids*, 69(5):1301–1304, 2008.

[38] EK Hobbie, DO Simien, JA Fagan, JY Huh, JY Chung, SD Hudson, J Obrzut, JF Douglas, and CM Stafford. Wrinkling and strain softening in single-wall carbon nanotube membranes. *Phys. Rev. Lett*, 104(12):125505, 2010.

[39] Philip Holmes, Gábor Domokos, and Geertje Hek. Euler buckling in a potential field. *Journal of Nonlinear Science*, 10(4):477–505, 2000.

[40] Julia WP Hsu. Soft lithography contacts to organics. *Materials Today*, 8(7):42–54, 2005.

[41] Liangbing Hu, Hui Wu, Fabio La Mantia, Yuan Yang, and Yi Cui. Thin, flexible secondary li-ion paper batteries. *Acs Nano*, 4(10):5843–5848, 2010.

[42] David M Huang, Scott A Mauger, Stephan Friedrich, Simon J George, Daniela Dumitriu-LaGrange, Sook Yoon, and Adam J Moulé. The consequences of interface mixing on organic photovoltaic device characteristics. *Advanced Functional Materials*, 21(9):1657–1665, 2011.

[43] Jinsong Huang, Gang Li, and Yang Yang. A semi-transparent plastic solar cell fabricated by a lamination process. *Advanced Materials*, 20(3):415–419, 2008.

[44] ZY Huang, W Hong, and Z Suo. Nonlinear analyses of wrinkles in a film bonded to a compliant substrate. *Journal of the Mechanics and Physics of Solids*, 53(9):2101–2118, 2005.

[45] Seung-Hyun Hur, Dahl-Young Khang, Coskun Kocabas, and John A Rogers. Nanotransfer printing by use of noncovalent surface forces: Applications to thin-film transistors that use single-walled carbon nanotube networks and semiconducting polymers. *Applied Physics Letters*, 85(23):5730–5732, 2004.

[46] John W Hutchinson. The role of nonlinear substrate elasticity in the wrinkling of thin films. *Philosophical Transactions of the Royal Society of London A: Mathematical, Physical and Engineering Sciences*, 371(1993):20120422, 2013.

[47] John W Hutchinson and Zhigang Suo. Mixed mode cracking in layered materials. *Advances in Applied Mechanics*, 29(63):191, 1992.

[48] JWt Hutchinson. Fundamentals of the phenomenological theory of nonlinear fracture mechanics. *Journal of Applied Mechanics*, 50(4b):1042–1051, 1983.

[49] Veeco Instruments Inc. Improving the accuracy of afm force measurements,the thermal tune solution. White Paper, Bruker Corporation, Billerica, MA, 2005.

[50] Yeau-Ren Jeng, Ming-Lung Guo, Hung-Chang Li, and Tzung-Fang Guo. Interfacial morphology in polymer light-emitting diodes. *Electrochemical and Solid-State Letters*, 10(12):D139–D141, 2007.

[51] Hanqing Jiang, Dahl-Young Khang, Huiyang Fei, Hoonsik Kim, Yonggang Huang, Jianliang Xiao, and John A Rogers. Finite width effect of thin-films buckling on compliant substrate: experimental and theoretical studies. *Journal of the Mechanics and Physics of Solids*, 56(8):2585–2598, 2008.

[52] Xingyu Jiang, Shuichi Takayama, Xiangping Qian, Emanuele Ostuni, Hongkai Wu, Ned Bowden, Philip LeDuc, Donald E Ingber, and George M Whitesides. Controlling mammalian cell spreading and cytoskeletal arrangement with conveniently fabricated continuous wavy features on poly (dimethylsiloxane). *Langmuir*, 18(8):3273–3280, 2002.

[53] KL Johnson, K Kendall, and AD Roberts. Surface energy and the contact of elastic solids. In *Proceedings of the Royal Society of London A: Mathematical, Physical and Engineering Sciences*, volume 324, pages 301–313. The Royal Society, 1971.

[54] ID Johnston, DK McCluskey, CKL Tan, and MC Tracey. Mechanical characterization of bulk sylgard 184 for microfluidics and microengineering. *Journal of Micromechanics and Microengineering*, 24(3):035017, 2014.

[55] Dahl-Young Khang, Hanqing Jiang, Young Huang, and John A Rogers. A stretchable form of single-crystal silicon for high-performance electronics on rubber substrates. *science*, 311(5758):208–212, 2006.

[56] Changsoon Kim, Paul E Burrows, and Stephen R Forrest. Micropatterning of organic electronic devices by cold-welding. *Science*, 288(5467):831–833, 2000.

[57] Changsoon Kim, Yifang Cao, Winston O Soboyejo, and Stephen R Forrest. Patterning of active organic materials by direct transfer for organic electronic devices. *Journal of Applied Physics*, 97(11):113512, 2005.

[58] Dae-Hyeong Kim and John A Rogers. Stretchable electronics: materials strategies and devices. *Advanced Materials*, 20(24):4887–4892, 2008.

[59] Dae-Hyeong Kim, Jianliang Xiao, Jizhou Song, Yonggang Huang, and John A Rogers. Stretchable, curvilinear electronics based on inorganic materials. *Advanced Materials*, 22(19):2108–2124, 2010.

[60] Rak-Hwan Kim, Dae-Hyeong Kim, Jianliang Xiao, Bong Hoon Kim, Sang-Il Park, Bruce Panilaitis, Roozbeh Ghaffari, Jimin Yao, Ming Li, Zhuangjian Liu, et al. Waterproof alingap optoelectronics on stretchable substrates with applications in biomedicine and robotics. *Nature Materials*, 9(11):929–937, 2010.

[61] Seong-Ku Kim, Tao Liu, and Xiaogong Wang. Flexible, highly durable, and thermally stable swcnt/polyimide transparent electrodes. *ACS Applied Materials & Interfaces*, 7(37):20865–20874, 2015.

[62] CY Kuo, WC Tang, Chie Gau, TF Guo, and DZ Jeng. Ordered bulk heterojunction solar cells with vertically aligned tio 2 nanorods embedded in a conjugated polymer. *Applied Physics Letters*, 93(3):033307–033307, 2008.

[63] CY Kwong, AB Djurišić, PC Chui, KW Cheng, and WK Chan. Influence of solvent on film morphology and device performance of poly (3-hexylthiophene): Tio 2 nanocomposite solar cells. *Chemical Physics Letters*, 384(4):372–375, 2004.

[64] Stéphanie P Lacour, Joyelle Jones, Z Suo, and Sigurd Wagner. Design and performance of thin metal film interconnects for skin-like electronic circuits. *Electron Device Letters, IEEE*, 25(4):179–181, 2004.

[65] Stephanie P Lacour, Joyelle Jones, Sigurd Wagner, Teng Li, and Zhigang Suo. Stretchable interconnects for elastic electronic surfaces. *Proceedings of the IEEE*, 93(8):1459–1467, 2005.

[66] Mai T Lam, William C Clem, and Shuichi Takayama. Reversible on-demand cell alignment using reconfigurable microtopography. *Biomaterials*, 29(11):1705–1712, 2008.

[67] Ronald FM Lange, Yun Luo, Roman Polo, and Jürg Zahnd. The lamination of (multi) crystalline and thin film based photovoltaic modules. *Progress in Photovoltaics: Research and Applications*, 19(2):127–133, 2011.

[68] Jongho Lee, Jian Wu, Mingxing Shi, Jongseung Yoon, Sang-Il Park, Ming Li, Zhuangjian Liu, Yonggang Huang, and John A Rogers. Stretchable gaas photovoltaics with designs that enable high areal coverage. *Advanced Materials*, 23(8):986–991, 2011.

[69] Jung-Yong Lee, Steve T Connor, Yi Cui, and Peter Peumans. Semitransparent organic photovoltaic cells with laminated top electrode. *Nano letters*, 10(4):1276–1279, 2010.

[70] Teng Li, Zhenyu Huang, Zhigang Suo, Stéphanie P Lacour, and Sigurd Wagner. Stretchability of thin metal films on elastomer substrates. *Applied Physics Letters*, 85(16):3435–3437, 2004.

[71] Teng Li, ZY Huang, ZC Xi, Stephanie P Lacour, Sigurd Wagner, and Z Suo. Delocalizing strain in a thin metal film on a polymer substrate. *Mechanics of Materials*, 37(2):261–273, 2005.

[72] Teng Li and Z Suo. Ductility of thin metal films on polymer substrates modulated by interfacial adhesion. *International Journal of Solids and Structures*, 44(6):1696–1705, 2007.

[73] Teng Li, Zhigang Suo, Stéphanie P Lacour, and Sigurd Wagner. Compliant thin film patterns of stiff materials as platforms for stretchable electronics. *Journal of Materials Research*, 20(12):3274–3277, 2005.

[74] Shuang Fang Lim, Lin Ke, Wei Wang, and Soo Jin Chua. Correlation between dark spot growth and pinhole size in organic light-emitting diodes. *Applied Physics Letters*, 78(15):2116–2118, 2001.

[75] Darren J Lipomi, Jennifer A Lee, Michael Vosgueritchian, Benjamin C-K Tee, John A Bolander, and Zhenan Bao. Electronic properties of transparent conductive films of pedot: Pss on stretchable substrates. *Chemistry of Materials*, 24(2):373–382, 2012.

[76] Darren J Lipomi, Benjamin C-K Tee, Michael Vosgueritchian, and Zhenan Bao. Stretchable organic solar cells. *Advanced Materials*, 23(15):1771–1775, 2011.

[77] Youdong Mao, Wei L Wang, Dongguang Wei, Efthimios Kaxiras, and Joseph G Sodroski. Graphene structures at an extreme degree of buckling. *ACS Nano*, 5(2):1395–1400, 2011.

[78] Daniel Maugis. Adhesion of spheres: the jkr-dmt transition using a dugdale model. *Journal of Colloid and Interface Science*, 150(1):243–269, 1992.

[79] Michael D McGehee. Nanostructured organic–inorganic hybrid solar cells. *MRS Bulletin*, 34(02):95–100, 2009.

[80] Haixia Mei and Rui Huang. Wrinkling and delamination of thin films on compliant substrates. In *ICF13*, 2013.

[81] Juan Meng, Argjenta Orana, Ting Tan, Kurt Wolf, Nima Rahbar, Hannah Li, George Papandreou, Cynthia Maryanoff, and Wole Soboyejo. Adhesion and interfacial fracture in drug-eluting stents. *Journal of Materials Research*, 25(04):641–647, 2010.

[82] David B Mitzi, Konstantinos Chondroudis, and Cherie R Kagan. Organic-inorganic electronics. *IBM Journal of Research and Development*, 45(1):29–45, 2001.

[83] DY Momodu, T Tong, MG Zebaze Kana, AV Chioh, and WO Soboyejo. Adhesion and degradation of organic and hybrid organic-inorganic light-emitting devices. *Journal of Applied Physics*, 115(8):084504, 2014.

[84] Jean-Michel Nunzi. Organic photovoltaic materials and devices. *Comptes Rendus Physique*, 3(4):523–542, 2002.

[85] OK Oyewole, D Yu, J Du, J Asare, DO Oyewole, VC Anye, A Fashina, MG Zebaze Kana, and WO Soboyejo. Micro-wrinkling and delamination-induced buckling of stretchable electronic structures. *Journal of Applied Physics*, 117(23):235501, 2015.

[86] O Pietrement and M Troyon. General equations describing elastic indentation depth and normal contact stiffness versus load. *Journal of Colloid and Interface Science*, 226(1):166–171, 2000.

[87] Melanie Pretzl, Alexandra Schweikart, Christoph Hanske, Arnaud Chiche, Ute Zettl, Anne Horn, Alexander Boker, and Andreas Fery. A lithography-free pathway for chemical microstructuring of macromolecules from aqueous solution based on wrinkling. *Langmuir*, 24(22):12748–12753, 2008.

[88] Yi Qi, Jihoon Kim, Thanh D Nguyen, Bozhena Lisko, Prashant K Purohit, and Michael C McAlpine. Enhanced piezoelectricity and stretchability in energy harvesting devices fabricated from buckled pzt ribbons. *Nano Letters*, 11(3):1331–1336, 2011.

[89] Nima Rahbar, Kurt Wolf, Argjenta Orana, Roy Fennimore, Zong Zong, Juan Meng, George Papandreou, Cynthia Maryanoff, and Wole Soboyejo. Adhesion and interfacial fracture toughness between hard and soft materials. *Journal of Applied Physics*, 104(10):103533, 2008.

[90] Nima Rahbar, Yong Yang, and Winston Soboyejo. Mixed mode fracture of dental interfaces. *Materials Science and Engineering: A*, 488(1):381–388, 2008.

[91] Muruganathan Ramanathan, II S Michael Kilbey, Qingmin Ji, Jonathan P Hill, and Katsuhiko Ariga. Materials self-assembly and fabrication in confined spaces. *Journal of Materials Chemistry*, 22(21):10389–10405, 2012.

[92] James R Rice. A path independent integral and the approximate analysis of strain concentration by notches and cracks. *Journal of Applied Mechanics*, 35(2):379–386, 1968.

[93] JRa Rice and Gl F Rosengren. Plane strain deformation near a crack tip in a power-law hardening material. *Journal of the Mechanics and Physics of Solids*, 16(1):1–12, 1968.

[94] John E Sader, Ian Larson, Paul Mulvaney, and Lee R White. Method for the calibration of atomic force microscope cantilevers. *Review of Scientific Instruments*, 66(7):3789–3798, 1995.

[95] NS Sariciftci, L Smilowitz, Alan J Heeger, F Wudl, et al. Photoinduced electron transfer from a conducting polymer to buckminsterfullerene. *Science*, 258(5087):1474–1476, 1992.

[96] Tsuyoshi Sekitani, Hiroyoshi Nakajima, Hiroki Maeda, Takanori Fukushima, Takuzo Aida, Kenji Hata, and Takao Someya. Stretchable active-matrix organic light-emitting diode display using printable elastic conductors. *Nature Materials*, 8(6):494–499, 2009.

[97] FM Serry. Improving the accuracy of afm force measurements: The thermal tune solution to the cantilever spring constant problem. *Veeco Application Notes*, pages 1–4, 2005.

[98] WO Soboyejo, G-Y Lu, S Chengalva, J Zhang, and V Kenner. A modified mixed-mode bending specimen for the interfacial fracture testing of dissimilar materials. *Fatigue & Fracture of Engineering Materials & Structures*, 22(9):799–810, 1999.

[99] Wole Soboyejo. *Mechanical properties of engineered materials*, volume 152. CRC Press, 2002.

[100] Tze-Bin Song and Ning Li. Emerging transparent conducting electrodes for organic light emitting diodes. *Electronics*, 3(1):190–204, 2014.

[101] Christopher M Stafford, Christopher Harrison, Kathryn L Beers, Alamgir Karim, Eric J Amis, Mark R VanLandingham, Ho-Cheol Kim, Willi Volksen, Robert D Miller, and Eva E Simonyi. A buckling-based metrology for measuring the elastic moduli of polymeric thin films. *Nature Materials*, 3(8):545–550, 2004.

[102] Christopher M Stafford, Bryan D Vogt, Christopher Harrison, Duangrut Julthongpiput, and Rui Huang. Elastic moduli of ultrathin amorphous polymer films. *Macromolecules*, 39(15):5095–5099, 2006.

[103] Yugang Sun, Won Mook Choi, Hanqing Jiang, Yonggang Y Huang, and John A Rogers. Controlled buckling of semiconductor nanoribbons for stretchable electronics. *Nature Nanotechnology*, 1(3):201–207, 2006.

[104] Subra Suresh. *Fatigue of materials*. Cambridge University Press, 1998.

[105] Dongha Tahk, Hong H Lee, and Dahl-Young Khang. Elastic moduli of organic electronic materials by the buckling method. *Macromolecules*, 42(18):7079–7083, 2009.

[106] T Tong, B Babatope, S Admassie, J Meng, O Akwogu, W Akande, and WO Soboyejo. Adhesion in organic electronic structures. *Journal of Applied Physics*, 106(8):083708, 2009.

[107] Tiffany Michelle Tong. Adhesion and interfacial fracture: From organic light emitting devices and photovoltaic cells to solar lanterns for developing regions. *Princeton PhD Dissertation*, 2012.

[108] Matthew B Tucker, DR Hines, and Teng Li. A quality map of transfer printing. *Journal of Applied Physics*, 106(10):103504, 2009.

[109] Kalu Uduma and Tomasz Arciszewski. Sustainable energy development: the key to a stable nigeria. *Sustainability*, 2(6):1558–1570, 2010.

[110] Fangfang Wang, Mianqi Xue, and Tingbing Cao. Thermochemical patterning of polymer thin films with tunable size-reduction effects using metal-coated poly (dimethylsiloxane) stamps. *Advanced Materials*, 21(21):2211–2215, 2009.

[111] Yi Wang, Rong Yang, Zhiwen Shi, Lianchang Zhang, Dongxia Shi, Enge Wang, and Guangyu Zhang. Super-elastic graphene ripples for flexible strain sensors. *ACS Nano*, 5(5):3645–3650, 2011.

[112] Yifan Wang, Pongsakorn Kanjanaboos, Edward Barry, Sean Mcbride, Xiao-Min Lin, and Heinrich M Jaeger. Fracture and failure of nanoparticle monolayers and multilayers. *Nano Letters*, 14(2):826–830, 2014.

[113] Masashi Watanabe. Wrinkles with a well-ordered checkerboard pattern, created using dip-coating of poly (methyl methacrylate) on a uv–ozone-treated poly (dimethylsiloxane) substrate. *Soft Matter*, 8(5):1563–1569, 2012.

[114] Masashi Watanabe, Hirofusa Shirai, and Toshihiro Hirai. Wrinkled polypyrrole electrode for electroactive polymer actuators. *Journal of Applied Physics*, 92(8):4631–4637, 2002.

[115] Yong Xiang, Xi Chen, and Joost J Vlassak. The mechanical properties of electroplated cu thin films measured by means of the bulge test technique. In *MRS Proceedings*, volume 695, pages L4–9. Cambridge University Press, 2001.

[116] Jie Yin and Xi Chen. Buckling patterns of thin films on compliant substrates: the effect of plasticity. *Journal of Physics D: Applied Physics*, 44(4):045401, 2011.

[117] Supan Yodyingyong, Xiaoyuan Zhou, Qifeng Zhang, Darapond Triampo, Junting Xi, Kwangsuk Park, Benjie Limketkai, and Guozhong Cao. Enhanced photovoltaic performance of nanostructured hybrid solar cell using highly oriented tio2 nanotubes. *The Journal of Physical Chemistry C*, 114(49):21851–21855, 2010.

[118] Pil Jin Yoo, Kahp Y Suh, S Young Park, and Hong H Lee. Physical self-assembly of microstructures by anisotropic buckling. *Advanced Materials*, 14(19):1383–1387, 2002.

[119] Cunjiang Yu, Kevin OBrien, Yong-Hang Zhang, Hongbin Yu, and Hanqing Jiang. Tunable optical gratings based on buckled nanoscale thin films on transparent elastomeric substrates. *Applied Physics Letters*, 96(4):041111, 2010.

[120] D Yu, OK Oyewole, D Kwabi, T Tong, VC Anye, J Asare, E Rwenyagila, A Fashina, O Akogwu, J Du, et al. Adhesion in flexible organic and hybrid organic/inorganic light emitting device and solar cells. *Journal of Applied Physics*, 116(7):074506, 2014.

[121] Gang Yu, Jun Gao, Jan C Hummelen, Fred Wudl, and Alan J Heeger. Polymer photovoltiac cells: Enhanced efficiencies via a network of internal donor-acceptor heterojunctions. *Science*, 270(5243):1789, 1995.

[122] Zhibin Yu, Xiaofan Niu, Zhitian Liu, and Qibing Pei. Intrinsically stretchable polymer light-emitting devices using carbon nanotube-polymer composite electrodes. *Advanced Materials*, 23(34):3989–3994, 2011.

[123] Yin Zhang and Ya-pu Zhao. A precise model for the shape of an adhered microcantilever. *Sensors and Actuators A: Physical*, 171(2):381–390, 2011.

[124] Tae Hyoung Zyung, Seong Hyun Kim, Sang Chul Lim, Jung Hun Lee, Hye Yong Chu, Jeong-Ik Lee, and Ji Young Oh. Novel method for combining flexible organic light-emitting diodes with organic thin-film transistors. *Journal of the Korean Physical Society*, 48(91):S111–S114, 2006.